February 2019

Doctoral Thesis

The Weldability of Aluminium Alloy and Advanced High Strength Steel with Different Thicknesses by Hybrid Friction Stir Welding

Graduate School of Chosun University

Department of Welding and Joining Science Engineering

Kyoung-Hak Kim

The Weldability of Aluminium Alloy and Advanced High Strength Steel with Different Thicknesses by Hybrid Friction Stir Welding

알루미늄 합금과 초고강도강의 TWB
하이브리드 마찰교반용접부의 용접성에 관한 연구

February 25, 2019

Graduate School of Chosun University

Department of Welding and Joining Science Engineering

Kyoung-Hak Kim

The Weldability of
Aluminium Alloy and Advanced High
Strength Steel with Different Thicknesses
by Hybrid Friction Stir Welding

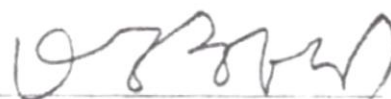Advisor: Professor Hee-Seon Bang

A Thesis Submitted for the Degree of
Doctor of Philosophy

October 2018

Graduate School of Chosun University

Department of Welding and Joining Science Engineering

Kyoung-Hak Kim

This is to certify that Ph.D. dissertation of Kyoung-Hak Kim has successfully met the dissertation requirements of Chosun University and has been approved by:

Chair of committee:
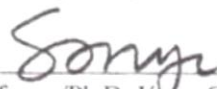
Professor/Ph.D. Han-Sur Bang

Department of Welding and Joining Science Engineering, Chosun University
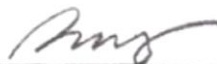
Member of committee:

Professor/Ph.D. Hee-Seon Bang

Department of Welding and Joining Science Engineering, Chosun University
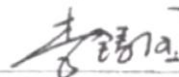
Professor/Ph.D. Yoon-Chul Sohn

Department of Welding and Joining Science Engineering, Chosun University

Director/Ph.D. Jong-Ho Song

Multi-Material Research Center, Korea Automotive Technology Institute (KATECH)

Professor/Ph.D. ZhuGuo Li

School of Materials Science and Engineering, Shanghai Jiaotong University

December 2018

Graduate School of Chosun University

TABLE OF CONTENTS

Chapter 3   Mechanical and Metallurgical Evaluation of Laser Assisted FSW Hybrid Welded Joints

Chapter 4   Features of Residual Stress in Laser Assisted FSW Hybrid Welded Joints

Chapter 5   Summary

LIST OF FIGURES

Chapter 3. *Mechanical and Metallurgical Evaluation of Laser Assisted FSW Hybrid Welded Joints*

IV

Chapter 4.   *Feature of Residual stress in Laser Assisted Friction Stir Welding*

LIST OF TABLES

ABSTRACT

The Weldability of Aluminium Alloy and Advanced High Strength Steel with Different Thicknesses by Hybrid Friction Stir Welding

Kyoung-Hak Kim

Advisor: Prof. Bang, Hee-Seon, Ph.D.

CO-Advisor: Prof. Bang, Han-Sur, Ph.D.

Dept. of Welding and Joining Science Engineering

Graduate School of Chosun University

자동차 산업은 세계적인 지구 온난화 및 자원 고갈과 환경규제 강화로 인하여 최대 격변기에 직면해 있으며, 선진국을 중심으로 한 자동차 연비규제가 지속적으로 강화되는 실정이다. 또한 승객의 안전성 및 편의성 향상을 위하여 장착되는 부품수의 증가로 인하여 차체 경량화는 더 이상 선택이 아닌 필수로 요구되고 있으며, 영원한 숙제로 인식되고 있다. 차체 경량화 기술 중에서 경량금속과 이종 또는 혼합재료를 채택하는 다중소재 혼용 기술(Multi-Materials Mix Technology)은 차체 중량을 보다 더 효과적으로 절감할 수 있다. 이에 따라 차체에 사용되는 소재 또한 점차 스틸과 알루미늄이 복합적으로 적절하게 구성 및 증가되고 있으며, 안정적인 개발을 위해서는 이종소재의 용접기술 확보가 필히 선행되어야 한다. 그러나 이종소재의 용접은 사용되는 소재간 물성이 크게 상이하므로 기존 용접방식으로는 고강도 및 고내구성의 용접부 품질을 구현하기 어렵게 된다.

통상적으로 이종소재 용접에 있어 두 금속의 융점 차이가 100℃ 이내에 있으면 용융용접이 가능하나, 그 이상일 경우에는 응고 시 융점 차이로 인한 응력이 발생하기 때문에 용융용접이 어렵고 브레이징 또는 고상용접이 채택 되어야 한다. 또한 선팽창 계수의 차이로 인한 열 응력은 이종소재 용접부의 균열형성에 기인하므로 건전한 용접부 강도를 확보하기 어렵다. 특히, 경량합금과 철계간 이종소재 용접에서는 계면에 형성되는 금속간화합물(Intermetallic compounds)이 강도에 지배적인 영향을 미치게 된다. 따라서, 이종소재 용접에 있어 적절한 공정선택과 함께 그에 따른 최적화된 공정변수를 통한 금속간화합물층의 형성을 최소화 시키는 것이 바람직하다.

1991년 영국 The Welding of Institute에서 개발된 마찰교반용접(Friction Stir Welding)은 대표적인 고상(Solid state) 용접법으로 알루미늄과 스틸의 이종소재 용접에 있어 효과적인 용접기술로 주목 받고 있다. 현재 마찰교반용접은 국내보다는 국외에서 보다 활발히 적용되고 있으나, 향후에는 국내 또한 그 수요와 적용이 증대될 것으로 예상된다. 상기의 용접기술은 열적 상태에서 금속을 가압 밀착시켜 미끄럼 변형을 일으키고 원자 상호간의 확산을 통하여 용접하므로 저입열하에서 보다 적은 변형과 함께 금속간화합물층의 성장이 극소화되며, 동적 재결정에 따른 결정립 미세화(Grain refinement)를 통한 용접부의 우수한 기계적 성질을 확보할 수 있다. 최근에는 보조열원을 이용한 하이브리드 마찰교반용접을 적용, 기존의 마찰교반용접과 비교하였을 때, 소성유동성 증가와 함께 향상된 용접부 강도 확보는 물론 사용되는 툴의 마모를 효과적으로 줄일 수 있는 장점으로 인하여 다양한 연구가 진행되고 있다.

따라서, 본 연구에서는 차체 경량화를 위한 5000계 알루미늄 합금과 초고강도강의 이종소재 용접법으로 레이저를 보조열원으로 이용한 하이브리드 마찰교반용접을 적용하였으며, 80% 이상의 우수한 용접부 강도 확보를 목표로 연구를 수행하였다. 개발된 하이브리드 마찰교반용접부의 타당성을 검증하기 위하여 기존 마찰교반용접과 동일한 공정 변수하에서 금속·기계학적 특성을 비교하였으며, 아울러 수치해석을 통한 이종소재 용접부의 온도분포를 고찰하고 잔류응력 특성을 규명하고자 하였다.

Chapter 1.

Introduction

1.1 General background

Global regulations on emission reduction and improving fuel efficiency in the automotive industry have become more restrictive in recent times. The Corporate Average Fuel Economy (CAFE) program requires automobile manufacturers to meet standards mandating higher fuel efficiency of 44.8 miles per gallon (mpg) by 2020, and the European Parliament and the Council of the European Union have agreed that the CO_2 emission targets will be implemented in the European Union within 2020. The passenger car standards are 95 g/km, reaching for 95% of vehicles in 2020 with 100% compliance in 2021 and the light-commercial vehicle standards are 147 g/km for 2020 [1]. In order to respond to these growing demands, the lightweight has played a major role in vehicle's design process because 10% reduction in vehicle weight can results in 6-8% fuel efficiency improvement as well emissions reduction, as shown in Fig. 1-1 [2].

The use of lightweight materials (LM) such as aluminium (Al) alloy, magnesium (Mg) alloy, advanced high-strength steel (AHSS), carbon fiber and polymer composite can possibly reduce the weight of car body and chassis components up to 50%.
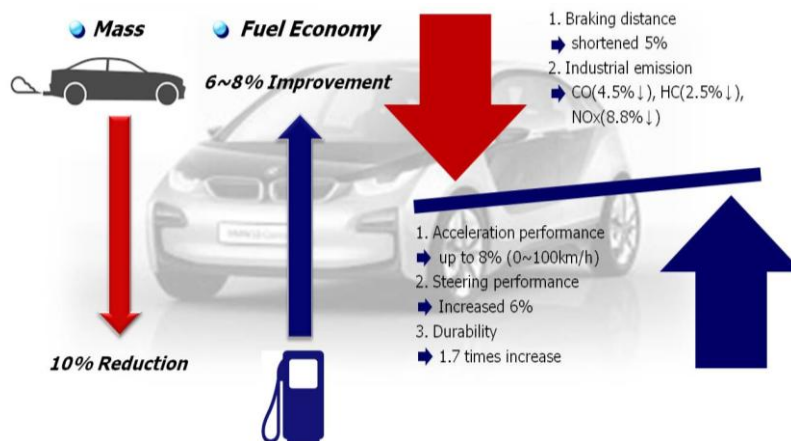
Fig. 1-1   *Advantages of weight reduction (Results of the effects of a trial calculation for a passenger vehicle achieving 10% weight reduction at 1,500 kg with a capacity of 5 peoples) [2]*

2

In particular, aluminium alloys are extensively used as the most promising lightweight materials in the automotive industry due to its high strength-to-weight ratio. As a result, stiffer and lighter designs can be produced by aluminium alloy in comparison to that of conventional steels. For applications of aluminium alloy in automotive components, Al-Mg alloy (AA5XXX series) is mainly used in chassis components due to its good weldability, high strength and excellent resistance to corrosion, while Al-Mg-Si alloy (AA 6XXX series) is employed in body panels due to its high strength with excellent formability. However, replacing a steel component by aluminium alloy component might lead to an important structural limitation. For instance, aluminium alloys have an elastic modulus of about 70 GPa, which is about one-third of typical steel. Therefore, under a given load, the component would undergo a greater deformation in elastic range than steel component of identical size and shape. On the other hands, aluminium alloys are less formable than automotive steel because of their low mechanical properties. The elongation, elastic modulus, plastic strain ratio (r-value) and strain hardening exponent (n-value) are critical mechanical properties that define the formability of car body and chassis component. Therefore, it is necessary that aluminium alloys should require not only strength and formability but also weldability and resistance to corrosion to be used for various automotive parts [3].

Furthermore, advanced high-strength steels such as dual phase (DP), complex phase (CP), ferritic-bainitic (FB), martensitic (MS), hot-formed (HF), transformation-induced plasticity (TRIP) and twinning-induced plasticity (TWIP) steel have been used to meet requirement for weight reduction with crash safety in automotive industry. Advanced high-strength steel, which is usually multi-phase microstructure for having reasonable formability and ductility, has poor weldability due to its higher carbon and alloying elements content than conventional lower-strength steels. That makes advanced high-strength steel more susceptible to welding thermal cycle, resulting in greater variations of microstructures and mechanical properties of welds [4].

One of the most prominent solutions for lightweight of the vehicle is to use the multi-material mix technology (MMMT) which is an advanced material application technology yielding weight reduction and improve performance. That is why multi-material structure, combining aluminium

alloy to advanced high-strength steel, is increasingly used to enhance the strength-to-weight ratio of the respective structural components in transportation industries including automotive, rail, shipbuilding and aerospace. There is a notable achievement for application of dissimilar welding in the automotive industry. Honda Motor Co., Ltd has recently developed a new robotic technology for the continuous dissimilar welding of steel to aluminium alloy by friction stir welding (FSW) process and employed it to sub-frame of Accord 2013 (Fig. 1-2) [5]. The newly designed sub-frame with this technique achieves 25% (6 kg) lighter weight than that of the previous model with aluminium alloy and steel manufactured by mechanical fastening such as bolting. The new technique of Honda Motor Co., Ltd can change the structure of sub-frame contributing to an increase in rigidity of mounting point by 20% and improved dynamic performance of the vehicle.
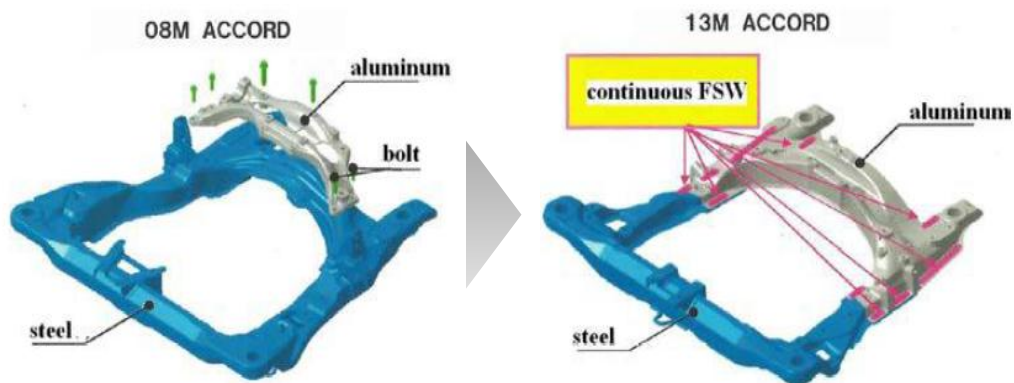
Fig. 1-2   Comparison between sub-frames of Accord 2008 and Accord 2013 (The new Accord 2013 increases aluminium portions and joins aluminium and steel by continuous FSW) [5]

However, the dissimilar joining of aluminium alloy to steel is challenging in the manufacturing of structures. The fundamental factors that result in failure of the joint between the dissimilar materials are wide differences in chemical and thermo-physical properties, the formation of the brittle intermetallic phase and galvanic corrosion. The formation of brittle intermetallic compounds (IMCs) layer at the Al-steel interface deteriorates the mechanical properties of the joint.

4

The intermetallic compounds layer formation can be limited to a size below 10 μm because a thick intermetallic compounds layer would cause the brittleness of the joint leading to easier crack initiation and propagation [6, 7]. Therefore, preventing the formation of excessive intermetallic compounds is vital in the dissimilar joining of aluminium to steel.

In conclusion, the potential of combining aluminium alloy to steel offers considerable flexibility in design and functionality of engineering structures. A comprehensive consideration on joint design associated with mechanical properties, microstructure characteristic and corrosion problem into dissimilar joint (galvanic corrosion) should be minutely considered for application of automotive components. The dissimilar materials of steel and aluminium alloy can be joined by thermal joining (e.g. solid/solid, solid/liquid, and liquid/liquid interface), mechanical fastening (e.g. clinching, riveting, and bolting) and adhesive bonding processes [8].

- Solid/solid interface joining, where peak temperature during the process is below the melting temperature of aluminium includes diffusion bonding [9], magnetic pulse welding [10], ultrasonic welding [11], friction stir welding [12] and hybrid friction stir welding [13]. Solid/liquid interface joining, where aluminium melts and wets to the solid steel includes arc brazing [14], laser brazing [15] and resistance spot welding [16]. Liquid/liquid interface joining, where peak temperature during is above the melting temperature of steel mainly use laser beam welding process [17].

- Adhesive bonding and mechanical fastening can be used to join dissimilar materials in the automotive industry. However, these processes have a drawback. Adhesive bonding requires the long processing time for ensuring effective bonding with environmental pollution. Mechanical fastening results in increased weight and stress concentration around the fastening locations [18].

5

1.2 Main issue in the dissimilar metal joining

When conventional fusion welding process is used to join dissimilar materials, thick and brittle intermetallic compounds and welding defects such as porosity, hot crack, and burn-through are easily formed. That happens due to fundamental limitations on the dissimilar joining of aluminium alloy and steel. For instance, vast differences in their chemical and thermo-physical properties such as the melting point (660 versus 1535℃), thermal conductivity (238 versus 77.5 W·m-1·K-1) and thermal expansion coefficient (23.5×10-6 versus 11.76×10-6/K) have impeded feasibility of dissimilar joining [19]. Therefore, dissimilar joints are expected to undergo a large temperature gradient that can lead to thermal strain and thermal stress. Due to limited mutual solubility between Fe and Al (the nearly-zero solid state solubility of Al in Fe and the zero solubility of Fe in Al) in the Fe-Al equilibrium phase diagram [20], the formation of intermetallic compounds at the faying Fe/Al interface is not only inevitable but also essential for establishing a strong atomic-scale metallurgical bonding. However, the brittleness of intermetallic compounds coupled with the presence of internal stress created during thermal joining process due to significant differences of their thermal properties makes dissimilar joint highly susceptible to cracking and brittle failure during service or operation. It is necessary that the formation of intermetallic compounds and welding defects should be properly controlled to produce a sound joint.

In this sense, a fundamental understanding of intermetallic compounds on the composition, morphology, nucleation, growth kinetics and mechanism is required to develop the improved materials and processes. When dissimilar materials come into contact at elevated temperature, the formation of intermetallic compounds depend on three main thermodynamic factors: (1) the chemical potentials of aluminium and iron elements, (2) the nucleation conditions at the beginning of inter-diffusion process, and (3) the mobility of the alloying constituent during thermal joining process [21]. It can be explained by the fact that the formation and growth of intermetallic compounds at the joint interface between Al and Fe could mainly contain three stages. The first stage involves the formation of solid solution through atomic diffusion at the interface. And then

6

intermetallic compounds will start to nucleate in the second stage when it is thermodynamically more favorable at corresponding temperature and constant pressure. In the third stage, solute atoms will continue to diffuse into the nucleus of stabilized intermetallic compounds for it to grow gradually. The Fe-Al phase diagram which presents the interaction as a function of temperature and elemental concentration under the atmospheric pressure is shown in Fig. 1-3. This system is characterized with an iron-based solid solution and six non-stoichiometric intermetallic compounds of FeAl (β2), Fe_3Al (β1), Fe_2Al_3 (ε), $FeAl_2$ (ζ), Fe_2Al_5 (η) and FeAl3 (θ). Table 1-1 suggests the stability rage, crystal structure and hardness of intermetallic compounds formed in Fe-Al binary system at room temperature. The phase reactions in Fe-Al phase diagram are shown in Table 1-2.
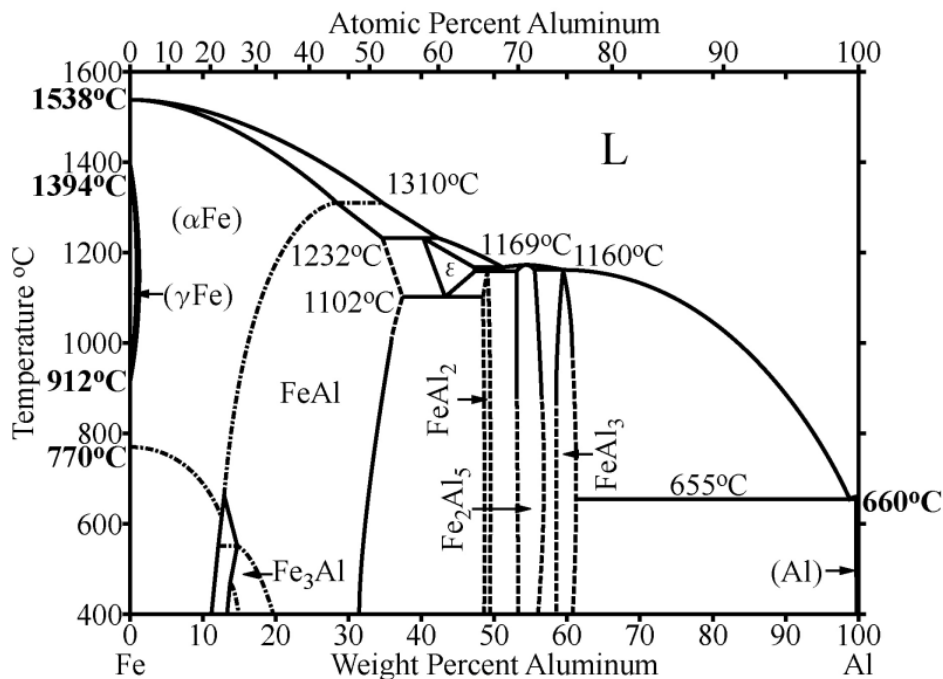
Fig. 1-3   Fe-Al equilibrium phase diagram [20]

7

Several studies have been performed on formation and growth of intermetallic compounds between molten Al and solid Fe. The formation of Fe_3Al occurs at a critical temperature of 552 ℃ (825 K) from FeAl (FeAl↔Fe_3Al) with Al concentration of around 26.5 at.%, while FeAl is formed through a peritectic reaction (liquid+α-Fe↔FeAl) under a much higher temperature of around 1310 ℃ (1583 K) with Al concentration of around 50.7 at.%. The Al-rich intermetallic compounds $FeAl_3$ are more likely to be formed at a critical temperature of 1157 ℃ (1430 K) through a peritictic reaction (liquid+Fe_2Al_5↔$FeAl_3$) with Al concentration ranging from 74.5 to 76.5 at.%. The intermetallic compounds Fe_2Al_5 can be formed by congruent compound (liquid↔Fe_2Al_5) at temperature of 1169 ℃ (1142 K) with Al concentration ranging from 69 to 74 at.%. The intermetallic compounds $FeAl_2$ tends to be formed through peritectoid reaction (Fe_2Al_5+ε-Fe_2Al_3↔ $FeAl_2$) from other phases of Fe_2Al_5 and Fe_2Al_3 at temperature of 1153 ℃ (1426 K) with Al concentration of around 66 at.%. The intermetallic compounds $FeAl_3$ is formed by a eutectic reaction (liquid↔$FeAl_3$+Al) at a critical temperature of 655 ℃ (928 K) [22, 23].

Above discussions explain that intermetallic compounds will depend primarily on elevated temperature and then the formation and growth of intermetallic compounds during welding could result from the thermal cycle at joint interface between aluminium alloy and steel. On the other hand, in case of friction stir welding process besides elevated temperature, the high pressure induced by mechanical force can be also taken into consideration on the formation of intermetallic compounds. It is further reported in laser roll welding for joining of aluminium alloy to steel that an increase in pressure can lead to the formation of interface layer at lower temperature under constant diffusion time [24]. Liu et al. explained that the formation and growth of intermetallic compounds are closely affected by three factors, such as temperature, mechanical welding force and material deformation status during friction stir welding process. According to the summary, mechanical welding force will raise the pressure, which can facilitate the phase reaction. Moreover, materials near pin will experience the severe plastic deformation under high strain rate, which enhances diffusion and reaction. The primary reason on diffusion enhancement suggests that short-circuiting along static and moving dislocations, grain boundaries and cracks generated during deformation can enhance the diffusion and facilitate nucleation of intermetallic compounds [25].

8

Table 1-1   Stability range, crystal structure and hardness of intermetallic compounds formed in Fe-Al binary system at room temperature [21-22]

Phases	Crystal structure	Stability range (at.%)	Vickers hardness (HV)	Density (Mg/mm^3)
Fe solid solution	BCC	0-45	-	7.8
γ-Fe	FCC	0-1.3	-	7.8
FeAl (β2)	BCC (order)	23-55	470-667	5.58
Fe$_3$Al (β1)	Do3	23-34	330-368	6.72
Fe$_2$Al$_3$ (ε)	Cubic (complex)	58-65	-	-
FeAl$_2$ (ζ)	Triclinic	66-66.9	1058-1070	-
Fe$_2$Al$_5$ (η)	Orthorhombic	70-73	100-1158	4.11
FeAl$_3$ (θ)	Monoclinic	74.5-76.5	772-1017	3.9
Al solid solution	FCC	99.998-100		2.69

Table 1-2   Phase reactions in Fe-Al phase diagram [22]

Reaction	Reaction composition (at.% Al)	Reaction temperature (°C)	Reaction type
αFe↔FeAl	45	1310	Critical
L+FeAl↔Fe$_2$Al$_3$	52	1232	Peritectic
L↔Fe$_2$Al$_3$+Fe$_2$Al$_5$	70.5	1165	Eutectic
L↔Fe$_2$Al$_5$+FeAl$_3$	72	1160	Unknown
L↔FeAl$_3$+Al	76.6	655	Eutectic
Fe$_2$Al$_3$+Fe$_2$Al$_5$↔FeAl$_2$	70	1156	Peritectoid
Fe$_2$Al$_3$↔FeAl+FeAl$_2$	55	1102	Eutectoid
L↔Fe$_2$Al$_5$	71	1169	Congruent
αFe↔FeAl	23.9	662	Tricritical
FeAl↔Fe$_3$Al	26.5	552	Critical
L↔δFe	0	1538	Melting
L↔Al	100	660	Melting
δFe↔γFe	0	1394	Allotropic
γFe↔αFe	0	912	Allotropic
L kFeAl$_6$+Al	85.7	653	Eutectic

1.3 Literature survey

In recent years, lightweight of the automobile is one of the major key strategies to meet the need of energy-saving, emissions reduction and fuel consumption [26]. As aluminium alloys of 5XXX or 6XXX are the most promising light materials despite the relatively expensive cost of more than steel, these are also used to replace steel in automotive components. Also, the use of advanced high strength steel is still preferred to achieve the weight reduction of the vehicle in the automotive industry. Especially, the multi-material combination such as light materials (Al and Mg alloy), advanced high strength steel (AHSS) and carbon fiber reinforced plastic (CFRP) is increasingly used to enhance the strength-to-weight ratio of the respective components in many transportation industries including the automotive industry.

The dissimilar joining of aluminium alloy to steel has attracted considerable attentions to achieve the lightweight for automotive applications. However, it is difficult to obtain a sound dissimilar joint by conventional fusion welding due to difference in the solid solubility, lattice transformation and thermal properties (thermal conductivity, thermal expansion, heat capacity and melting point) [27]. Especially, major problems are an excessive formation of intermetallic compound (IMC), which forms due to both chemical reaction and interdiffusion near interface between auminium alloy and steel, and generation of pores and cracks. According to the Fe-Al equilibrium phase diagram [20], non-stoichiometric intermetallic compounds of Fe-rich (Fe_3Al, FeAl,) and Al-rich ($FeAl_2$, Fe_2Al_5 and $FeAl_3$) are formed in Fe-Al system. Although Fe-rich intermetallic compound is preferred as ductile phase, Al-rich intermetallic compounds resulting in the brittle joints, are mainly generated in dissimilar joints during welding. Because the presence of intermetallic compound in joints interface can lead to severe problem causing brittleness and low strength, it is necessary that the size and quantity of intermetallic should be properly controlled with lower heat input during welding [28-32].

Many research works in joining of aluminium alloy to steel have been attempted by cold metal transfer welding (CMT) [31], advanced pulsed metal inert gas welding (Advanced Pulsed MIG) [33], resistance spot welding (RSW) [33], laser beam welding (LBM) [34], ultrasonic spot

welding (USW) [35] and friction stir welding [36]. The primary interest is not only how to control the thickness of intermetallic compounds but also to improve the mechanical properties of the joints. Since the transient thermal cycle and short diffusion time during welding processes may form different intermetallic compounds, an appropriate joining method has been required to join aluminium alloy to steel and to satisfy the strength of dissimilar joints.

Friction stir welding (FSW) developed by The Welding Institute (TWI) in 1991 has become a prominent process for joining of aluminium alloy to steel. The solid-state joining method generates lower heat input as compared to the conventional fusion welding processes preventing solidification problems such as solidification crack and porosity. This process can offer good mechanical properties in as-welded condition, low distortion and welding residual stress compared with conventional fusion welding and provides very limited Fe-Al intermetallic compound because the diffusion of Fe and Al in solid phase is much more difficult than the liquid phase. In this sense, the experimental studies have proven an understanding of the critical issue on joining of aluminium alloy to steel using friction stir butt welding. Watanabe et al. [36] investigated the effects of pin rotation speed, pin offset and pin diameter on tensile strength and microstructure of the dissimilar joints (AA5083 to SS400 mild steel). They obtained maximum tensile strength when pin offset at steel side. Intermetallic compounds of FeAl and $FeAl_3$ was formed at an upper part of the joint interface, while no intermetallic compounds were observed at central and bottom regions of joints interface. Ramachandran et al. [37] indicated that intermetallic compounds of FeAl, $FeAl_2$ and $FeAl_3$ were observed at joint interface and also joint strength was significantly dependent upon the thickness of intermetallic compounds formed at the interface. The typical softening at thermo-mechanically affected zone (TMAZ) close to stir zone (SZ) occurred due to the reduction in dislocation density. However, they explained that as reinforcement, the fragments of steel and intermetallic compounds distributed in the stir zone of aluminium alloy side were contributed to high tensile strength. The effect of tool offset and geometry of tool pin profile on the mechanical and metallographic characteristics of dissimilar joints (AA5052 to HSLA steel) was further reported by Ramachandran et al. [38]. Liu et al. [25] quantitatively studied the growth kinetics of interlayer by relationships between thickness and welding speed under process parameters on

11

rotational speed and tool offset. They indicated that the welding speed was related with interlayer thickness, whereas the variations in rotational speed and tool offset have an effect on the formation of the intermetallic compound of FeAl and Fe_3Al. Movahedi et al. [39] examined the effect of travel and rotation speed on the formation of reaction layer of dissimilar joints (AA5083 to St-12 steel) to improve the joint quality. They indicated that joints strength was enhanced by decreasing the travel speed and increasing the rotation speed. A thin intermetallic layer of less than 2 μm has no effect on joint strength resulting in fracture of base metal. Dehghani et al. [40] investigated the effect of plunge depth, tilt angle, pin geometry and travel speed at fixed rotation speed on microstructure and tensile strength. As a linear relationship, the thin intermetallic compound layer was formed by increasing travel speed resulting in low heat input.

On the other hand, hybrid joining process, which combines the principle process and other joining process, can be viable alternatives in similar and dissimilar welding. For instance, the hybrid effect between friction stir welding and additional energy source have a positive influences on heat generation, material flow and joint performance. Based on an extensive literature survey, the significant progress has been introduced in the fundamental understanding of hybrid friction stir welding on the microstructure and mechanical properties of joint. Additional energy sources combining friction stir welding process can be classified into two categories of thermal energy source and mechanical energy source [41].

Thermal energy source, which is carried out to soften the of workpiece as preheating source, include the electricity [42-45], induction [46-48], laser [49-52], plasma [53], arc [13, 54, 55], hot gas stream [56], gas torch [57], etc. Electricity and induction are used for resistance heating of the workpieces, whereas laser, arc, plasma and gas are adopted for direct preheating. As shown in Fig. 1-4, there are two configuration systems for current supply on electrically assisted friction stir welding (EAFSW). The first configuration is that the friction stir welding tool makes an integral part of the electric circuit. The electrical current is supplied into workpiece via the tool [42, 43]. The second configuration is that the tool is not an integral part of the electric circuit. The electrical current is exclusively supplied into the workpiece without any involvement of tool [44, 45]. Liu et

al. [45] applied an electrically assisted friction stir welding for joining Al 6061 to TRIP 780 steel with numerical analysis of electrical field distribution. They explained that the synergic effect of both electro-plastic effect and Joule heating can help reduce axial welding force and the electrical current can help formation of a thin layer of intermetallic compounds for plunge section of the joint due to combined effect of accelerated atom diffusion and reduced activation energy for chemical reaction. However, electrically assisted friction stir welding may have significant complexity optimizing window variables in process.

(a) Electricity passed through tool

(b) No electricity passed through tool
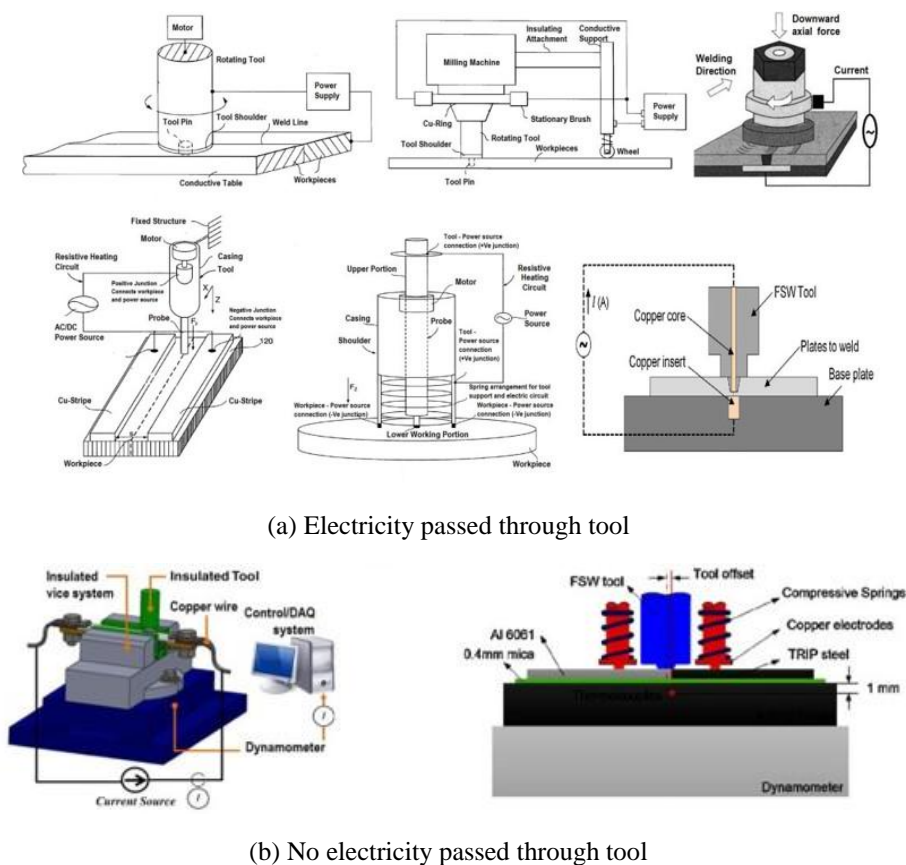
Fig. 1-4   Schematics of experimental set-up of electrically assisted FSW (EAFSW) [41]; (a) Electricity passed through tool [42, 43] and (b) No electricity passed through tool [44, 45]

13

On the other hand, several studies have been performed on laser assisted friction stir welding (LAFSW) for joining aluminium alloy to steel as shown in Fig. 1-5(a). The laser sources used, which is employed to locally preheat the surface of hard material, are diode laser and Nd:YAG laser. Merklein et al. used diode laser assisted friction stir welding to join 1 mm thick DC04 steel and Al 6016–T4 and reported maximum tensile strength of 80% of base aluminium alloy and good formability of drawable steel-aluminium tailored hybrids [49]. Similar investigation was reported by bang et al [50]. The tensile strength of Nd:YAG laser assisted friction stir welding was higher than that of conventional friction stir welding due to enhanced material flow by preheating of laser.

Based on gas tungsten arc welding assisted friction stir welding (GAFSW) for dissimilar joining as shown in Fig. 1-5(b), Bang et al. [13] used gas tungsten arc welding assisted friction stir welding to join 3 mm thick 304L stainless steel and Al 6061-T6 and to improve the weld strength. The maximum tensile strength obtained by TAFSW was 15% higher than that of conventional friction stir welding. According to their statements, the improved joint strength in GAFSW was attributed to the sufficient material plastic flow and partial annealing effect by GTAW preheating harder material side compared with conventional friction stir welding. The preheating effect of GTAW on enhanced joint properties was further confirmed by Bang et al. and Joo [54-55].
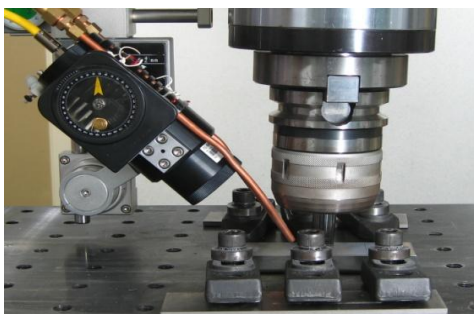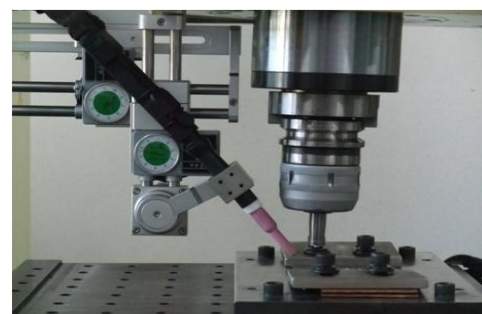
(a) Laser assisted FSW (LAFSW)　　　(b) Gas tungsten arc assisted FSW (GAFSW)

Fig. 1-5　　*Schematics of experimental set-up of (a) Laser assisted FSW (LAFSW) [50] and (b)Gas tungsten arc assisted FSW (GAFSW) [13, 54-55]*

14
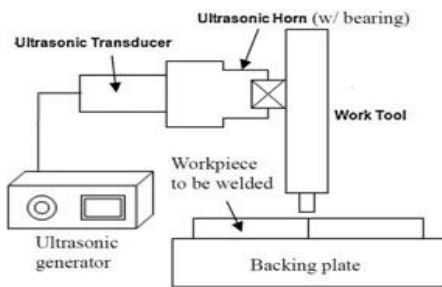
(a) Through FSW tool via bearing
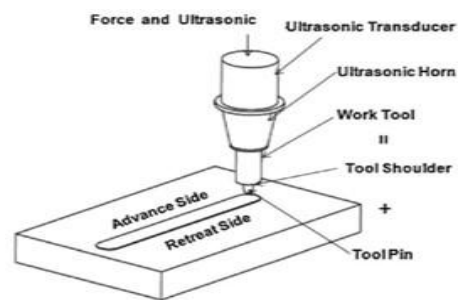
(b) Through tool
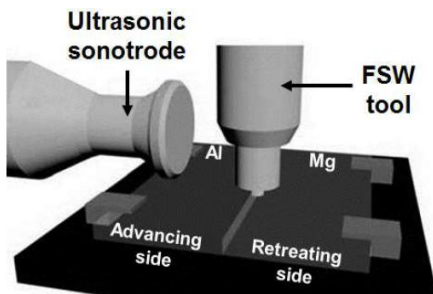
(c) Directly on far end of one of the workpiece
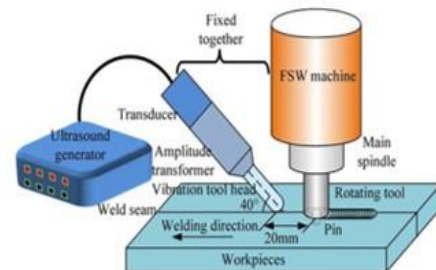
(d) Directly into weld zone

Fig. 1-6 *Schematics of experimental set-up of ultrasonic energy assisted FSW (UAFSW)*
[41]; (a) Through FSW tool via bearing [58], (b) Through tool [59], (c) Directly
on far end of one of the workpiece [60] and (d) Directly into weld zone [61]

Based on ultrasonic energy assisted friction stir welding (UAFSW), as shown in Fig. 1-6, ultrasonic energy, which is transmitted onto workpiece from horn, is mainly employed as mechanical energy source and ultrasonic vibrations directly soften the material without variation in process temperature. This process has been recently applied to joining similar material and dissimilar materials of light materials [58-61]. The ultrasonic vibration, which has been widely applied to metal plastic processing, was initially used to investigate the plasticity of metals by Blaha and Langenecher [62]. Langenecher explained that the ultrasonic vibration decreased the yield stress and flow stress of the metal during plastic deformation [63]. In summary for effect on

15

ultrasonic vibration, the ultrasonic energy required to form an identical amount of softening is 10,000,000 times less than that of thermal energy because it is preferentially absorbed at the dislocation in grains and is hardly absorbed in the defect free zones of the crystal. In this sense, there might be to have difference in softening effect of material between ultrasonic energy and heating energy since heating energy is distributed to be locally uniform into the material by heat conduction [64].

In summary on literature survey, for many implementations, hybrid friction stir welding offers many advantages on improvement on better mechanical properties, material flow, welding speed and reduction in tool wear. In present study, laser assisted friction stir welding adopting tailored welded blanks with different thickness of dissimilar materials will be performed to join 1.4 mm thickness DP590 steel and 2.5 mm Al5052-H32. Therefore, this research aims to provide a fundamental understanding of laser assisted friction stir welding for dissimilar aluminium alloy and advanced-high strength steel and improve the process ability through preheating effect by laser.

1.4 Research objectives

This investigation aims to develop a new innovative welding technique for dissimilar thickness materials of aluminium alloy (AA5052-H32) and advanced-high strength steel (DP590 steel). The technique used is based on conventional friction stir welding (CFSW) and laser assisted friction stir welding (LAFSW), which is considered to be environmental-friendly, economic and energy benefit as green technology. In present study, the joint performance and quality have been investigated through a critical analysis on correlation between the mechanical properties and the variation of microstructures of dissimilar joint in relation to the process parameters. Moreover, in laser assisted friction stir welding, the influence of laser preheating on mechanical properties and metallurgical characteristics including the formation and grow of intermetallic compounds, fracture path and welding defect has been compared with that of result obtained by conventional friction stir welding. A finite element model of three-dimensional transient thermal analysis has been developed to determine the temperature distribution of dissimilar Al/steel joints generated during conventional friction stir welding and laser assisted friction stir welding. The validity of finite element model has been verified through comparison with thermal cycle measured experimentally. Ultimately, the numerical and experimental investigation of thermally induced welding residual stress generated between aluminium and steel have been also performed by thermal elastic-plastic stress analysis and then the results predicted from analysis were compared with experimental results measured in dissimilar joints.

An additional aim is to manufacture the automotive part of side upper, which is combined into lightweight center floor module, by using developed process based on laser assisted friction stir welding, as shown in Fig. 1-7(a). In order to explore the industrial applicability of the developed dissimilar joining process, the durability of center floor module has been considered by vibration endurance test. Fig. 1-7(b) illustrates the lightweight center floor module combining the side upper produced by laser assisted friction stir welding. The durability of newly developed lightweight center floor module should be thoroughly satisfied based on the criteria specified of automotive industry (H-Motor Group).

Therefore, the aim of present study is to offer the comprehensive understanding on dissimilar Al/steel joints produced by conventional friction stir welding and laser assisted friction stir welding in its various aspects of mechanical and metallurgical characteristics as well as welding residual stress distribution. The summary of research objectives is therefore undertaken as:

➢ To develop the laser assisted friction stir welding process in dissimilar thickness materials of aluminium alloy and advanced-high strength steel through comparison between conventional friction stir welding and laser assisted friction stir welding

➢ To evaluate joint performance and quality on correlation between mechanical properties and the variation of microstructure in relation to the process variables and suggest optimum process variables in laser assisted friction stir welding

➢ To develop a three-dimensional transient thermal analysis for quantitative estimation of temperature field and thermal cycle in both conventional friction stir welding and laser assisted friction stir welding process

➢ To validate the analysis results with the corresponding experimentally measured results of thermal cycles in both conventional friction stir welding and laser assisted friction stir welding process

➢ To predict the thermally induced welding residual stress generated between aluminium and steel by thermal elastic-plastic stress analysis

18
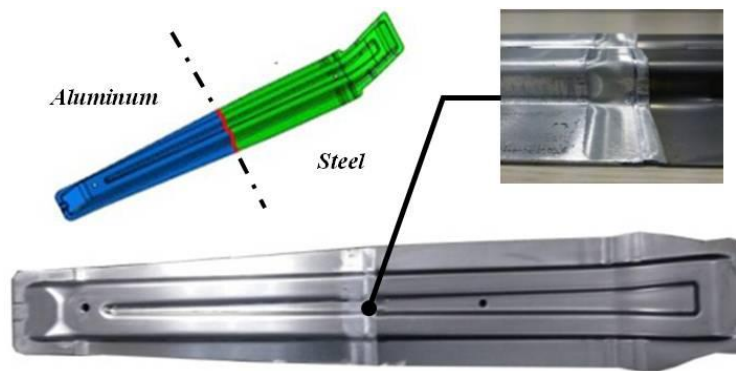
(a) Dissimilar Al/steel joints applied to lightweight side upper
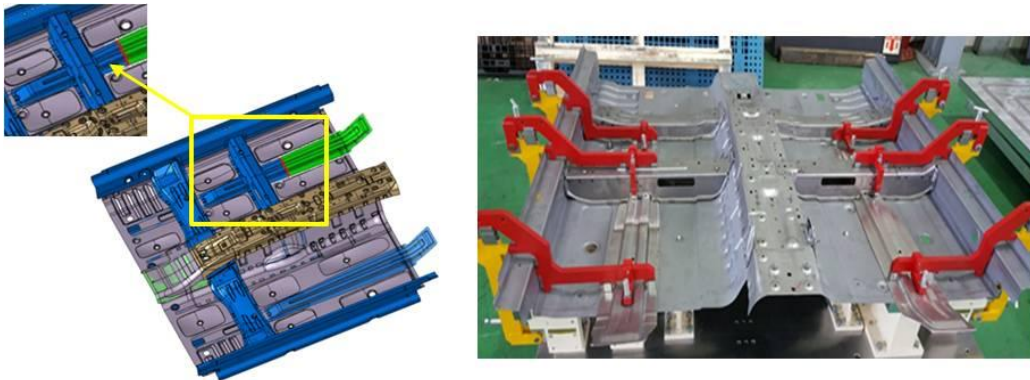
(b) Manufactured lightweight center floor of dissimilar materials

Fig. 1-7   *Lightweight center floor and side upper of automotive part manufactured by tailored laser assisted friction stir butt welded blanks; (a) Dissimilar Al/steel joints applied to lightweight side upper and (b) Manufactured lightweight center floor of dissimilar materials*

19

1.5 Construction of thesis

In present thesis, there consist of total five chapters on experimental and numerical investigation of dissimilar joining of aluminium alloy to advanced high-strength steel based on conventional friction stir welding and laser assisted friction stir welding. This chapter is mainly focused on general background, main issue in the dissimilar metal joining, literature survey and research objectives. The outline of this dissertation is organized as:

Chapter 2 entitled "experimental development of laser assisted FSW Hybrid welding process, which is based on the effect of welding parameters on laser assisted friction stir weldability in dissimilar joints of aluminium alloy 5052 and advanced high strength steel introduces the surface quality, material flow and welding defect.

Chapter 3 entitled "mechanical and metallurgical evaluation of laser assisted FSW hybrid welded joints" introduces the influence of preheating source on joint properties. In present chapter, based on conventional friction stir welding and laser assisted friction stir welding, the joint performance and quality have been investigated through critical analysis on correlation between the mechanical properties and microstructures of dissimilar joints in relation to the process parameters. The influence of preheating on mechanical properties and microstructures including intermetallic compounds, fracture path welding defect has been compared with that of result obtained by friction stir welding.

Chapter 4 entitled "features of residual stress in laser assisted FSW hybrid welded joints", introduces the results of numerical simulation research on heat conduction analysis and elastic-plastic analysis of laser assisted friction stir welding, mainly dealing with temperature field, welding residual stress field and plastic strain field thermally induced.

Chapter 5 entitled "summary" that is comprehended from the present thesis introduces the conclusion, scope of future work and appendix on publications.

20

Reference

[1]   www.europarl.europa.eu, Comparative study on the differences between the EU and US legislation on emission in the automotive sector, Study by EMIS Committee.

[2]   Kobuki. S., 2002. Mass reduction on vehicle. TOYOTA Technical Review. 52, 8-11

[3]   Sakuri, K., 2008. The latest trends in aluminium alloy sheets for automotive body panels. KOBELCO Technology Review. 28, 22-28

[4]   Zhili, Feng., 2006. Characterization of thermo-mechanical behaviors of advanced high strength steels (AHSS): task 2-weldability and performance evaluations of AHSS parts for automotive structures. Automotive Lightweighting Materials. 28, 206-218

[5]   Kusuda, Y., 2013. Honda develops robotized FSW technology to weld steel and aluminum and applied it to a mass-production vehicle. Industrial Robot: An International Journal. 40, 208-212

[6]   Sierra, G., Peyre, P., Deschaux Beaume, F., Stuart, D., Fras, G., 2008. Steel to aluminium braze welding by laser process with Al12Si filler wire. Sci. Technol. Weld. Join. 13, 430-437.

[7]   Nasiri, A. M., Li. L., Kim, S. H., Zhou, Y., Weckman, D. C., Nguyen, T. C. 2011. Microstructure and properties of laser brazed magnesium to coated steel. Weld. J. 90, 211-219

[8]   Pouranvari, M., 2017. Critical assessment: dissimilar resistance spot welding of aluminium/steel: challenges and opportunities. Mater. Sci. Technol. 33, 1705-1712

[9]   Karfoul, M. K., Tatlock, G. J., Murray, R. T., 2007. The behavior of iron and aluminium during the diffusion welding of carbon steel to aluminium. J. Mater. Sci. 42, 5692-5699

[10]   Yu, H., Xu, Z., Fan Z., Zhao, Z., Li, C., 2013. Mechanical property and microstructure of aluminium alloy-steel tubes joint by magnetic pulse welding. Mater. Sci. Eng. A-struct. Mater. Prop. Microstruct. Process. 561, 259-265

[11]   Prangnell, P., Haddadi, F., Chen, Y. C., 2011. Ultrasonic spot welding of aluminium to steel for automotive applications-microstructure and optimization. Mater. Sci. Technol. 27, 617-624

[12]   Ratanathavorn, W., Melander, A., Magnusson, H., 2016. Intermetallic compounds in

friction stir lap joints between AA5754/galvanized ultra-high strength steel. Sci. Technol. Weld. Join. 21, 653-659

[13] Bang, H. S., Bang, H. S., Jeon, G. H., Oh, I. H., Ro, C. S., 2012. Gas tungsten arc welding assisted hybrid friction stir welding of dissimilar materials Al6061-T6 aluminum alloy and STS304 stainless steel. Mater. Des. 37, 48-55

[14] Song, J. L., Lin, S. B., Yang, C. L., Fan, C. L., Ma, G. C., 2010. Analysis of intermetallic layer in dissimilar TIG welding-brazing butt joint of aluminium alloy to stainless steel. Sci. Technol. Weld. Join. 15, 213-218

[15] Mei, S. W., Gao, M., Yan, J., Zhang, C., Li, G., Zeng, X. Y., 2013. Interface properties and thermodynamic analysis of laser-arc hybrid welded Al/steel joint. Sci. Technol. Weld. Join. 18, 293-300

[16] Chen, N., Wang, H.P., Carlson B.E., Sigler, D.R., Wang, M., 2018. Fracture mechanisms of Al/steel resistance spot welds in coach peel and cross tension testing. J. Mater. Process. Technol. 252, 348-361

[17] Lee, K. J., Kumai, S., Arai, T., 2005. Interfacial microstructure and strength of steel to aluminum alloy lap joints welded by a defocused laser beam. Mater. Trans. 46, 1847-1856

[18] Nagatsuka, K., Xiao, B., Wu, L., Nakata, S., 2018. Resistance spot welding of metal/carbon-fibre-reinforced plastics and applying silane coupling treatment. Sci. Technol. Weld. Join. 23, 181-186

[19] Casalino, C., Leo, P., Mortello, M., Perulli, P., 2017. Effects of laser offset and hybrid welding on microstructure and IMC in Fe-Al dissimilar welding. METALS-BASEL.7, No page number

[20] Kattner, U. R., 1990. In: binary alloy phase diagrams. Materials Park, OH: ASM International; 147

[21] Atabaki, M. M., Nikodinovski, M., Chenier, P., Ma, J., Harooni, M., Kovacevic, R., 2014. Welding of aluminum alloy to steels: an overview. J. Manuf. Sci. Prod. 14, 59-78

[22] Shahverdi, H. R., Ghomashchi, M. R., Shabestari, S., Hejazi, J., 2002. Microstructural analysis of interfacial reaction between molten aluminium and solid iron. J. Mater. Process. Technol. 124, 345-352

[23] Kubaschewski, O., 1982. Iron-binary phase diagrams. Springer Verlag Berlin Heidelberg

22

GmbH, Germany

[24]   Rathod, M.J., Kutsuna, M., 2004. Joining of aluminum alloy 5052 and low-carbon steel by laser roll welding. Weld. J. 83, 16-26

[25]   Liu, X., Lan, S., Ni, J., 2014. Analysis of process parameters effects on friction stir welding of dissimilar aluminum alloy to advanced high strength steel. Mater. Des. 59, 50-62

[26]   Pouranvari, M., 2017. Critical assessment: dissimilar resistance spot welding of aluminium/steel: challenges and opportunities. Mater. Sci. Technol 33, 1705-1712

[27]   Atabaki, M.M., Nikodinovski, M., Chenier, P., Ma, J., Harooni, M., Kovacevic, R., 2014. Welding of aluminum alloy to steels: an overview. J. Manuf. Sci. Prod. 14, 59-78

[28]   Zhang, W., Sun, D., Han, L., Gao, W., Qiu, X., 2011. Characterization of intermetallic compounds in dissimilar material resistance spot welded joint of high strength steel and aluminum alloy. J. Manuf. Process. 178, 342-349

[29]   Xu, L., Wang, L., Chen, Y.C., Robson, J.D., Prangnell, P.B., 2016. Effect of interfacial reaction on the mechanical performance of steel to aluminum dissimilar ultrasonic spot welds. Metall. Mater. Trans. A-Phys. Metall Mater. Sci. 47A, 334-346

[30]   Chen, H.C., Pinkerton, A.J., Li, L., Liu Z., Mistry, A.T., 2011. Gap-free fibre laser welding of Zn-coated steel on Al alloy for light-weight automotive applications. Mater. Des. 32, 495-504

[31]   Agudo, L., Eyidi, D., Schmaranzer, C.H., Arenholz, E., Jank, N., Bruckner, J., Pyzalla, A., 2007. Intermetallic FexAly-phase in a steel/Al-alloy fusion weld. J. Mater. Sci. Technol. 42, 4205-4214

[32]   Springer, H., Kostka, A., Payton, E.J., Raabe, D., Kaysser-Pyzalla, Eggeler, G., 2011. On the formation and growth of intermetallic phase during interdiffusion between low-carbon steel and aluminum alloys. Acta Mater. 59, 1586-1600

[33]   Das, A., Shome, M., Goecke, S.F., De, A., 2017. Joining of aluminium alloy and galvanized steel using a controlled gas metal arc process. J. Manuf. Process. 27, 179-187

[34]   Chen, N., Wang, H.P., Carlson B.E., Sigler, D.R., Wang, M., 2018. Fracture mechanisms of Al/steel resistance spot welds in coach peel and cross tension testing. J. Mater. Process. Technol. 252, 348-361

[35]   Watanabe, T., Sakuyama, H., Yanagisawa, A., 2009. Ultrasonic welding between mild steel

sheet and Al-Mg alloy sheet. J. Manuf. Process. Technol. 209, 5475-5480

[36] Watanabe, T., Takayama, H., Yanagisawa, A., 2006. Joining of aluminum alloy to steel by friction stir welding. J. Manuf. Process. Technol. 178, 342-349

[37] Ramachandran, K.K., Murugan, N., Shashi Kumar, S., 2015. Friction stir welding of aluminum alloy AA5052 and HSLA steel. Weld. J. 94, 291-300

[38] Ramachandran, K.K., Murugan, N., Shashi Kumar, S., 2015. Effect of tool axis offset and geometry of tool pin profile on the characteristics of friction stir welded dissimilar joints of aluminum alloy AA5052 and HSLA steel. Mater. Sci. Eng. A-struct. Mater. Prop. Microstruct. Process. 639, 219-233

[39] Movahedi, M., Kokabi, A.H., Seyed Reihani, S.M., Najafi, H., 2012. Effect of tool travel and rotation speeds on weld zone defects and joint strength of aluminium steel lap joints made by friction stir welding. Sci. Technol. Weld. Join. 17, 162-167

[40] Dehghani, M., Amadeh, A., Akbari Mousavi, S.A.A., 2013. Investigations on the effects of friction stir welding parameters on intermetallic and defect formation in joining aluminum alloy to mild steel. Mater. Des. 49, 433-441

[41] Padhy, G. K., Wu, C. S., Gao, S., 2015. Auxiliary energy assisted friction stir welding – status review. Sci. Technol. Weld. Join. 20, pp. 631-649

[42] Long, X., Khanna, S. K., 2005. Modelling of electrically enhanced friction stir welding process using finite element method. Sci. Technol. Weld. Join. 10, pp. 482-487

[43] Santos, T. G., Miranda, R. M., Vilaca, P., 2014. Friction stir welding assisted by electrical joule effect. J. Mater. Process. Technol. 214, pp. 2127-2133

[44] Potluri, H., Jones, J. J., Mears, L., 2013. Comparison of electrically assisted and conventional friction stir welding processes by feed force and torque. Proc. ASME 2013 Int. Manufacturing Science and Engineering Conf. (doi:10.1115/MSEC2013-1192)

[45] Liu, X., Lan, S., Ni, J., 2015. Electrically assisted friction stir welding for joining Al 6061 to TRIP780 steel. J. Mater. Process. Technol. 219, pp. 112-123

[46] Sinclair, P. C., Longhurst, W. R., Cox, Ch. D., Lammlein, D. H., 2010. Heated friction stir welding: an experimental and theoretical investigation into how preheating influences process forces. Mater. Manuf. Processes. 25, pp. 1283-1291

[47] Alvarez, I., Garcia, M., Pena, G., Sotelo, J., Verdera, D., 2013. Assisted friction stir

24

welding of carbon steel: use of induction and laser as preheating techniques. TMS (The Minerals, Metals & Materials Society). 7, pp. 117-126

[48]   Alvarez, I., Garcia, M., Pena, G., Sotelo, J., Verdera, D., 2014. Evaluation of an induction-assisted friction stir welding technique for super duplex stainless steels. Surf. Interface Anal. 46, pp. 892-896

[49]   Merklein, M., Giera, A., 2008. Laser assisted friction stir welding of drawable steel-aluminum tailored hybrids. Int. J. Mater. Form. 1, pp. 1299-1302

[50]   Bang, H. S., Bang, H. S., Kim, H. S., Kim, J. H., Oh, I. H., Ro, C. S., 2010. A study on the weldability and mechanical characteristics of dissimilar materials butt joints by laser assisted friction stir welding. J. of welding and joining. 28, pp. 70-75

[51]   Sun, Y. F., Konishi, M., Kamai, M., Fujii. H., 2013. Microstructure and mechanical properties of S45C steel prepared by laser-assisted friction stir welding. Mater. Des. 47, pp 842-849

[52]   Campanelli, S. L., Casalino, G., Casavola, C., Moramarco, V., 2013. Analysis and comparison of friction stir welding and laser assisted friction stir welding of aluminum alloy. Materials. 6, pp. 5923-5941

[53]   Yaduwanshi, D. K., Bag, S., Pal, S., 2014. Effect of preheating in hybrid friction stir welding of aluminum alloy. J. Mater. Eng. Perform. 23, pp. 3794-3803

[54]   Bang, H. S., Bang, H. S., Song, H. J., Joo, S. M., 2013. Join properties of dissimilar Al6061-T6 aluminum alloy/Ti-6%Al-4%V titanium alloy by gas tungsten arc welding assisted hybrid friction stir welding. Mater. Des. 51, pp. 544-551

[55]   Joo, S. M., 2013. Joining of dissimilar AZ31B magnesium alloy and SS400 mild steel by hybrid gas tungsten arc friction stir welding. Met. Mater. Int. 19, pp. 1251-1257

[56]   Choi, D. H., Lee, C. Y., Ahn. B. W., Choi, J. H., Yeon, Y. M., Song, K., Hong, S. G., Lee, W. B., Kang, K. B., Jung, S. B., 2011. Hybrid friction stir welding of high-carbon steel. J. Mater. Sci. Technol. 27, pp. 127-130

[57]   Lotfi, A. H., Nourouzi, S., 2014. Predictions of the optimized friction stir welding process parameters for joining AA7075-T6 aluminum alloy using preheating system. Int. J. Adj. Manuf. Technol. 73, pp. 1717-1737

[58]   Park, K., Kim, B., Ni, J., 2007. Design and analysis of ultrasonic assisted friction stir

25

welding. Proc. ASME 2007 Int. Mechanical Engineering Cong. and Exposition. 3, pp. 731-737 (doi: 10.1115/IMECE200744007) 21

[59] Lai, R. L., He, D. Q., Liu, L., Ye, Y. S., Yang, K., 2014. A study of the temperature field during ultrasonic-assisted friction-stir welding. Int. J. Adv. Manuf. Technol. 73, pp. 321-327

[60] Strass, B., Wagner, G., Eifler, D., 2014. Realization of Al/Mg-hybrid-joints by ultrasound supported friction stir welding. Mater. Sci. Forum. 783-786, pp. 1814-1819

[61] Shi, L., Wu, C. S., Liu, X. C., 2015. Modelling the effects of ultrasonic vibration on friction stir welding. J. Mater. Process. Technol. 222, pp. 91-102

[62] Blaha, F., Langenecker, B., 1955. Tensile deformation of zinc crystal under ultrasonic vibration. Naturwissenschaften. 42, 556

[63] Langenecker, B., 1966. Effects of ultrasound on deformation characteristics of metals. IEEE Trans. Son. Ultrason. 13, pp. 1-8

[64] Liu, X. C., Wu, C. S., Padhy, G. K., 2015. Improved weld macrosection, microstructure and mechanical properties of 2024Al-T4 butt joints in ultrasonic vibration enhanced friction stir welding. Sci. Technol. Weld. Join. 20, pp. 345-352

Chapter 2.

Experimental Development of Laser Assisted FSW Hybrid Process

27

2.1 Introduction

Tailor welded blanks (TWB), which is combining different thickness materials represents one of the most exciting areas as the lightweight structures in automobile joining applications. Laser beam welding has already achieved a relatively significant predominance in the joining of steels [1]. On the other hand, the considerable potential for aluminium joining of TWB with difference thickness has been recently verified by friction stir welding [2-4]. On the other hand, a variety of aspects have to be adequately considered such as joining process, joint geometry, sheet thickness, welding distortion and galvanic corrosion relevant to mechanical properties when dissimilar joints of aluminium alloy and steel are designed for actual application of automotive component [5-7]. However, the research work on laser assisted friction stir welding for tailored welded blanks (TWB) of dissimilar materials with different thicknesses is still not available in the literature.

Therefore, in present chapter, the aim of this work intends to assess the applicability of dissimilar joining of aluminium alloy and advanced high-strength steel with different thicknesses in conventional friction stir welding and laser assisted friction stir welding. The comprehensive effect of process variables (e.g. pin offset, rotation speed and travel speed, laser power) on the surface quality, material flow and welding defect has been extensively investigated in friction stir welding and laser assisted friction stir welding process. Especially, this chapter provides a fundamental understanding of laser assisted friction stir welding for dissimilar aluminium alloy and advanced-high strength steel and improve the process ability through the effect on laser preheating.

2.2 Experimental details

2.2.1 Experimental set-up

In present study, 2.5 mm thick AA5052-H32 and 1.4 mm thick SPFC590DP steel have been used for fabrication of dissimilar thickness tailored blanks by friction stir butt welding process. The experimental set-up of friction stir butt welding with joint configuration of 200 mm (L) × 200 mm (B) is shown in Fig. 2-1. AA 5052-H32, which is the non-heat treatable Aluminum-Magnesium alloy with good strength and corrosion resistance, is widely used for manufacturing automotive components in automotive industry. SPFC590DP steel, which is cold rolled (CR) dual-phase (DP) steel having martensite phase in ferrite matrix, has been used as advanced high-strength steel (AHSS) for lightweight application. The chemical compositions and mechanical properties of dissimilar materials are listed in Table 2-1. All base metals were cleaned to remove impurity of the faying surface with the acetone before welding. The AA5052-H32 and SPFC590DP steel sheet were placed at retreating and advancing side, respectively, as shown in Fig. 2-1. Watanabe et al. [8] explained that hard material such as steel should be positioned at advancing side for successful joining and pin offset located at steel faying surface should be further shifted toward steel. The tungsten carbide (WC)-12% Cobalt (Co), which is hard metal with 1,522 HV made tapered cylindrical FSW tool (prepared by Daewha Alloytech Company in Korea) was used for experiment. As shown in Fig. 2-1, the tool shape of shoulder and pin was concave and frustum, respectively. Figure 2-1 shows the dimensions of the tool. The tool dimensions were as follow: shoulder diameter of 18 mm; pin diameter of top 6 mm, pin diameter of bottom 4 mm; pin length 1.4 mm. The tool tilt angle was kept around 3°. Table 2-2 lists welding parameters used in present study.

The laser assisted friction stir welding system (LAFSW) together with charge-coupled device (CCD) is designed for joining aluminium alloy to steel, as shown in Fig. 2-1. The laser source used in this study, which is employed to locally preheat the workpiece of steel, is industrial 400 W Diode Laser (United Winner Laser Ltd.: UW-400-915). The CCD camera adopted in laser assisted friction stir welding system was used to precisely control the pin-offset and line arrangement for preheating during experiment. All experiments of conventional friction stir welding and laser

assisted friction stir butt welding were performed in displacement-control mode. The load indicator (Model) was utilized to reveal the influence of process parameters on the axial vertical force (F_z) during welding. The temperature history during laser assisted friction stir welding was recorded using data logger with K thermocouples of 1 mm diameter. The locations of thermocouples where were measured in midsection perpendicular to welding direction on the workpieces of aluminium alloy and steel, respectively are shown in Fig. 2-1. The preceding laser heating source was preheated at the point of 2 mm steel away from joint interface with an angle of 45°. The distance between tool and laser preheating beam is 5 mm. This effect on preheating is to ensure the wear reduction of tool and to enhance the material plastic flow during welding.
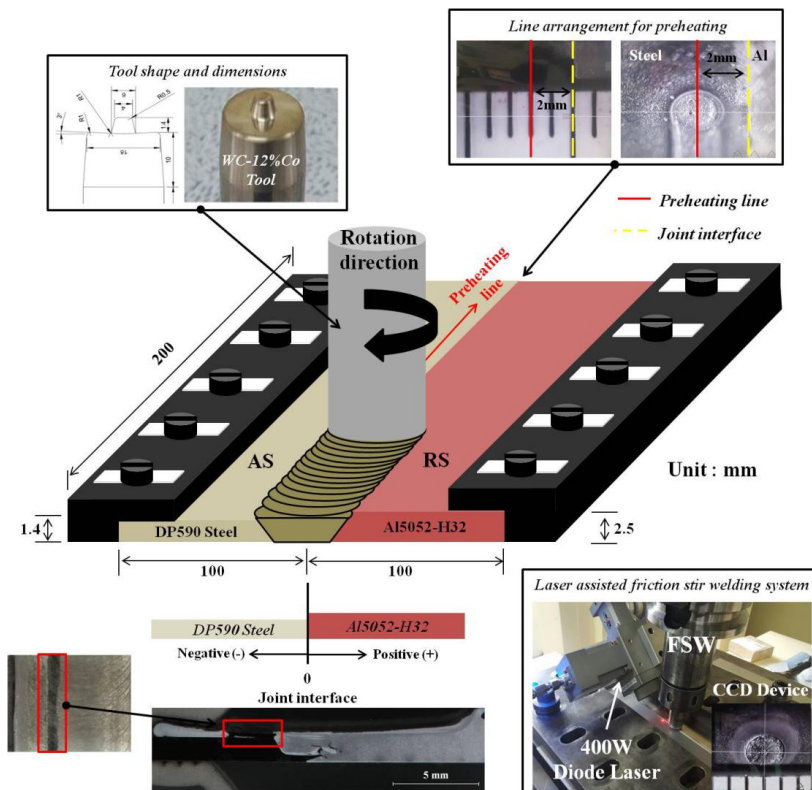
Fig. 2-1   Schematics of experimental set-up of laser assisted friction stir welding system adopted with charge-coupled device (CCD)

30

Table 2-1   Chemical compositions and mechanical properties of materials used

Chemical compositions (wt.%)

Material	C	Mn	Si	P	S	Fe
SPFC590DP	0.0762	1.833	0.249	0.0108	0.0042	Bal.
AA5052-H32	-	0.01	0.09	-	-	0.21
	Mg	Cu	Ti	Cr	Al	
	2.34	0.01	0.011	0.19	97.14	

Mechanical properties

Material	Yield strength (MPa)	Tensile strength (MPa)	Elongation (%)
SPFC590DP	459	623	24
AA5052-H32	188	225	12

Table 2-2   Conventional friction stir welding and laser assisted friction stir welding parameters

Welding process	Welding parameters	Values
Conventional FSW	Tool rotation speed (rpm)	300, 400, 500
	Travel speed (mm/min)	60, 90, 120
	Plunge depth (mm)	0.9
	Pin-offset (mm)	0-0.8
	Tilt angle (°)	3 (Fixed)
Laser	Power (W)	200 (Fixed)
	Focal length (mm)	90 (Fixed)
	Beam diameter (mm)	2 (Fixed)
Back plate	STS304L	

2.2.2 Experimental method

(a) Mechanical test

Fig. 2-2 shows the dimensions of the standard tensile specimen and fatigue specimen. The tensile and fatigue specimens perpendicular to welding direction were prepared using a wire-cutting machine. The load axis was applied in the direction perpendicular to the dissimilar weld. The tensile test based on ASTM E8 was performed to evaluate joints strength using a universal testing machine (Shimadzu: EHF-EF200kN) at a cross head speed of 1 mm/min at room temperature. Before fatigue test, all fatigue specimens were manually polished using emery paper. The fatigue test based on ASTM E466 was performed to evaluate the fatigue endurance limit at room temperature using fatigue test machine (MTS System Corporation: 661.20F-02) with a capacity of 50 kN under a sinusoidal wave with a frequency of 10 Hz and a stress ratio of $R = 0.1$ in tension-tension mode. In fatigue test, 60% of ultimate tensile strength ($0.6\sigma_T$) was chosen at the first-stage stress level.
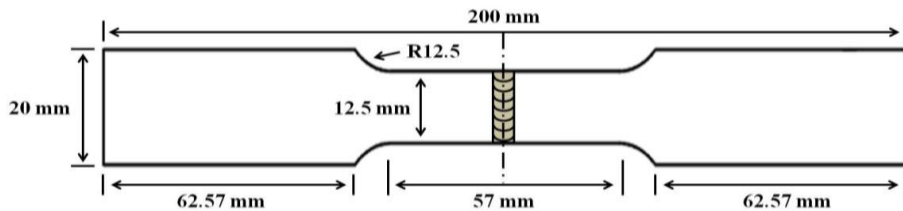
(a) Tensile specimen
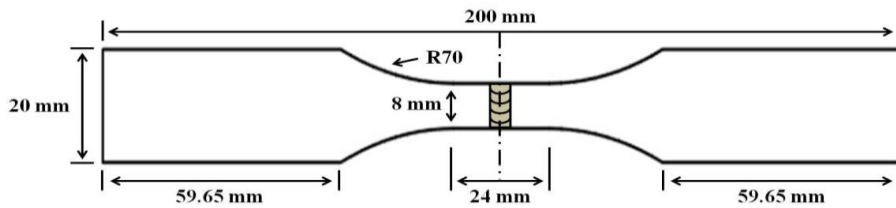
(b) Fatigue specimen

Fig. 2-2   *Dimension of standard specimen; (a) Tensile specimen and (b) Fatigue specimen*

32

The Micro Vickers Hardness (Mitutoyo: AKASHI HM112) was measured along the middle line of transverse cross section with a load of 500 g and dwell time of 10 s. The erichsen cupping test (Smtest in Korea: SMB-006-30T) based on ASTM 643-09 was carried out to evaluate the formability of joints using tip of the punch of 10 mm at test speed of 20 mm/min. The erichsen cupping specimen with length of 100 mm and width of 100 mm were cut from butt-welded plates using wire-cutting machine.

(b) Metallurgical test

All samples for metallurgical observation were polished from emery papers of 400 to 4000 grit and diamond suspension of 9, 3 and 1 micron. After polishing, the metallographic samples were etched in 5% Nital reagent (100 ml Ethanol+5 ml nitric acid) for 5 s and Tucker's reagent (45 ml HCI+15 ml HNO3+15 ml HF+25 ml distilled water) for 10 s in sequence to observe the macrostructure and microstructure using optical microscope (Olympus SZ61 and BX51M with I-solution imaging program). The thickness and composition of interfacial layer between Al and Fe were characterized by scanning electron microscopy with energy dispersive spectrometry (EDS) using beam energy of 15 kV and magnification of x5,000. In addition, the phase of intermetallic compound formed at joint interface was identified by X-ray diffractometer using monochromatic CuKa radiation.

2.3 FSW process

2.3.1 Optimization of welding process parameters

In order to verify the effect of pin-offset on material flow and surface quality of FS welds, the experiments were performed by varying pin-offset Fig. 2-3 shows surface appearance of FS welds with pin-offset ranging from 0 mm to 0.9 mm at rotation speed of 300 rpm and at travel speed of 60 mm/min. The frictional heat generated between tool shoulder and workpiece thermally softens material under high pressure and material experiences severe plastic deformation which can lead to the formation of excessive flash. Excessive formation of flash was observed in all FS welds due to difference in workpiece thickness of aluminium alloy and steel. With the decrease of pin-offset, which was shifted to steel side, small pin-offset relatively resulted in higher heat input and lead to a large amount of flash compared with other FS welds. With respect to effect on surface quality, FS welds exhibited the coarse surface appearance when pin-offset gradually increased into steel side. On the other hand, FS welds obtained under pin-offset of 0 mm indicated smooth surface appearance because deformation resistance of steel relatively occurs under small pin-offset [8-10].
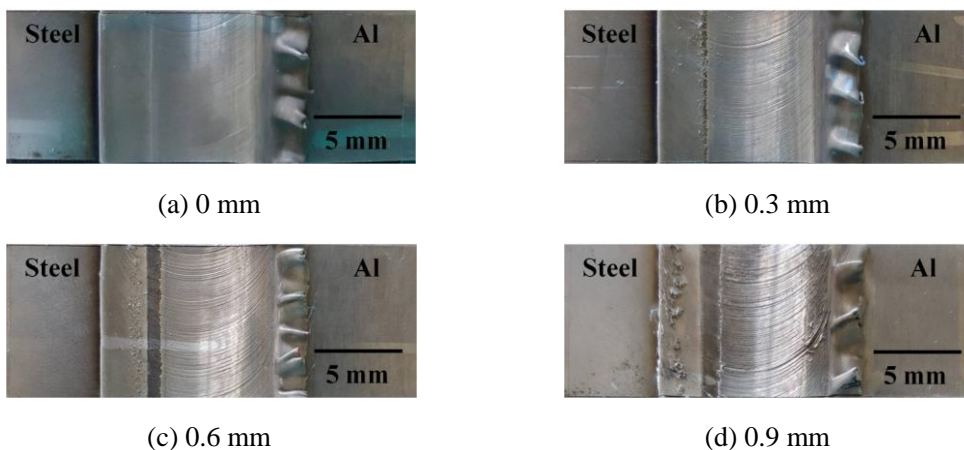

(a) 0 mm

(b) 0.3 mm

(c) 0.6 mm

(d) 0.9 mm

Fig. 2-3   *Surface appearance of FS welds under different pin-offsets; (a) 0 mm, (b) 0.3 mm, (c) 0.6 mm and (d) 0.9 mm*

34

2.3.2 Development of welding process

The bead profile views of FS welds under various travel speeds with at rotation speeds ranging from 300 to 500 rpm, 0.8 mm plunge depth and 0.9 mm pin-offset are shown in Table 2-3. When travel speed was increased from 60 to 120 mm/min, the bead width of FS welds was significantly decreased by lower heat input resulting in insufficient surface material flow. The elongated steel strip formed at advancing side in the bead of FS welds exhibited a smaller width with increasing travel speed. This formation of elongated steel strip, which is induced by forging action, was generated in initial plunging stage of pin inserted into dissimilar materials due to different thicknesses between aluminium alloy and steel. Moreover, smooth bead morphology was observed at lower travel speed of 60 mm/min in correspondence with weld pitch of v/ω that indicates a ratio of travel speed (v) to rotational rate (ω). This weld pitch represents the inverse of heat input. It is obvious that the energy generated per unit length of weld increases with decreasing weld pitch.

Table 2-3   Surface appearance of FS welds with different travel speeds and rotation speeds
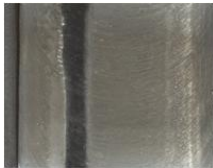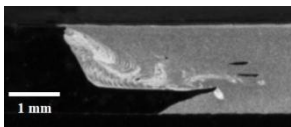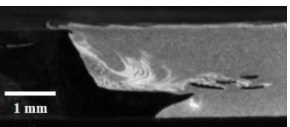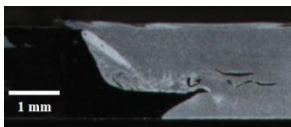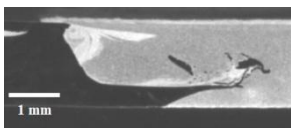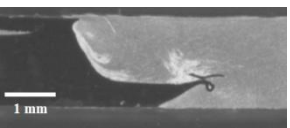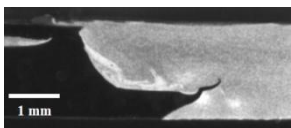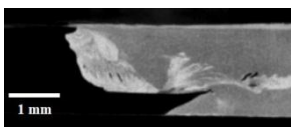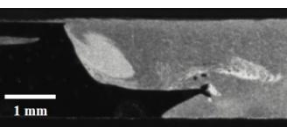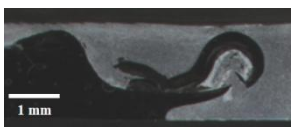
Variables		Travel speed (mm/min)		
		60	**90**	**120**
Rotation speed (rpm)	**300**			
	400			
	500			

Table 2-4 shows the macrostructure views of FS welds with different travel speeds and rotation speeds. From the observation of macrostructure, no defects such as tunnel and crack were observed at joint interface. The steel fragments with irregular shape and size at retreating side (Al side) were distributed by stirring action of pin. This steel fragments scattered in the Al matrix could be expected to be partially beneficial and acts as reinforcement in softer Al matrix [11]. The influence of steel fragment in the Al matrix on joint strength will be discussed with tensile test results. On the other hand, the reduction of effective thickness ranging from 1.81 mm to 1.99 mm occurred in all FS welds due to difference in thickness of two materials. This reason tends to be related to heat input, which is indicated as the ratio (ω/v) of rotation speed (ω) to travel speed (v). In present study, the ratio range of ω /v is from 2.5 to 8.33. It was revealed that effective thickness with a large amount of burr formed at aluminium alloy side decreased with the increase of heat input by decreasing travel speed at constant rotation speed. Also, FS welds have a weakness presenting the unwelded zone at bottom region of joint interface when the travel speeds are varied from 90 to 120 mm/min at all rotation speeds. This is meaning that the lack of plasticization caused by insufficient friction heat generation attributes to low heat input with increase in travel speed.

Table 2-4   Cross section view of FS welds with different travel speeds and rotation speeds

Variables		Travel speed (mm/min)		
		60	**90**	**120**
Rotation speed (rpm)	**300**			
	400			
	500			

2.4 Laser Assisted FSW Hybrid process

2.4.1 Optimization of welding process parameters

In order to observe the effect of laser power on width and depth of preheating zone, the experiment of bead on plate (BOP) were carried out with variation ranging from 150 W to 250 W at constant travel speed of 60 mm/min. Table 2-5 shows the surface appearance and macrostructure characteristics in bead on plate experiment with varying laser power of 150 W, 200 W and 250 W. With the increase of laser power, the width and depth of preheating zone relatively increased at constant travel speed. In case of laser power of 250 W, the deepest penetration is observed in cross section of macrostructure, but this is improper due to high heat input with large deformation of workpiece, which may be resulted in excessive thermal range at joint interface of dissimilar welds.

Table 2-5   Surface appearance and cross section characteristics with varying laser power
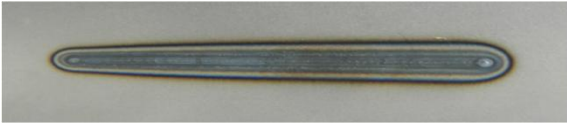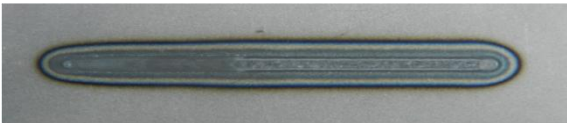
		Bead appearance	Cross section
Laser power (W)	**150**		
	200		
	250		

Fig. 2-4 shows the temperature history ranging from 150 W to 250 W at constant travel speed of 60 mm/min. Similar to macrostructure characteristics, with the increase of laser power, the maximum temperature increased. The maximum temperatures measured at central location of transverse cross section in welding direction were approximately 234 ℃, 325 ℃ and 374 ℃, respectively. In present study, considering macrostructure and measured temperature, the optimal parameter of laser power in laser assisted friction stir welding was selected as 200 W.
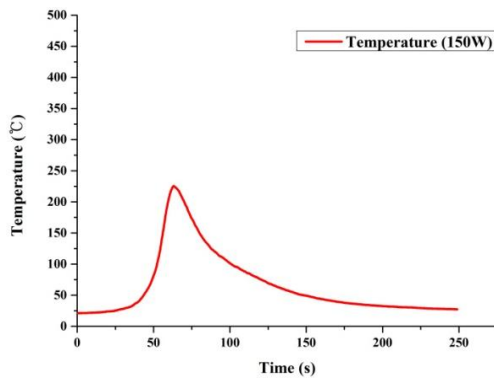
(a) 150 W
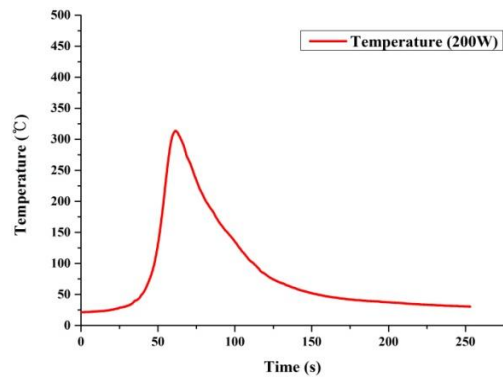
(b) 200 W
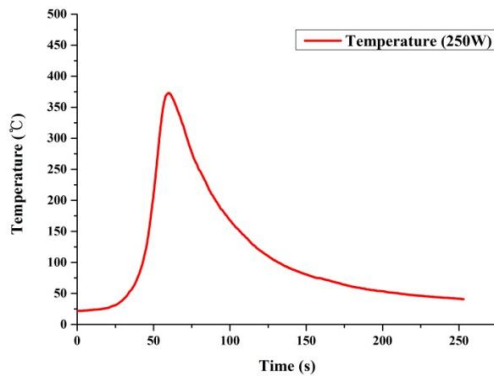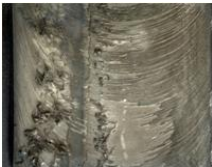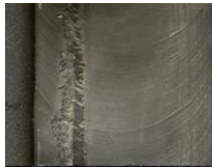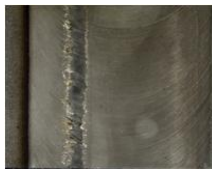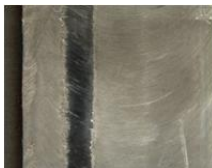
(c) 250 W

Fig. 2-4   *Temperature histories ranging from 150 W to 250 W at constant travel speed of 60 mm/min; (a) 150 W, (b) 200 W and (c) 250 W*

38

2.4.2 Development of welding process

Table 2-6 shows the bead profile views of LAFS welds under various travel speeds at rotation speeds ranging from 300 to 500 rpm, 0.8 mm plunge depth, 0.9 mm pin-offset and laser power of 200 W. This table exhibits that bead quality of welds associated with surface material flow was enhanced by decreasing travel speed. When travel speed increased from 60 to 120 mm/min at various rotation speeds, the bead width of LAFS welds was significantly decreased. This reduction in bead width significantly depends on heat input. It is seen from Table 2-6 that no specific surface defects such as surface tunnel (or groove) and voids were observed. These defects are likely to be caused by insufficient heat generation and non-uniform interned material in the stir zone under inappropriate process parameters. Similar to conventional FS welds, the elongated steel strip formed at advancing side was observed in all dissimilar joint due to difference in material thickness between aluminium alloy and steel.

Table 2-6   Surface appearance of LAFS welds with different travel speeds and rotation speeds

Variables		Travel speed (mm/min)		
		60	90	120
Rotation speed (rpm)	300			
	400			
	500			

As shown in Table 2-6, by increasing travel speed ranging from 60 mm/min to 120 mm/min, the width of the elongated steel strip was significantly decreased. Higher rotation speed results in a wider width of the elongated steel strip. This could be explained from the aspect of heat generation between workpiece and tool shoulder because the crucial welding parameters that influence heat generation are travel speed and rotation speed.

Table 2-7 shows the macrostructures of cross-sections obtained by LAFS welds. As seen in Table 2-7, no defects such as internal tunnel and crack were observed at joint interface and stir zone. The steel fragments scattered in the Al matrix were irregularly distributed in the nugget zone by stirring action. In the advancing steel side, the joint interface tilted with distinct inclination angle between aluminium alloy and steel, which is larger than the original angle of tool pin, can be observed. It is seen from Table 2-7 that this inclination angle of joint interface decreased with the increasing travel speed ranging from 60 mm/min to 120 mm/min and higher rotation speed resulted in smaller angle. The curved interface became to be concave shape by increasing the rotation speed ranging from 300 rpm to 500 rpm at constant travel speed of 60 mm/min.

Table 2-7   Cross section view of LAFS welds with different travel speeds and rotation speeds
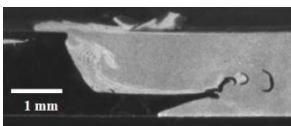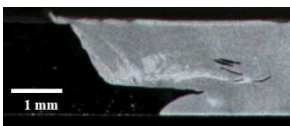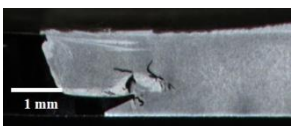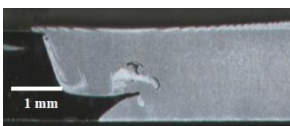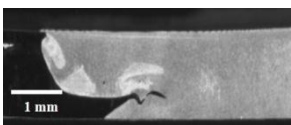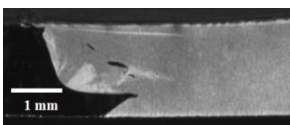
Variables		Travel speed (mm/min)		
		60	**90**	**120**
Rotation speed (rpm)	**300**			
	400			
	500			

40

Fig. 2-5 shows clear effect of heat generation on inclination angle of interface, effective thickness and material flow in dissimilar joint. It is obvious that decreasing travel speed increase the heat generation and larger frictional heat will be generated between tool shoulder and workpiece. Referring to the magnified macrostructure of Table 2-7, the lower heat generation with increasing travel speed leads to insufficient stirring and lack of materials plastic flow causing unwelded zone in Fig. 2-5(c) within a circle. It is necessary that the unwelded zone in dissimilar welds, which have an influence on joint property, should be improved by preheating source enabling improved material flow to enhance the sufficient plasticization [8, 12-13]. Higher travel speed results in less amount of frictional heat conducted to bottom region and more non-uniform temperature distribution in the nugget zone due to difference in thickness between aluminium alloy and steel. Consequently, the difference in steel flow stress between upper and bottom region is larger resulting in a more curved interface shape and the steel deformed at upper region will increase the effective thickness in the stir zone, as shown in Fig. 2-5 within red square [9].

(a) 60 mm/min	(b) 90 mm/min	(c) 120 mm/min
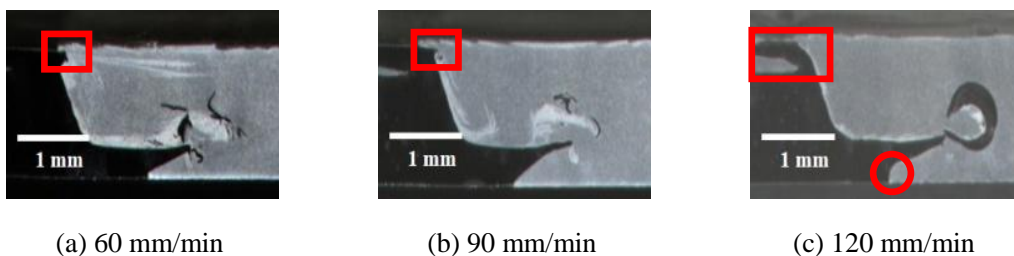
Fig. 2-5   ***Cross section view of LAFS welds produced with different travel speeds at rotation speed of 400 rpm; (a) 60 mm/min, (b) 90 mm/min and (c) 120 mm/min***

2.5 Conclusions

In present study, dissimilar joining of different thicknesses with 2.5 mm thick AA5052-H32 and 1.4 mm thick DP590 steel has been successfully achieved by conventional friction stir welding and laser assisted friction stir welding. Moreover, the crucial effect of process parameters on surface quality material flow and welding defect of FS welds and LAFS welds has been investigated and compared. The results can be summarized as follow:

- ➢ Higher travel speed results in less amount of frictional heat conducted to bottom region and more non-uniform temperature distribution in the nugget zone due to difference in thickness between aluminium alloy and steel. The difference in steel flow stress between upper and bottom region is larger resulting in a more curved interface shape and the steel deformed at upper region will increase the effective thickness in the stir zone.

- ➢ In laser assisted friction stir welding process, the elevated temperature by laser preheating can reduce the steel deformation resistance compared with friction stir welding process. This preheating effect can contribute to both greater amount of conduction heat and plastic deformation heat and promote the penetration of aluminium stirred into steel side. Therefore, the material flow is significantly enhanced by laser preheating.

- ➢ From the observation of macrostructure, no major defects such as tunnel and crack were observed at joint interface of FS welds and LAFS welds. Unwelded zone of FS welds was observed at travel speed of 90 mm/min and 120 mm/min, while it was only observed at travel speed of 120 mm/min in LAFS welds. It can be inferred that material flow was relatively enhanced under elevated temperature by laser preheating. This result shows that LAFSW owns wider process window.

- ➢ Consequently, it is necessary that the unwelded zone in dissimilar welds, which have an influence on joint property, should be improved by preheating source enabling improved material flow to enhance the sufficient plasticization.

Reference

[1]   Anand, D., Chen, D.L., Bhole, S.D., Andreychuk, P., Boudreau, G., 2006. Fatigue behavior of tailor (laser)-welded blanks for automotive applications. Mater. Sci. Eng. A-struct. Mater. Prop. Microstruct. Process. 420, 199-207

[2]   Feistauer, E.E., Bergmann, L.A., Barreto, L.S., Dos Santos, J.F., 2014. Mechanical behavior of dissimilar friction stir welded tailor welded blanks in Al-Mg alloys for marine applications. Mater. Des. 59, 323-332

[3]   Yoo, S. J., Kim, K. H., Ro, C. S., Bang, H. S., Bang, H. S., 2018. Numerical analysis for thermal characteristics comparison of Al5052-H32 TWB friction stir welded joints by varying workpiece tilting angle. Autumn Conference of the Korean Welding and Joining Society, 238

[4]   Choi, E. G., Kim, K. H., Kim, J. H., Bang, H. S., Bang, H. S., 2017. Welding characteristics of dissimilar thickness TWB friction stir welding upon welding parameters. Proceedings of KSPE 2017 Autumn Conference, 235

[5]   Piccini, J.M., Svoboda, H.G., 2017. Tool geometry optimization in friction stir spot welding of Al-steel joints. J. Manuf. Process. 26, 142-154

[6]   Kim, K. H., Ro, C. S., Bang, H. S., Bang, H. S., 2014. Evaluation of corrosion resistance of hybrid friction stir welded joints in dissimilar materials (SS400/AA6061-T6). Abstracts of the 2014 Autumn Annual Meeting of Korean Welding and Joining Society, 60

[7]   Kim, K. H., Bang, H. S., Bang, H. S., Choi, I. C., Hong, S. M., Kim, C. H., 2017. Weldability of hybrid friction stir welded joints for tailor welded blanks of dissimilar materials (Al/Steel) in CTR FLR COMPL. KSAE 2017 Annual Spring Conference, 954

[8]   Watanabe, T., Takayama, H., Yanagisawa, A., 2006. Joining of aluminum alloy to steel by friction stir welding. J. Manuf. Process. Technol. 178, 342-349

[9]   Liu, X., Lan, S., Ni, J., 2014. Analysis of process parameters effects on friction stir welding of dissimilar aluminum alloy to advanced high strength steel. Mater. Des. 59, 50-62

[10]   Derazkola, H. A., Aval, H. J., Elyasi, M., 2015. Analysis of process parameters effects on dissimilar friction stir welding of AA1100 and A441 AISI steel. Sci. Technol. Weld. Join. 20, pp. 553-562

[11]   Ramachandran, K.K., Murugan, N., Shashi Kumar, S., 2015. Friction stir welding of aluminum alloy AA5052 and HSLA steel. Weld. J. 94, 291-300

[12]   Bang, H. S., Bang, H. S., Jeon, G. H., Oh, I. H., Ro, C. S., 2012. Gas tungsten arc welding assisted hybrid friction stir welding of dissimilar materials Al6061-T6 aluminum alloy and STS304 stainless steel. Mater. Des. 37, 48-55

[13]   Uzun, H., Donne, C. D., Argagnotto, A., Ghidini, T., Gambaro, C., 2005. Friction stir welding of dissimilar Al 6013-T4 to X5CrNi18-10 stainless steel. Mater. Des. 26, 41-46

Chapter 3.

Mechanical and Metallurgical Evaluation of Laser Assisted FSW Hybrid Welded Joints

3.1 Introduction

Hybrid Friction Stir Welding (HFSW), which combines the process of friction stir welding and preceding preheating source laser or Gas Tungsten Arc Welding (GTAW), is known to offer several advantages [1-3]. The remarkable advantage is that the preceding preheating source can play an important role in improvement on better mechanical property, material flow and welding speed compared with friction stir welding process. The other advantage is reduction in tool wear [4]. Therefore, in present chapter, the aim of this work intends to assess joint properties and metallurgical evolution of dissimilar welds with different thicknesses in conventional friction stir welding and laser assisted friction stir welding. The joint performance has been investigated through critical analysis on correlation between the mechanical properties and microstructures of dissimilar welds in relation to the process parameters. Moreover, the side upper of automotive component, which was combined in lightweight center floor module, has been manufactured by laser assisted friction stir welding under optimal process variables obtained in present study.

46

3.2 FSW Process

3.2.1 Mechanical characteristics

Fig. 3-1 shows the comparison of tensile strength of dissimilar joints fabricated above-mentioned parameters; at travel speed of 60-120 mm/min and rotation speed of 300-500 rpm. The highest tensile strength of FS welds is 178 MPa, which is obtained under conditions of travel speed of 60 mm/min and rotation speed of 500 rpm. Its joint efficiency reached approximately 79% of Al base metal. On the other hand, the tensile strength significantly decreased with the increase of travel speed ranging from 90 and 120 mm/min at all rotation speeds. At constant travel speed of 60 mm/min, which indicates the highest tensile strength at rotation speed ranging from 300 and 500 rpm, the effect of rotation speed on tensile strength has shown increasing tendency with the increase of rotation speed. These results obtained by tensile test of dissimilar joints show that higher heat input with increasing rotation speed and decreasing travel speed was contributed to higher tensile strength. The detailed reason for these results on effect of crucial parameters on tensile strength will be explained in accordance with macrograph analysis of fractured tensile specimen, in next paragraph.

Fig. 3-2 shows the macrograph of fractured surface presenting three types of failure modes of interface failure, TMAZ failure and mixed failure on interface + TMAZ, after tensile test. The tensile specimen fractured at joint interface of Al/Steel indicates the highest tensile strength compared with tensile specimen fractured at NZ. It can be inferred that the fracture path is propagating from interface of unwelded zone to large or small steel particle. These results obtained from tensile test reveal that steel particles have influence on joint strength and it is consistent with the result of macrostructure showing the presence of unwelded zone. The unwelded zone of bottom region in dissimilar joints acts as path of crack propagation during tensile test. Consequently, it is necessary that the unwelded zone at the welds root in dissimilar joints should be prevented by additional preheating source enabling material flow to enhance the sufficient plasticization.
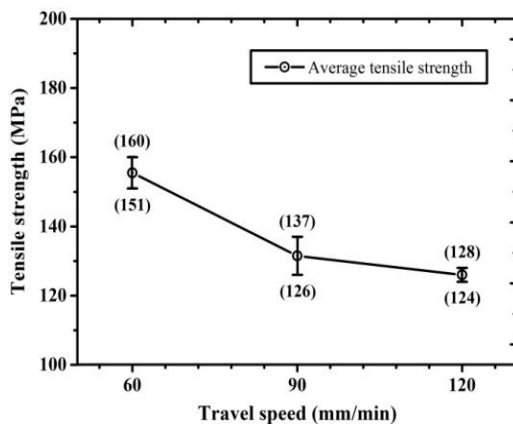
(a) 300 rpm
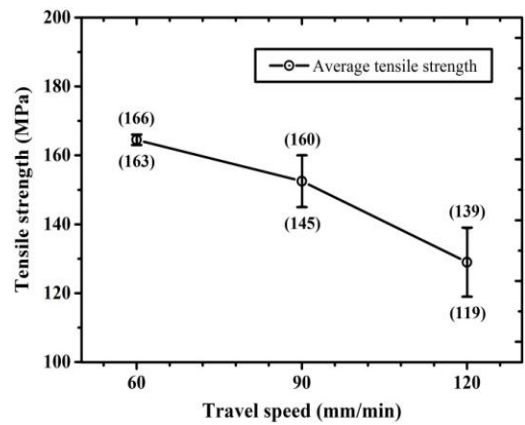
(b) 400 rpm
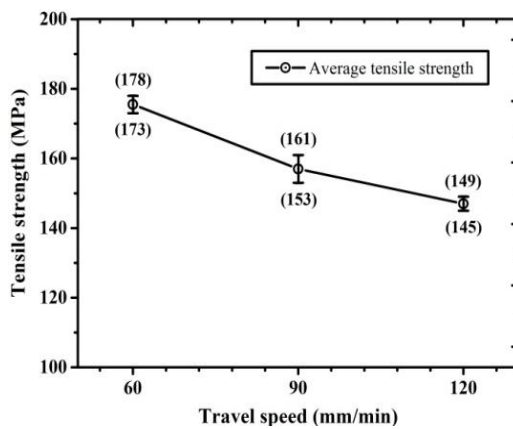
(c) 500 rpm

Fig. 3-1   The comparison of tensile strength of FS welds with different rotation speeds and travel speeds; (a) 300 rpm, (b) 400 rpm and (c) 500 rpm

48
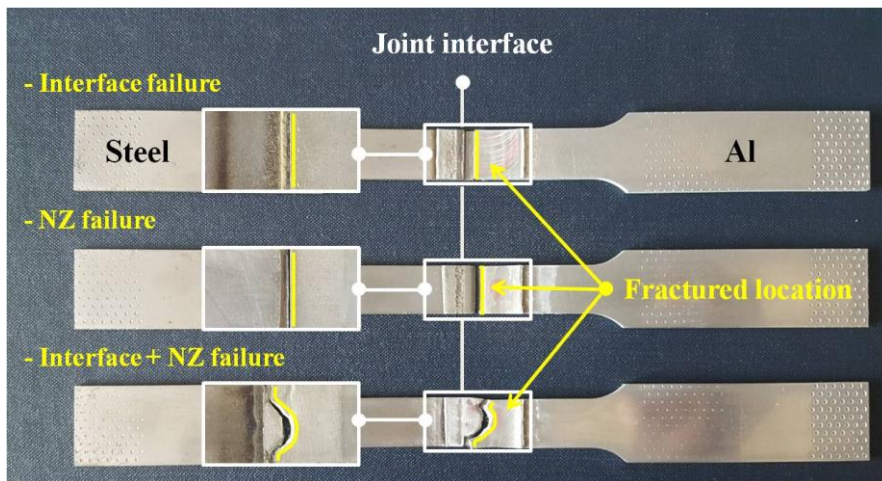
Fig. 3-2   ***Macrograph of fractured tensile specimen of FS welds***

Fig. 3-3 shows the hardness distribution measured along the middle line of transverse cross section of FS welds, which indicates the highest tensile strength after tensile test. The base metal hardness of Al5052-H32 and DP 590 steel used in present study have ranges of 54-57 HV and 192-198 HV, respectively. The hardness value at the steel side close to joint interface was significantly higher than that of steel base metal due to its high hardenability. However, there was no distinct difference in hardness value in advancing side of the steel. The average hardness value in the stir zone of the retreating side was slightly lower than that of the Al base metal. In particular, the hardness value in TMAZ of retreating side close to the stir zone (SZ) was significantly decreased. This localized decrement in hardness value is due to the softening caused by reduction in dislocation density, metallurgical recovery and annealing effect by thermal cycle during FSW (the softening zone is denoted by gray outline in Fig. 3-3). This phenomenon is also consistent with that of tensile test result indicating fracture of NZ close to the stir zone, which is lower tensile strength. However, this hardness distribution measured in the test specimen is obtained from the highest tensile strength after tensile test. It can be therefore inferred that small steel particle scattered in the stir zone act as reinforcement [5].

49
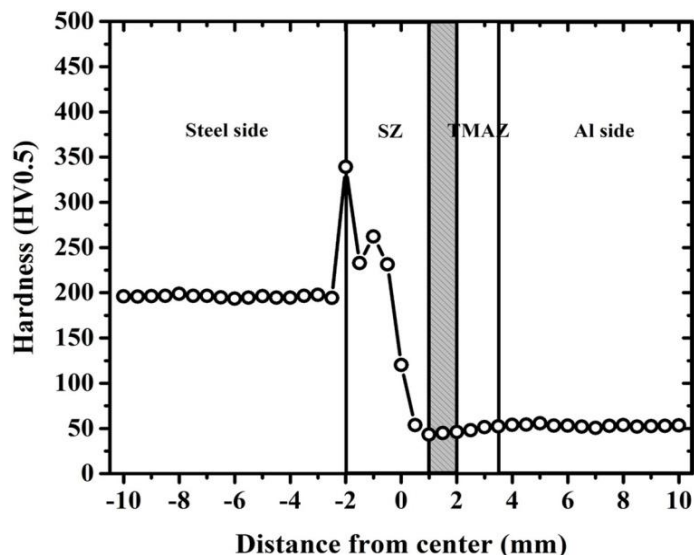
Fig. 3-3 **Hardness distribution of FS welds along the transverse middle line**
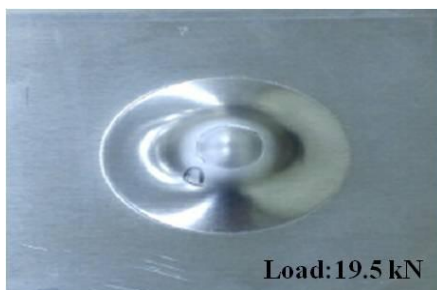
(a) Al base metal
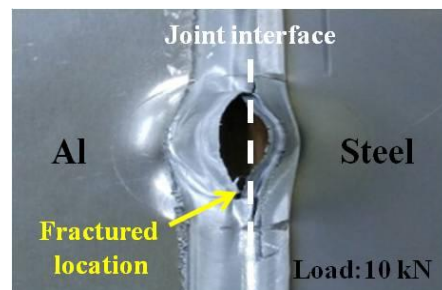
(b) FS welds

Fig. 3-4 **Macrograph of Al base metal and FS welds after Erichsen cupping test; (a) Al base metal and (b) FS welds**

In order to evaluate the formability of FS welds, the Erichsen cupping test was performed. Fig. 3-4 shows the test samples on Al base metal and FS welds after Erichsen cupping test. The test sample on FS welds was fractured under the 10 kN of the vertical sphere punch, which is

50

significantly lower than that of Al base metal. The rupture occurred along the joint interface of FS welds. This rupture seems to be more brittle at joint interface because it was drastically reduced the shift and load value of the vertical sphere punch due to mismatch of mechanical properties on dissimilar materials.

3.2.2 Metallurgical characteristics

Fig. 3-5 shows the back-scattered scanning electron (BSE) images of the joint interface between Al and steel produced at travel speed of 60 mm/min and rotation speed of 500 rpm. The results obtained from energy dispersive spectrometry (EDS) analysis are summarized in Table 3-1. Intertermetallic compound layer, where is distinct interfacial layer between steel (grey color) and aluminium alloy (dark color) can be distinguished was formed at joint interface, as shown in Fig. 3-5. As shown in Fig. 3-5(a), the microstructure of BSE image reveals that FS welds had visually internal micro defect-free, such as micro crack and void. The scattered steel fragments consisting of 87.8 at.% for Fe, 9.69 at.% for C, 2.34 at.% for Mn and 0.17 at.% for P were distributed near joint interface. It is seen from Fig. 3-5(b) that thin intermetallic compounds layer with thickness of less than 1 μm was formed at joint interface and was also almost uniform. This interfacial layer had elemental compositions on 28.52 at.% for Fe and 71.48 at.% for Al. According to the Fe-Al equilibrium phase diagram, the EDS analysis result for elemental composition indicates that the intermetallic compounds layer formed at the joint interface consist of Al-rich. The X-ray diffraction (XRD) analysis was used to determine the intermetallic phase on interfacial layer. Fig. 2-10 shows the XRD spectrum of FS welds. It is seen from Fig. 3-7 that intermetallic phase of Fe_4Al_{13} are detected at joint interface.
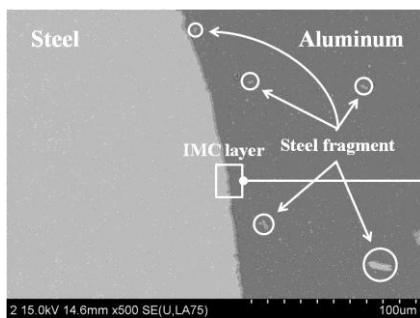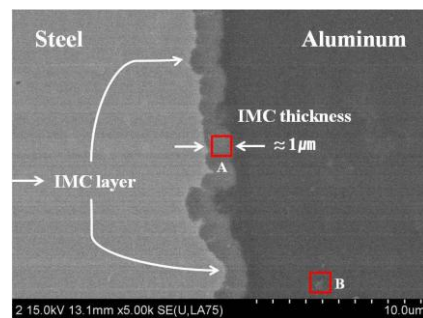
(a) Microstructure near joint interface   (b) Magnification of (a)

Fig. 3-5   SEM BSE images of microstructure near joint interface; (a) Microstructure near joint interface and (b) Magnification of (a)

(a) Interfacial layer   (b) Steel fragment
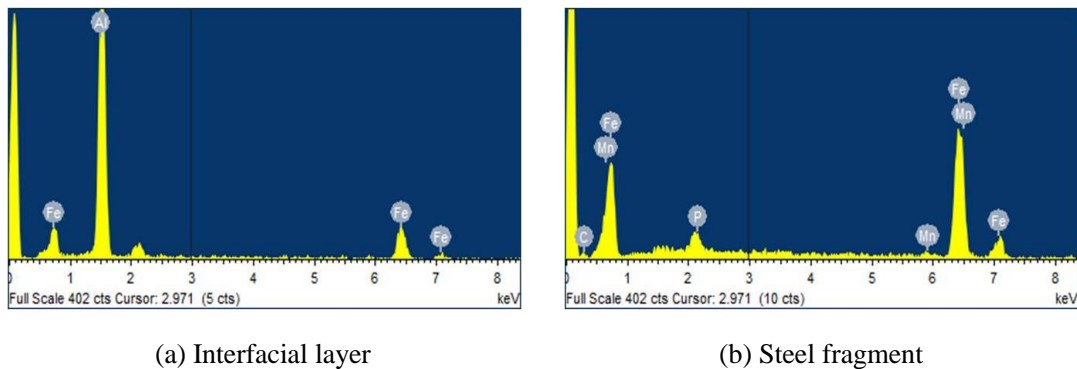
Fig. 3-6   *SEM-EDS spectrum; (a) Interfacial layer and (b) Steel fragment*

Table 3-1   **SEM-EDS results on composition analysis of different areas of dissimilar FS welds; (A) Interfacial layer and (B) Steel fragment**

Area	at.%				
	Fe	Al	C	Mn	P
Point (A) (Interfacial layer)	28.52	71.48	-	-	-
Point (B) (Steel fragment)	87.8	-	9.69	2.34	0.17
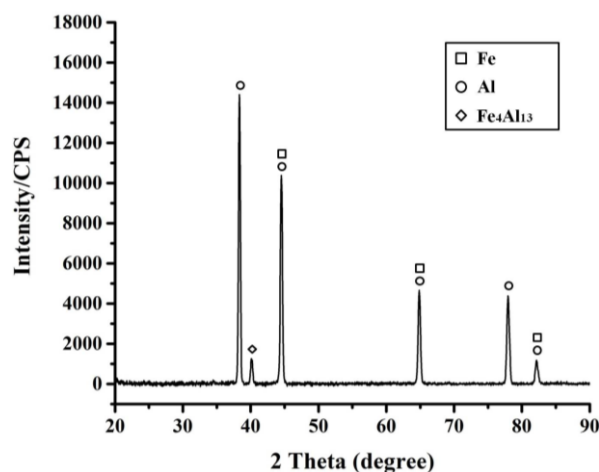
Fig. 3-7   *XRD spectrum of FS welds*

53

3.3 Laser Assisted FSW Process

3.3.1 Mechanical characteristics

Fig. 3-8 shows the comparison of tensile strength of LAFS welds fabricated under process parameters; at travel speed of 60-120 mm/min, rotation speed of 300-500 rpm and laser power of 200 W. The highest tensile strength of LAFS welds is 193 MPa, which is obtained under conditions of travel speed of 60 mm/min and rotation speed of 400 rpm. Its joint efficiency reached approximately 88% of Al base metal. It is seen from Fig. 3-8 that maximum tensile strength of LAFS welds increased when the travel speed ranging from 60 mm/min to 90 mm/min increased and then tensile strength decreased at travel speed of 120 mm/min. This result demonstrates that the tendency is different compared with result of tensile strength obtained in conventional FS welds. Therefore, it can be inferred that the increase in tensile strength is attributed to the sufficient material flow by adopting the laser preheating. However, the tensile strength of LAFS welds produced at rotation speed of 400 rpm decreased with the increase of travel speed ranging from 60 to 120 mm/min similarly to conventional FS welds. This reason on this tendency will be discussed next section on microstructure of joint interface.

Fig. 3-9 shows macrograph of fractured tensile specimen of LAFS welds after tensile test. There are three distinct features indicating interface failure (mainly occurred at travel speed of 60 mm/min), interface + NZ (nugget zone) failure (mainly observed at travel speed of 120 mm/min) and TMAZ (thermo-mechanically affected zone) failure (observed at travel speed of 60 mm/min and rotation speed of 400 rpm). The most frequent failure mode occurred in present study is interface failure. In this failure mode, the crack started at upper region of LAFS welds and then propagated along the joint interface. Hence, the dissimilar LAFS welds fractured in this failure mode will be remarkably influenced by intermetallic compounds. On the other hand, this failure mode is significantly different than that of conventional FS welds on the final fracture path. This result indicates that sufficient material plastic flow is enhanced by laser preheating steel. In interface + NZ failure mode, which is mainly obtained at the highest travel speed, this mode results in the lowest tensile strength among the three failure modes because the tensile specimen fractured

54

at interface + NZ exhibits the presence of large steel particle and unwelded zone in the bottom region. It is also consistent with result of macrostructure observation. It can see from Fig. 3-9 that TMAZ failure mode is the most acceptable mode resulting in the highest tensile strength of 193 MPa, which was approximately 88% of Al base metal.
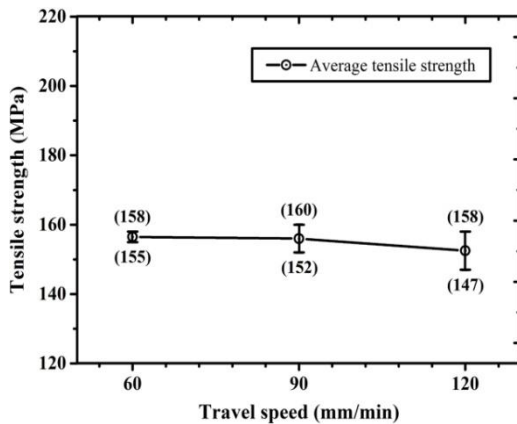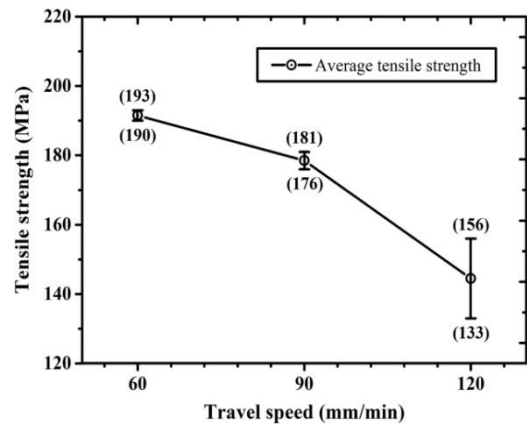
(a) 300 rpm   (b) 400 rpm
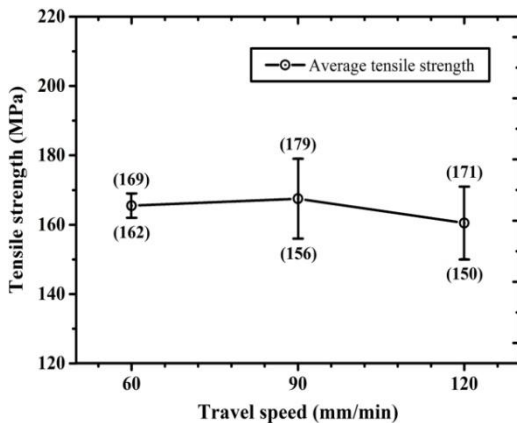
(c) 500 rpm

Fig. 3-8   ***The comparison of tensile strength of LAFS welds with different rotation speeds and travel speeds; (a) 300 rpm, (b) 400 rpm and (c) 500 rpm***
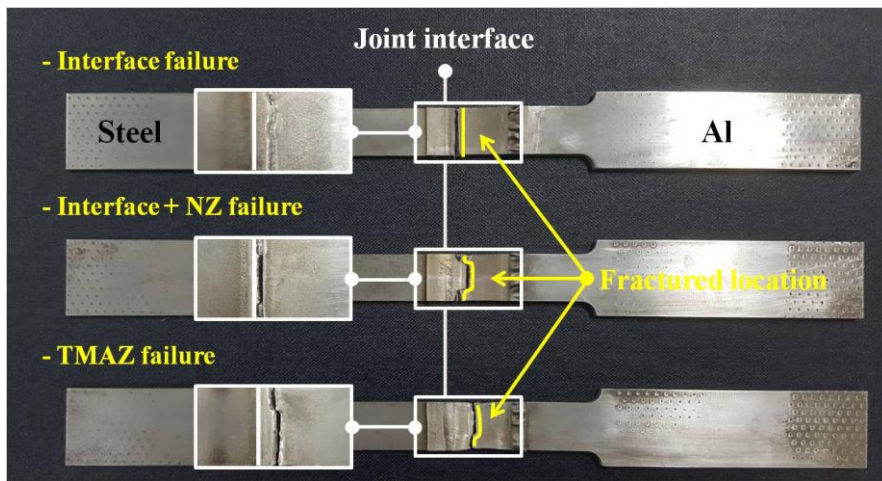
Fig. 3-9   Macrograph of fractured tensile specimen of LAFS welds
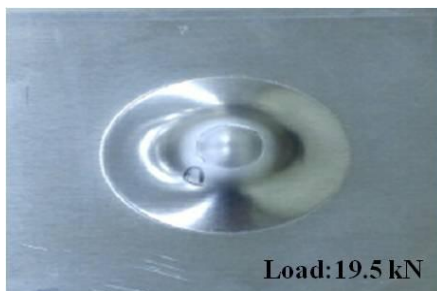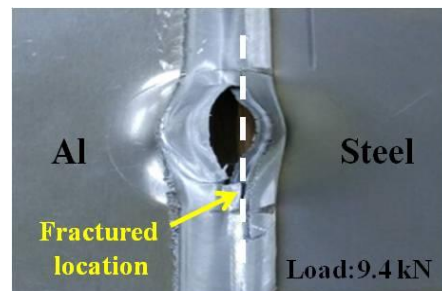
(a) Al base metal   (b) LAFS welds

Fig. 3-10   Macrograph of Al base metal and LAFS welds after Erichsen cupping test; (a) Al base metal and (b) LAFS welds

The Erichsen cupping test was performed to evaluate the formability of LAFS welds and to compare with that of FS welds. Fig. 3-10 shows the test samples on Al base metal and LAFS welds after Erichsen cupping test. The test sample on LAFS welds was fractured under the 9.4 kN, which is 6% and 52% lower than that of conventional FS welds and Al base metal, respectively. The

rupture occurred along the joint interface. The reason for this result is due to formation of thick intermetallic compounds compared with conventional FS welds. This rupture seems to be more brittle at joint interface because it was drastically reduced the shift and load value of the vertical sphere punch due to mismatch of mechanical properties on dissimilar materials.
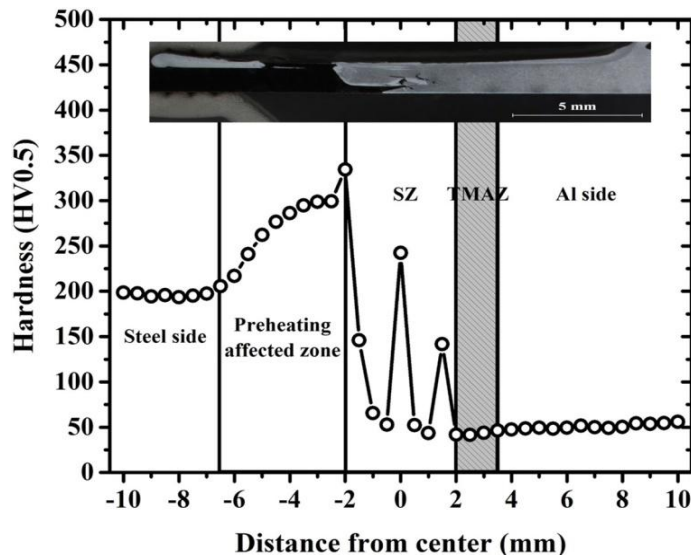
Fig. 3-11   Hardness distribution of LAFS welds along the transverse middle line

Fig. 3-11 shows the hardness distribution measured along the middle line of transverse cross section of LAFS welds, which indicates the highest tensile strength after tensile test. The base metal hardness value of Al5052-H32 and DP590 steel used in present study have ranges of 54-57 HV and 192-198 HV, respectively. It is seen from Fig. 3-11 that there are four distinct featured zones indicating the nugget zone (NZ), thermo-mechanically affected zone (TMAZ), preheating affected zone (PAZ) and base metal (BM) of steel and Al side on hardness distribution across the LAFS welds. The hardness value at steel side close to joint interface was significantly higher than that of steel base metal due to grain refinement and high hardenability and also increased in the PAZ of the advancing side by the microstructural variation on decrease in the ferrite matrix and the

57

increase in the martensite due to quenching effect after LAFSW. The minimum hardness value in the nugget zone of retreating side was about 48 HV, which indicates lower than that of base metal. The W pattern in the nugget zone was observed due to increase in hardness value by steel particle scattered. Similar to conventional FS welds, the localized decrement in hardness value by softening was observed at TMAZ close to NZ of 4 mm away from joint interface. The hardness distribution in LAFS welds has shown a little difference in softening area compared with conventional FS welds. The softening area of LAFS welds (5.5mm) was wider than that of FS welds (4 mm) away from joint interface due to higher heat input.

Fig. 3-12 shows the effect of process parameters on the axial force (F_Z) during welding stage under different values of travel speed and rotation speed. Note that the axial force during welding can be determined by monitoring the Z-axial output of motor. Based on the axial force versus time curve, there are four distinct features indicating plunging stage, dwelling stage, welding stage and pulling stage. In the plunging stage, the axial force curve is significantly increased in the beginning. Higher rotation speed, which can increase the material shear strain rate between the pin surface and material, can reduce the axial force in plunge stage. Hence, higher rotation speed is attributed to enhancing both plastic material flow and frictional heat generation. It is seen from Fig. 3-12 that positive relationship is evident between the axial force and the travel speed as well as between the axial force and rotation speed. The overall axial force reduced with decrease of travel speed.
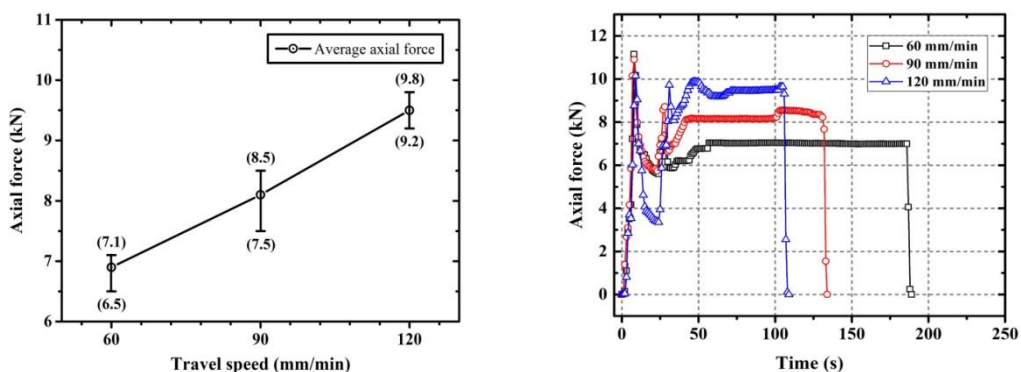
(a) 300 rpm (left: average axial force and right: axial force versus time curve)

58
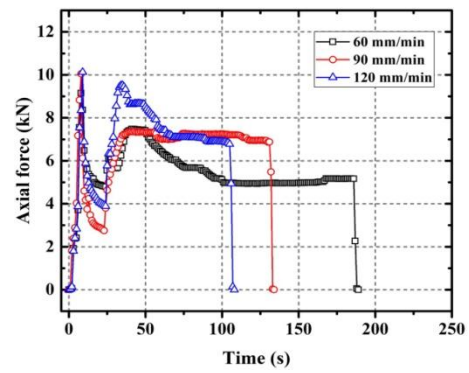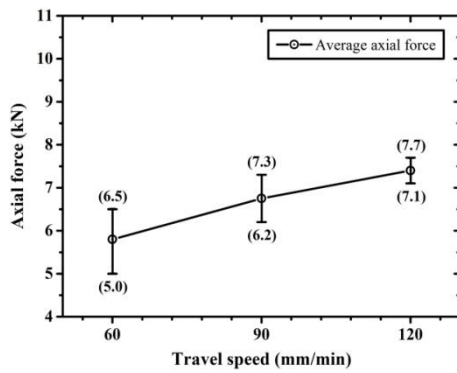
(b) 400 rpm (left: average axial force and right: axial force versus time curve)
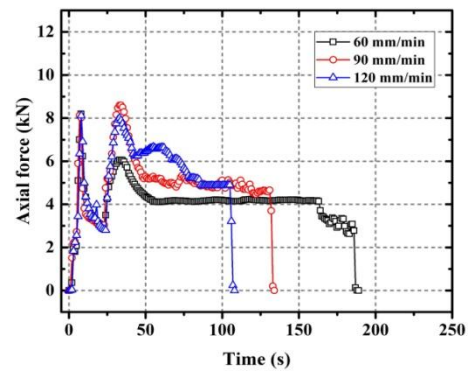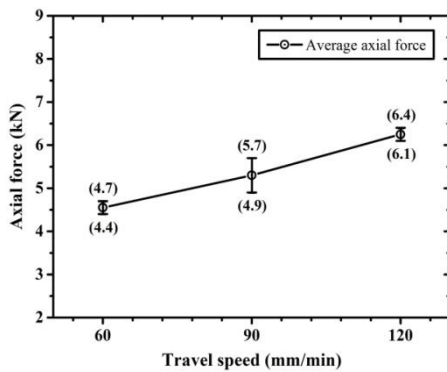
(c) 500 rpm (left: average axial force and right: axial force versus time curve)

Fig. 3-12   Effect of process parameters on the axial force during LAFSWelding stage; (a) 300 rpm, (b)400 rpm and (c) 500 rpm

Fig. 3-13 shows the stress-number of cycles to failure curve (S-N curve) of LAFS welds, which indicates the highest tensile strength after tensile test. Table 3-2 lists the detailed results of fatigue test for LAFS welds. The fatigue data of S-N curve can be expressed as the stress range ($\Delta\sigma$) versus the corresponding number of cycles to failure (N). In present study, the corresponding stress level is defined as the fatigue limit, when the number of cycles exceeds 2×10^{6} during fatigue test. Based on the stress range and fatigue life obtained from fatigue test, regression line was determined using the least square method, as shown in Fig. 3-13. The 60% tensile strength of LAFS welds was determined as the first-stage stress levels in fatigue test. The fatigue strength of LAFS welds was 63 MPa based on the regression line of the S-N curve at 2×10^{6} cycle. The relationship between stress level and fatigue life for welded joint is as follow:

$$(\Delta\sigma)^{m} \cdot N = C \tag{1}$$

where $\Delta\sigma$ is the stress range, N is the number of cycles to failure, m and C are the fitting constants related to the material properties in S-N curve.
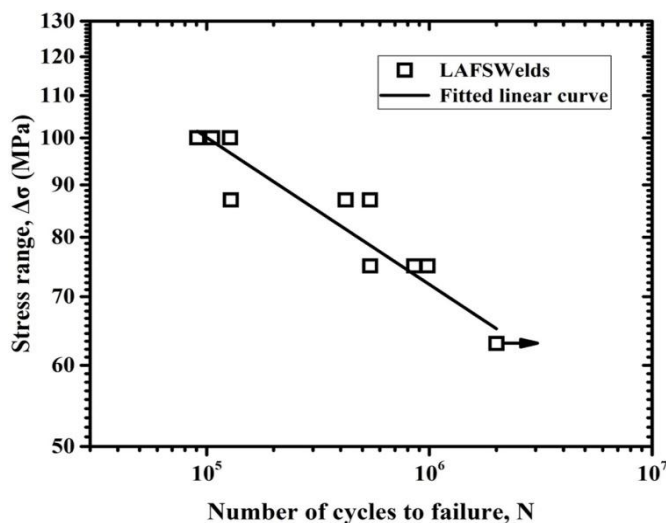
Fig. 3-13 ***Stress-Number of cycles to failure curve (S-N curve) of LAFS welds produced under welding parameter; at rotation speed of 400 rpm and at travel speed of 60 mm/min***

Table 3-2   Fatigue test results of LAFS welds

S_{max} (MPa)	$\Delta\sigma$ (MPa)	$(F_{max} - F_{min})/2$ (kN)	$(F_{max} + F_{min})/2$ (kN)	N_f $(\times 10^3)$
111	100	0.72	0.88	90,867
111	100	0.72	0.88	106,056
111	100	0.72	0.88	128,494
97	87	0.63	0.77	120,590
97	87	0.63	0.77	541,824
97	87	0.63	0.77	542,209
83	75	0.54	0.66	835,492
83	75	0.54	0.66	856,483
83	75	0.54	0.66	981,420
70	63	0.45	0.55	2,152,752
70	63	0.45	0.55	2,247,395
70	63	0.45	0.55	2,464,629

3.3.2 Metallurgical characteristics

Fig. 3-14 shows the SEM BSE images of LAFS welds at joint interface between steel and Al produced at travel speed of 60 mm/min and rotation speed of 400 rpm. The results obtained from composition analysis of energy dispersive spectrometry (EDS) are summarized in Table 3-3. It is seen from 3-14(a) that the minute fragments of Al-rich intermetallic compounds, which has the element compositions of 23.45 at.% for Fe and 76.55 at.% for Al were distributed close to interfacial layer in the retreating side. The thick interfacial layer of 5 μm with mixed intermetallic compounds of Fe-rich and Al-rich was formed at joint interface, as shown in Fig. 3-14(b). There is difference in formation of intermetallic compounds between conventional friction stir welding and laser assisted friction stir welding. The intermetallic compounds formed in conventional FS welds mainly was Fe_4Al_{13}, while the intermetallic compounds formed in LAFS welds was FeAl, Fe_2Al_5 and Fe_4Al_{13} obtained from X-ray diffraction (XRD) analysis, as shown in Fig. 3-16. Hence, compared with FS welds, this result indicates that laser preheating can enhance the diffusion process and promote the formation of greater amount of intermetallic compounds. Consequently, the elevated temperature by preheating laser significantly affects the formation and growth of intermetallic compounds.

(a) Microstructure near joint interface   (b) Magnification of (a)
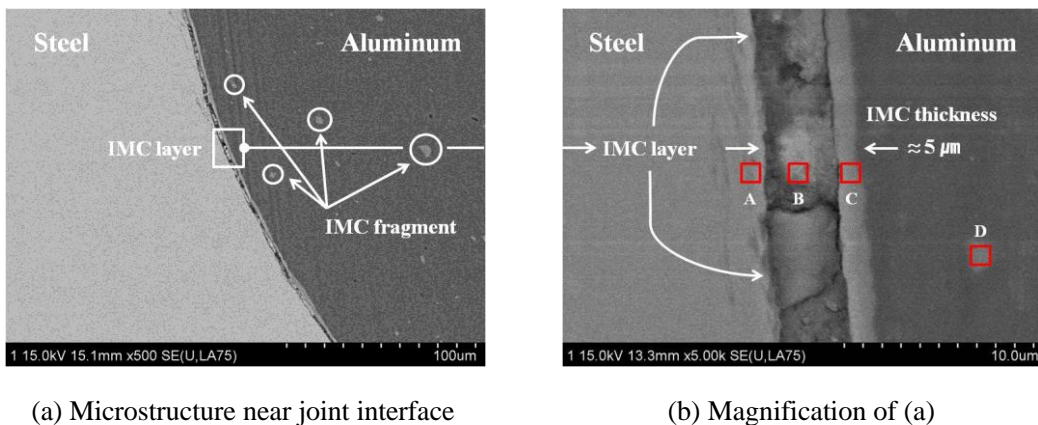
Fig. 3-14   SEM BSE images of microstructure near joint interface; (a) Microstructure near joint interface and (b) Magnification of (a)

(a) At steel side

(b) Fe-rich intermetallic compounds

(c) Al-rich intermetallic compounds

(d) Intermetallic compounds fragment
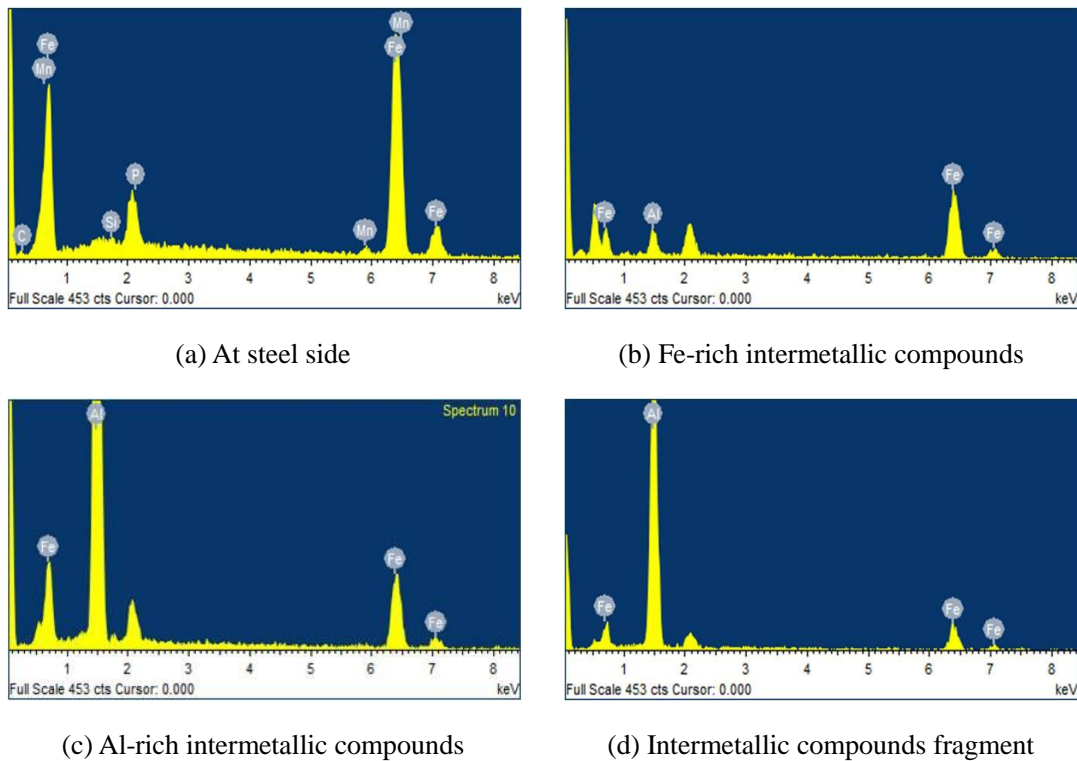
Fig. 3-15 *SEM-EDS spectrum; (a) At steel side, (b) Fe-rich intermetallic compounds, (c) Al-rich intermetallic compounds and (d) Intermetallic compounds fragment*

Table 3-3 **SEM-EDS results on composition analysis of different areas; (A) At steel side, (B) Fe-rich intermetallic compounds, (C) Al-rich intermetallic compounds and (D) Intermetallic compounds fragment**

Area	At.%					
	Fe	Al	C	Mn	Si	P
Point (A)	65.82	-	28.58	1.68	1.21	2.71
Point (B)	72.06	27.94	-	-	-	-
Point (C)	28.05	71.95	-	-	-	-
Point (D)	23.45	76.55				

63
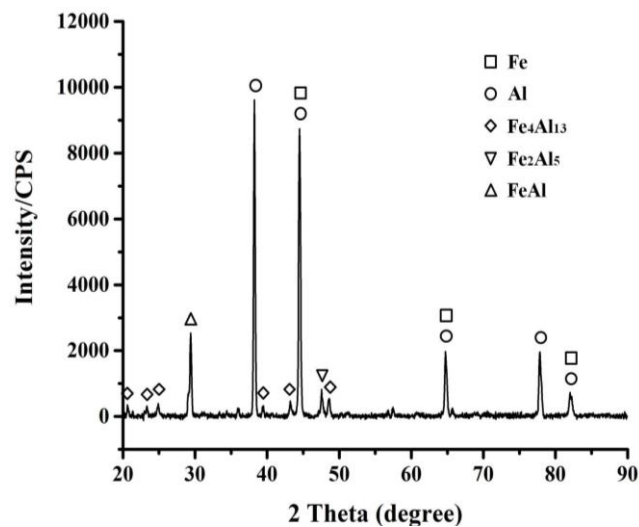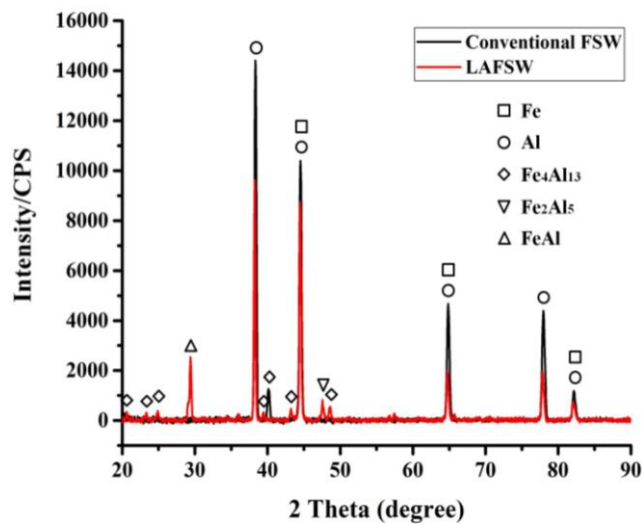
(a) LAFS welds

(b) Comparison of FS welds and LAFS welds

Fig. 3-16   XRD spectrum of LAFS welds; (a) LAFS welds and (b) Comparison of FS welds and LAFS welds

64

Fig. 3-17 shows fractured surface morphologies of three failure modes on interface, interface + NZ and TMAZ, which explained in chapter 3.2.1. It is seen in Fig. 3-17(a) that fractured surface on interface failure mode exhibits cleavage fracture in aluminium side, which is remarkably influenced by intermetallic compounds. This failure mode is mainly observed at lower travel speed of 60 mm/min. When travel speed is mainly 120 mm/min, the mixed mode indicating dimples and cleavages are observed in fractured surface on interface + NZ failure mode, as shown in Fig. 3-17(b).
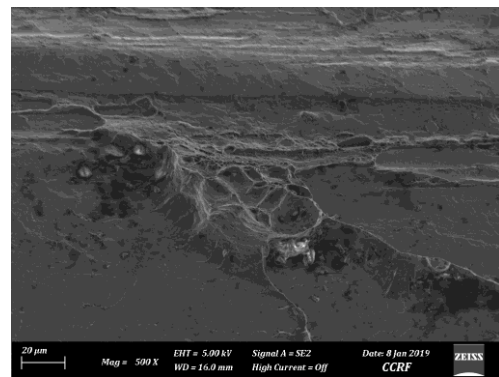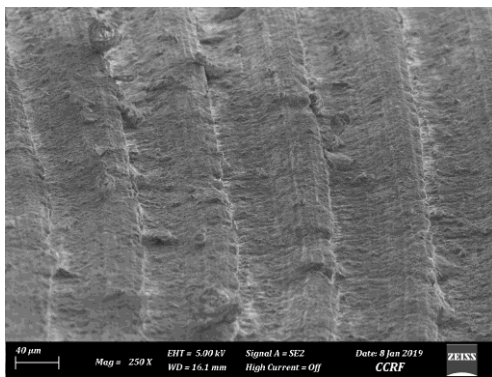
(a) Fractured surface on interface failure mode (left: aluminium side and right: steel side)
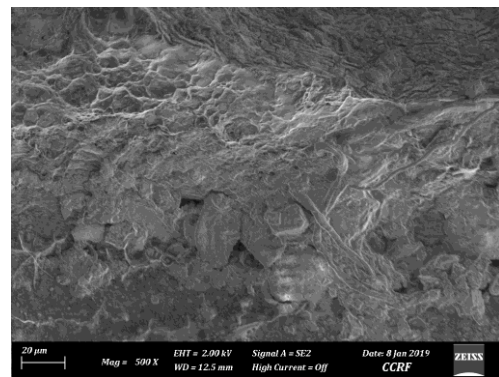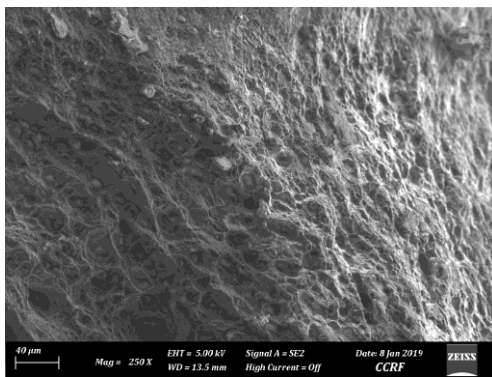
(b) Fractured surface on interface + NZ failure mode (left: aluminium side and right: steel side)
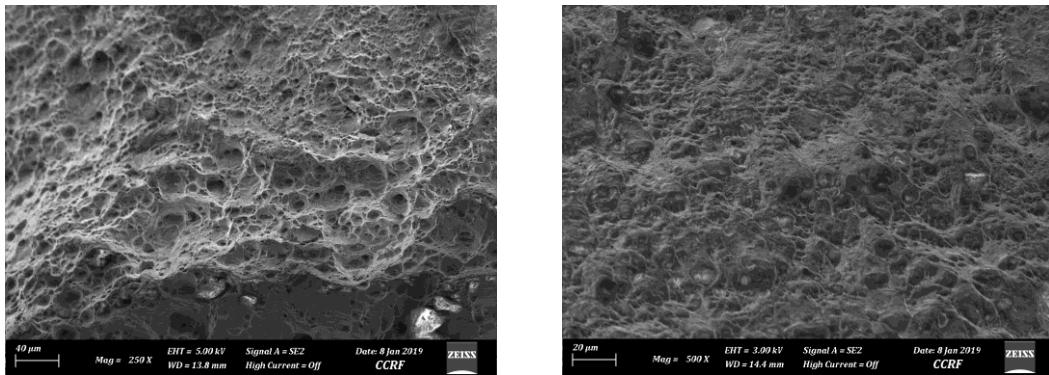
(c) Fractured surface on TMAZ failure mode (left: aluminium side and right: steel side)

**Fig. 3-17   *Fractured surface morphologies; (a) Fractured surface on interface failure mode,
(b) Fractured surface on interface + NZ failure mode and (c) Fractured surface
on TMAZ failure mode***

In case of TMAZ failure mode, which indicates the highest tensile strength, many large and deep
dimples with tearing edges associated with micropores are observed at the fractured surface of both
aluminium side and steel side, indicating the typical ductile fracture, as shown in Fig. 3-17(c). As
previously mentioned, intermetallic compounds scattered in aluminium matrix can act as
reinforcement. Intermetallic compounds with irregular size were observed in fractured surface of
aluminium alloy side, as shown in Fig. 3-18.
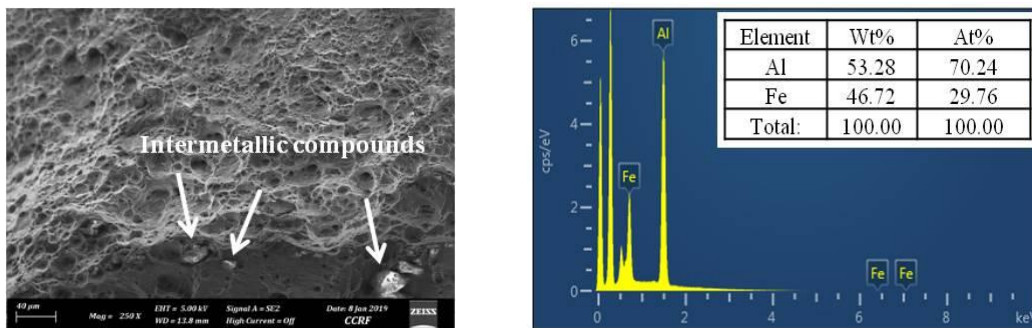
Fig. 3-18   *SEM-EDS result in fractured surface on intermetallic compounds*

Fig. 3-18 shows the result obtained from composition analysis of energy dispersive spectrometry on intermetallic compounds in fractured surface indicating TMAZ failure mode. This intermetallic compounds has the element compositions of 29.76 at.% for Fe and 70.24 at.% for Al. According to the Fe-Al equilibrium phase diagram, the EDS analysis result for elemental composition indicates intermetallic compound of Fe_2Al_5. It can be therefore inferred that this intermetallic compounds can take into account as reinforcement in dissimilar welds and then is contributed to enhancement in tensile strength.

4. Conclusions

In present study, dissimilar joining of different thicknesses with 2.5 mm thick AA5052-H32 and 1.4 mm thick DP590 steel has been successfully achieved by laser assisted friction stir welding. Moreover, the crucial effect of process parameters on mechanical properties and microstructure of LAFS welds has been investigated. The results can be summarized as follow:

➢ The highest tensile strength of FS welds produced under conditions of travel speed of 60 mm/min and rotation speed of 500 rpm is 178 MPa, which is a joint efficiency of about 79%. For effect of process parameter on tensile strength, the tensile strength increase with increasing rotation speed and decreasing travel speed.

➢ Whereas, the highest tensile strength of LAFS welds produced under conditions of travel speed of 60 mm/min, rotation speed of 400 rpm and laser power of 200 W is 193 MPa, which is a joint efficiency of about 88%.

➢ It can be inferred that the increase in tensile strength is attributed to the sufficient material flow under elevated temperature by adopting the laser preheating. Moreover, compared with FS welds, the tensile strength of LAFS welds increases at travel speed of 90 mm/min. This result shows that laser assisted friction stir welding owns wider process window than friction stir welding with improvement in welding speed.

➢ The localized decrement in hardness value at TMAZ of retreating side close to stir zone is observed due to the softening caused by reduction in dislocation density, metallurgical recovery and annealing effect during thermal cycle.

➢ The intermetallic compounds formed in conventional FS welds mainly was Fe_4Al_{13}, while the intermetallic compounds formed in LAFS welds was FeAl, Fe_2Al_5 and Fe_4Al_{13} obtained from X-ray diffraction (XRD) analysis. The layer of intermetallic compounds in laser assisted friction stir welding is approximately 5 times thicker than that of conventional friction stir welding due to relatively elevated temperature at joint interface.

68

Reference

[1]   Bang, H. S., Bang, H. S., Kim, H. S., Kim, J. H., Oh, I. H., Ro, C. S., 2010. A study on the weldability and mechanical characteristics of dissimilar materials butt joints by laser assisted friction stir welding. J. of welding and joining. 28, pp. 70-75

[2]   Bang, H. S., Bang, H. S., Jeon, G. H., Oh, I. H., Ro, C. S., 2012. Gas tungsten arc welding assisted hybrid friction stir welding of dissimilar materials Al6061-T6 aluminum alloy and STS304 stainless steel. Mater. Des. 37, 48-55

[3]   Bang, H. S., Bang, H. S., Song, H. J., Joo, S. M., 2013. Join properties of dissimilar Al6061-T6 aluminum alloy/Ti-6%Al-4%V titanium alloy by gas tungsten arc welding assisted hybrid friction stir welding. Mater. Des. 51, pp. 544-551

[4]   Kim, K. H., Bang, H. S., Ro, C. S., Bang, H. S., 2017. Influence of preheating source on mechanical properties and welding residual stress characteristics in ultra thin ferritic stainless steel hybrid friction stir welded joints. Int. J. Precis Eng Manuf-Green Technol. 4, pp. 393-400

[5]   Ramachandran, K.K., Murugan, N., Shashi Kumar, S., 2015. Friction stir welding of aluminum alloy AA5052 and HSLA steel. Weld. J. 94, 291-300

Chapter 4.

Features of Residual Stress in Laser Assisted FSW Hybrid Welded Joints

4.1 Introduction

Friction stir welding (FSW) is a solid-state joining process which joins the materials at a temperature below the melting point of the base metal. FSW process yields lower residual stresses as compared to the conventional fusion welds due to its low welding temperature than conventional fusion welding techniques. However, the strong rigid clamping arrangement could exert a much higher restraint on the deformation of the welded plates than the compliant clamp used for fixing the parts during the conventional fusion welding process. These restraints impede the contraction of material during cooling of the nugget zone (NZ) and heat affected zone (HAZ) in longitudinal as well as in transverse direction inducing transverse and longitudinal welding residual stresses [1]. In this sense, numerically analytical investigations on heat conduction and elastic-plastic analysis of friction stir welding have been performed to predict the heat and residual stress distribution [2]. Rajesh et al. studied numerical determination of residual stress in friction stir weld of Al6061-T6 using newly developed 3D-analytical model of stir zone. They reported that the predicted longitudinal residual stress distribution was reasonable agreement with the experimentally measured value [3]. Nandan et al. investigated three-dimensional heat and material flow during friction stir welding of mild steel [4].

Hybrid friction stir welding (HFSW) such as laser-assisted friction stir welding (LAFSW) and tungsten inert gas assisted friction stir welding (TAFSW) is an innovative process in joining dissimilar materials [5-7]. These processes have great potential to produce effective and defect free joints. Heat is mainly generated by the friction between the tool and workpiece during welding. The preheating source adopted in hybrid friction stir welding process can offer a better plastic flow of material. However, the joining of aluminium alloy and steel is still challenging. A difference in thermo-physical properties of the two materials can result in large welding residual stress and formation of brittle intermetallic compounds. In particular, the influence of preheating on the distribution of welding residual stress in welds is different in comparison to that of conventional friction stir welding. Bang et al. investigated residual stress in GTAW assisted hybrid friction stir butt welding of Al 6061-T6 and STS304 [8]. The authors reported lower longitudinal residual

71

stress in the STS304 side. The maximum longitudinal stress values predicted by simulation were approximately 15% of yield strength of base metal and a further increase in longitudinal residual stress around 20-35% exhibited with the release of clamping in both advancing and retreating side. Kim et al. studied the influence of preheating source on characteristics of welding residual stress in hybrid friction stir welding of ultrathin ferritic stainless steels [9]. The authors compared the induced residual stress for different welding techniques (GTAW, FSW and HFSW) and reported the order of magnitude of the stress component (σ_x) in welding direction was GTAW > HFSW > FSW. In case of stress component (σ_y) perpendicular to welding direction, the FSW and HSW processes exhibited a similar value of maximum residual stress. However, the area of residual stress distribution in HFSW was smaller than the FSW. Sundqvist et al. investigated numerical simulation of laser preheating of friction stir welding of Ti-6Al-4V to AISI 304L [10]. They explained that laser beam preheating can be substantially possible to lower acting force on the tool pin and shoulder. Their results of temperature distribution obtained from simulation showed good agreement with experiment results.

Residual stress occurs when material is subjected to a non-uniform temperature change. This stress is usually called thermal stress. The significant amounts of welding residual stress can be generated in the dissimilar joining of steel and aluminium alloy leading to critical degradation of the structural integrity and performance. However, numerically predicting welding residual stress and distortion for the joint of steel and aluminium alloy might be more complex and difficult, since it involves the interaction of thermal and mechanical phenomena. Therefore, it is necessary to investigate the temperature field first and then evaluate the welding residual stress field in the dissimilar joint of steel and aluminium alloy. The aim of present study is to estimate the temperature distribution and welding residual stress in laser-assisted friction stir welding of dissimilar Al/Fe welds through numerical simulation.

4.2 FE Model of heat source

4.2.1 Characterization of heat source

(a) Conventional Friction Stir Welding process [4, 11]

The total heat energy is generated by frictional heat and deformation at the tool shoulder/workpiece interface and tool pin/workpiece interface during conventional friction stir welding process. For three-dimensional numerical modeling on heat generation in conventional friction stir welding (CFSW), the total heat generation is simply expressed as follow:

$$Q_{\text{total}} = Q_{\text{shoulder}} + Q_{\text{pinsurface}} + Q_{\text{pinbottom}} \tag{4.1}$$

As shown in Fig. 3.1, the tangential speed (V_r) of the tool with respect to the workpiece between the tool shoulder and workpiece interface is expressed as follows:

$$V_r = (\omega r - U\sin\theta) \tag{4.2}$$

The local heat generation rate (q_1) due to friction at tool-workpiece interface is expressed as follows:

$$q_1 = \delta \times V_r \times \mu_f P_N dA \text{ (sliding velocity} \times \text{frictional force)}$$

$$= \delta \times (\omega r - U\sin\theta) \times \mu_f P dA \tag{4.3}$$
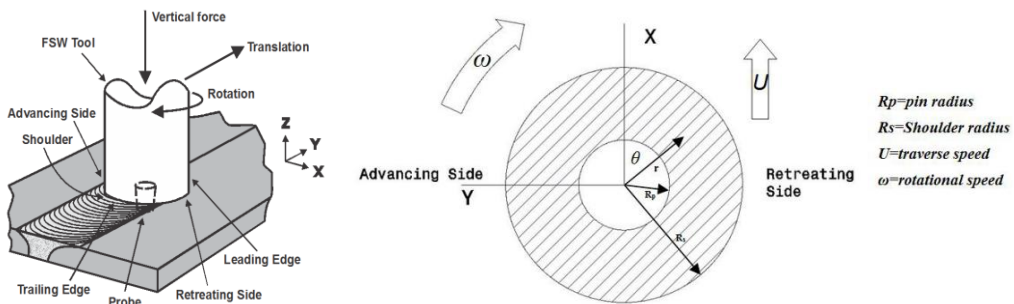
Fig. 4-1   ***Schematic of rotation and travel speed direction of tool shoulder***

73

The local heat generation rate (q_2) due to shear deformation at tool-workpiece interface is expressed as follows:

$$q_2 = \eta_m \times (1 - \delta) \times (\omega r - U\sin\theta) \times \tau_y dA \tag{4.4}$$

Due to friction and plastic deformation at the tool shoulder and workpiece interface, summing up these two components on equations of 4.3 and 4.3, the rate of heat generation per unit area along the tool shoulder and workpiece interface (Q_s) is analytically calculated as follows:

$$Q_s = \eta_h \frac{q_1 + q_2}{dA}$$

$$= \eta_h \left[\delta\mu_f P_N + \eta_m (1 - \delta)\tau_y \right](\omega r - U\sin\theta) \tag{4.5}$$

where η_h is heat partition efficiency, δ is extent of slip, μ_f is coefficient of friction, P_N is axial pressure, η_m is mechanical efficiency, τ_y is the temperature dependent shear yield stress of the deforming material, ω is the rotation speed, r is the radial distance from the tool axis, U is the welding speed and θ is the angle between radial vector and welding direction.

Assuming a steady state, one-dimensional heat flow through the interface of two metallic materials, the percentage of heat transferred to the workpiece (η_h) is estimated as follows:

$$\eta_h = \frac{\sqrt{(K \times \rho \times C_p)_{WO}}}{\sqrt{(K \times \rho \times C_p)_{TO}} + \sqrt{(K \times \rho \times C_p)_{WO}}} \tag{4.6}$$

where the subscript W_O and T_O refer to workpiece and tool material, respectively. The equation assumes an intimate contact between the tool and the workpiece and constant thermophysical properties.

When sticking condition is $\delta = 1$, no material stick to the tool and all heat is generated by friction. In contrast, when sliding condition is $\delta = 0$, all heat is generated by plastic deformation. The detailed definition of contact condition related to tool and matrix velocity is shown in Table 3.1. The terms on extent of slip (δ) and coefficient of friction (μ_f) are estimated as follow:

74

$$\delta = -0.026 + 0.5 \times \exp\left(\frac{\omega r}{1.87}\right) \tag{4.7}$$

$$\mu = 0.5 \times \exp(-\delta \omega r) \tag{4.8}$$

Table 4-1 Definition of contact condition related to tool and matrix velocity

Contact condition	Matrix velocity (m/sec)	Tool velocity (m/sec)	Shear stress (Pa)	State variable
Sticking	$v_{matrix} = v_{tool}$	$v_{tool} = \omega r$	$\tau_{friction} > \tau_{yield}$	$\delta = 1$
Sticking/sliding	$v_{matrix} < v_{tool}$	$v_{tool} = \omega r$	$\tau_{friction} \geq \tau_{yield}$	$0 < \delta < 1$
Sliding	$v_{matrix} = 0$	$v_{tool} = \omega r$	$\tau_{friction} < \tau_{yield}$	$\delta = 0$

As shown in Fig. 3-2, $R(z)$ is linearly decreased from top to bottom surface of the tool pin and can be expressed as follows:

$$R(z) = R_1 + (R_2 - R_1)\frac{z}{h} \tag{4.9}$$

Due to plastic deformation of workpiece material by tool pin, the rate of heat generation around the taper pin surface on vertical surface is applied as volumetric heat intensity (Q_{ps}) and is calculated as follows:

$$Q_{ps} = \eta_h\big[\eta_m(1-\delta)\tau_y + \delta\mu_f\sigma_y\big]\{\omega R(z) - U\sin\theta\}\left(\frac{A_i}{V_i}\right) \tag{4.10}$$
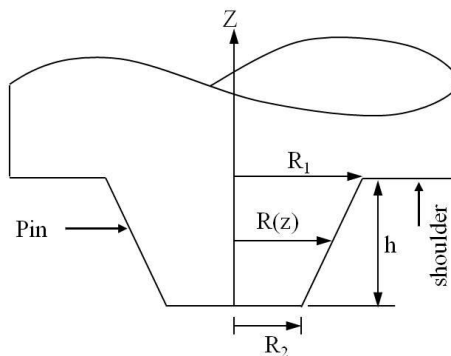
Fig. 4-2 *Schematic of FSW tool pin used in present study*

75

where η_h is the percentage of heat transferred to the workpiece. η_m is the mechanical efficiency, which is a material dependent parameter on complex function of strain, strain rate and temperature. The shear yield stress (τ_y) is assumed to be $\sigma_y/\sqrt{3}$ based on the distortion energy yield criteria. σ_y and R(z) are the temperature dependent yield strength of the deforming material and pin radius, respectively. A_i and V_i are the pin surface contact area and the volume of the presumed shear layer adjacent to the pin surface.

The rate of frictional heat generation along the pin bottom surface is also applied as volumetric heat intensity by multiplying the rate of heat generation per unit area along the tool shoulder and workpiece interface (Q_s) with the ratio of (A_i/V_i).

$$Q_{pb} = \eta_h\left[\eta_m(1-\delta)\tau_y + \delta\mu_f\sigma_y\right] \times \{\omega r - U\mathrm{Sin}\theta\} \times \left(\frac{A_i}{V_i}\right) \tag{4.11}$$

(b) Laser preheating source

In laser assisted FSW hybrid process, the heat input (Q_{lp}) from laser preheating source was considered as a surface heat flux considering Gaussian distribution.

$$Q_{lp} = \frac{d\eta P_w}{\pi r_{eff}^2}\exp\left(-d\frac{x^2+y^2}{r_{eff}^2}\right) \tag{4.12}$$

where d is the energy distribution coefficient, η and P_w referred to process efficiency and laser power, and r_{eff} represented effective radius of laser beam on top surface of workpiece. The values of d and η are considered as 1.3 and 0.5, respectively. A lumped heat transfer coefficient of $h_0(T-T_0)^{0.25}$ was considered to represent the heat loss from bottom surface. The value of h_0 is 70 W/m^2K and constant heat transfer coefficient is 20 W/m^2K.

76

4.2.2 Analysis method

(a) Heat conduction analysis

The governing equation of transient three-dimensional heat conduction analysis in joining of aluminium to steel by conventional friction stir welding is defined as follows:

$$\lambda\left(\frac{\partial^2 T}{\partial x^2} + \frac{\partial^2 T}{\partial y^2} + \frac{\partial^2 T}{\partial z^2}\right) + \dot{Q} = \rho c \frac{\partial T}{\partial t} \tag{4.13}$$

where λ is the thermal conductivity of isotropic material (W/m·K), T is the temperature (K), ρ is the density (g/m^3), $\dot{Q}$ is the internal heat generation per unit volume (W/m^3), t is the time (sec), and c is the specific heat (J/kg·K).

The boundary condition applied in the analysis is represented as follows:

$$\lambda\left(\frac{\partial T}{\partial n}\right) - q_s + h(T - T_0) + \sigma\varepsilon(T^4 - T_0^4) = 0 \tag{4.14}$$

where n represents normal direction to surface. h, σ and ε are convective heat transfer coefficient, emissivity and Stephen-Boltzmann constant, respectively. In equation (4.14), the first term represents heat loss by conduction from the surface; the second term represents heat flux applied onto the surface, and third and fourth terms represent heat loss from the surface to atmosphere by convection and radiation, respectively. The radiation heat loss from the workpiece surface is neglected considering that the peak temperature during FSW remains below the melting temperature of material [12].

A lumped heat transfer coefficient is expressed as follows:

$$h = h_0(T - T_0)^{0.25} \tag{4.15}$$

where $h_0 = 70 \, \text{W/m}^2\text{K}$ is used for the bottom and side surface to account for the heat loss and a constant heat transfer coefficient of $20 \, \text{W/m}^2\text{K}$ is applied for rest of the surfaces.

77

(b) Thermal elastic-plastic analysis

The temperature history calculated in the temperature field model was applied as a thermal load for elastic-plastic analysis of residual stress field. The elastic strain-stress relationship in the elastic region is considered by isotropic Hooke's law. The plastic behavior in plastic region is considered by Von Misses yield criterion and linear isotropic hardening rule. In the thermal elastic-plastic analysis, the total strain rate ($\dot{\varepsilon}_{ij}^{total}$) includes elastic strain rate ($\dot{\varepsilon}_{ij}^{e}$), plastic strain rate ($\dot{\varepsilon}_{ij}^{p}$) and thermal strain rate ($\dot{\varepsilon}_{ij}^{th}$) as follows:

$$\dot{\varepsilon}_{ij}^{total} = \dot{\varepsilon}_{ij}^{e} + \dot{\varepsilon}_{ij}^{p} + \dot{\varepsilon}_{ij}^{th} \tag{4.16}$$

The thermal strain rate, which is calculated by the amount of change in temperature multiplied by the thermal expansion coefficient, can ($\dot{\varepsilon}_{ij}^{th}$) be expressed as follows:

$$\dot{\varepsilon}_{ij}^{th} = \delta_{ij}\alpha\dot{T} \tag{4.17}$$

where δ_{ij} is Kronecker delta function; α is the thermal expansion coefficient and $\dot{T}$ is the rate of temperature change.

By combining the strain rate components on elastic, plastic and thermal, the total strain rate can be expressed as follows:

$$\dot{\varepsilon}_{ij}^{total} = \frac{1+\nu}{E}\dot{\sigma}_{ij} - \delta_{ij}\frac{\nu}{E}\dot{\sigma}_{kk} + \lambda s_{ij} + \delta_{ij}\alpha\dot{T} \tag{4.18}$$

where E is Young's modulus; ν is Poisson's ratio λ is the plastic flow factor, s_{ij} is the components of deviatoric stresses and α is the thermal expansion coefficient. $\lambda = 0$ is for elastic deformation (or $\sigma_e < \sigma_s$) and $\lambda > 0$ is for plastic deformation (or $\sigma_e \geq \sigma_s$).

$$s_{ij} = \sigma_{ij} - \delta_{ij}\frac{\sigma_{kk}}{3} \tag{4.19}$$

$$\sigma_e = \sqrt{\frac{3}{2}S_{ij}S_{ij}} \tag{4.20}$$

4.3 Features of residual stress and plastic stain

4.3.1 Model and temperature-dependent material property

(a) Finite Element Model

The temperature field and the weld-induced residual stress field and plastic strain field of dissimilar welded joints are performed by numerical analysis based on FEM modeling using ANSYS 18.0 commercial software. The ANSYS parametric design language (APDL) code is developed for transient thermal analysis and thermo-mechanical analysis. The finite element (FE) model on large size with dimensions of 600 mm (L) $\times$ 500 mm (B) is shown in Fig. 4.3. The dimension of small FEM model, which is equivalent to dimensions of experiment of dissimilar materials, is 200 mm (L) $\times$ 200 mm (B). Workpiece thicknesses of aluminium alloy and steel are 2.5 mm and 1.4 mm, respectively. In this FE model, the number of brick element and node are 204,497 and 246,735, respectively. The model is meshed using a brick element called SOLID70, which is three dimensional elements and can be used for a three dimensional steady-state or transient analysis. The element is defined by eight nodes with temperature as single degree of freedom at each node. Solid185 is correspondingly used for thermo-mechanical analysis. The result of thermal analysis is given as the input data for thermo-mechanical analysis.
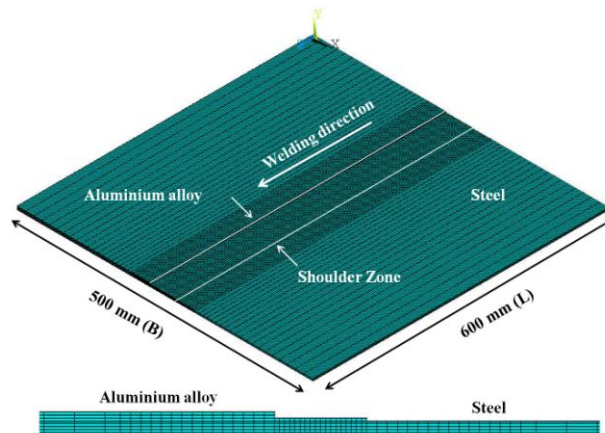
Fig. 4-3   Finite element model of dissimilar welds

79

(b) Temperature-dependent material properties

The temperature-dependent thermal physical properties and mechanical properties of aluminium alloy and steel applied in the present analysis are shown in Table. 4-2 and Table 4-3. Because the temperature-dependent thermal physical properties and mechanical properties on dissimilar materials are significantly different, it can make a great difference in deformation between aluminium alloy and steel. The temperature-dependent thermal physical properties such as density, solidus temperature (T_S), liquidus temperature (T_L), specific heat and thermal conductivity are used for transient thermal analysis and temperature-dependent mechanical properties including Young's modulus, Poisson's ratio, yield strength and thermal expansion coefficient are used for thermo-mechanical analysis.

Table 4-2   Temperature-dependent thermal physical properties of aluminium alloy and steel

Material	Property	Value
Aluminium AA5052	Density, kg/m^3	2,696
	Solidus temperature, K	880
	Liquidus temperature, K	925
	Specific heat, J/kg K	$929.0-0.627T+1.5\times10^{-3}T^2+4\times10^{-8}T^3$
	Thermal conductivity, W/m K	$25.2+0.398T+7\times10^{-6}T^2-3\times10^{-7}T^3$
Steel DP590	Density, kg/m^3	8,000
	Solidus temperature, K	1,673
	Liquidus temperature, K	1,728
	Specific heat, J/kg K	$448.11+3.7\times10^{-2}T+1.61\times10^{-4}T^2-6.86\times10^{-8}T^3$
	Thermal conductivity, W/m K	$3.79+3.85\times10^{-2}T-4.18\times10^{-6}T^2-3.03\times10^{-9}T^3$

Table 4-3   Temperature-dependent thermal mechanical properties of aluminium alloy and steel

Material	Property	Value
Aluminium (AA5052)	Young's modulus, GPa	$68791.65+91.32T-0.29T^2+1.61\times10^{-4}T^3$
	Poisson's ratio	$0.33+1.65\times10^{-4}T-1.29\times10^{-6}T^2+2.61\times10^{-9}T^3-1.4\times10^{-12}T^4$
	Yield strength, MPa	$112.64+2.73T-0.0091T^2+7.14\times10^{-6}T^3$
	Thermal expansion coefficient	$1.45\times10^{-6}+1.34\times10^{-7}T-2.21\times10^{-10}T^2+1.17\times10^{-13}T^3$
Steel (DP590)	Young's modulus	$218900.06-63.61T-0.04T^2+1.6\times10^{-5}T^3$
	Poisson's ratio	$0.28+4.35\times10^{-5}T+5.42\times10^{-8}T^2-2.34\times10^{-11}T^3$
	Yield strength, MPa	$628.01-1.76T+0.0021T^2-8.34\times10^{-7}T^3$
	Thermal expansion coefficient	$8.62\times10^{-6}+2.97\times10^{-8}T-2.41\times10^{-11}T^2+6.17\times10^{-15}T^3$

4.3.2 Heat conduction analysis

Fig. 4-4 shows the temperature field calculated in conventional FS welds and laser-assisted FS welds of aluminium and steel. The aluminium alloy is on the retreating side, and the advanced high-strength steel plate is on advancing side. It can be seen from Fig. 4-4 that the temperature distribution of aluminium alloy and steel was asymmetric due to the difference in their thermophysical properties. The temperature gradient in aluminium alloy was larger than that of steel because the thermal conductivity of aluminium alloy is much higher than that of steel. Therefore, the temperature region in aluminium alloy was wider than steel during welding.

(a) FS welds   (b) LAFS welds
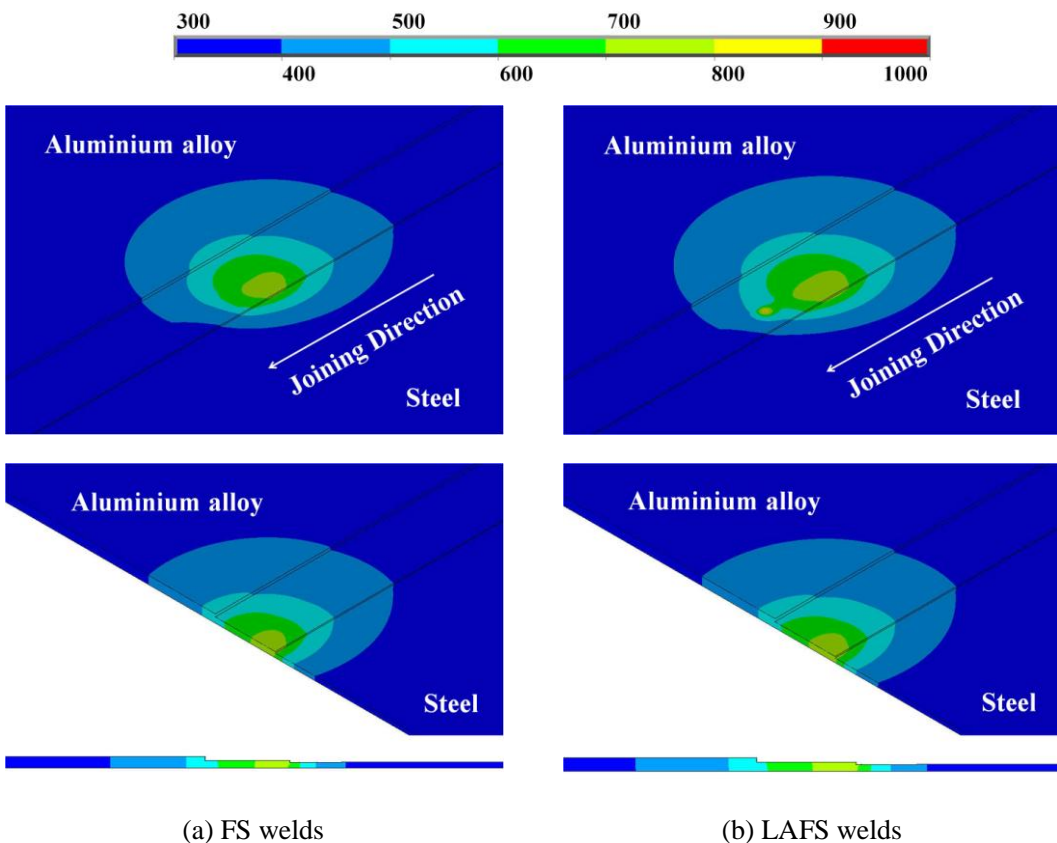
Fig. 4-4   Welding temperature field; (a) FS welds and (b) LAFS welds

82
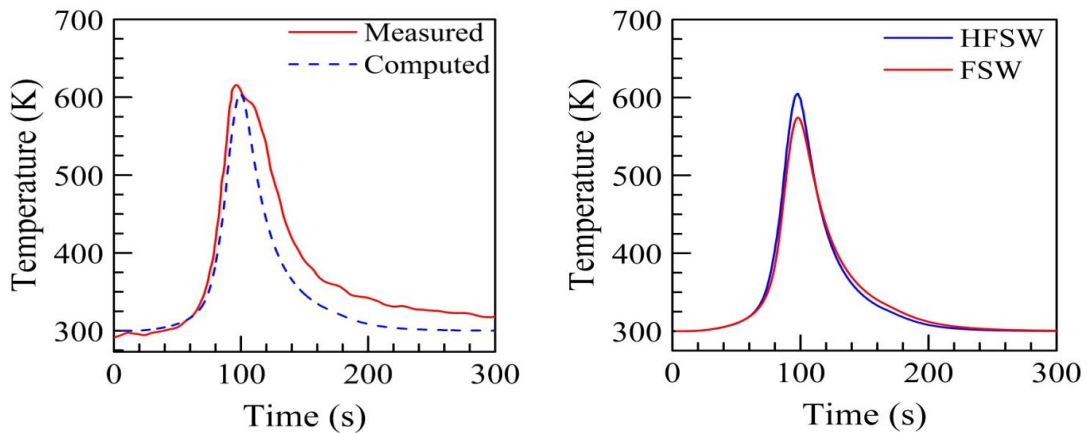
(a) Comparison of temperature history
obtained from experiment and analysis

(b) Comparison of temperature history in FS
welds and LAFS welds

**Fig. 4-5   Comparison of temperature history; (a) Comparison of temperature history
obtained from experiment and analysis and (b) Comparison of temperature
history in FS welds and LAFS welds**

On the other hand, the temperature field at joint interface between aluminium and steel was also
asymmetric due to low thermal conductivity of steel leading to higher local temperature in the steel
near interface. In comparison with temperature field distribution of FS welds, the maximum peak
temperature of LAFS welds occurred at laser preheating zone in steel side. As shown in Fig. 4-4(b),
the higher temperature region in LAFS welds was longer than that of FS welds due to preheating
effect by laser beam, which resulted in the enhanced softening effect on the steel during welding.
This softening effect of the steel can be possible to be contributed to lower axial force during
welding and relatively reduce wear of tool.

In order to verify the validation of finite element model, the result obtained from thermal
analysis was compared with experimental result. Fig. 4-5(a) shows the comparison of calculated
temperature history and corresponding experimentally measured temperature history. Note that
temperature unit used in present thermal analysis is expressed as absolute temperature (K). It can
be seen from Fig. 4-5(a) that at a thermocouple monitoring location of 12 mm of steel side away

83

from the joint interface, the peak temperature of the measured location was 616 K and calculated peak temperature was 604 K. The result obtained from simulation indicates good agreement with experimental result. Fig. 4-5(b) shows the comparison of calculated temperature history in steel side. The result calculated in simulation shows that the peak temperature of LAFS welds was approximately 40 K higher than that of FS welds due to laser preheating on steel surface. In general, bimodal thermal characteristic could be observed in thermal cycle when preheating source is employed in hybrid friction stir welding process (e.g. LAFSW and TAFSW). Bimodal thermal characteristic means that one of the two peak temperature between preheating source and primary heat source is high or low. However, no distinct bimodal thermal characteristic by laser preheating was observed in LAFS welds obtained from results of experiment and analysis. It can be inferred that the distance between laser preheating source and rotating tool was close, indicating that the heat input of laser preheating was almost equivalent to heat generation of FSW.

(a) FS welds　　　　　　　　　(b) LAFS welds
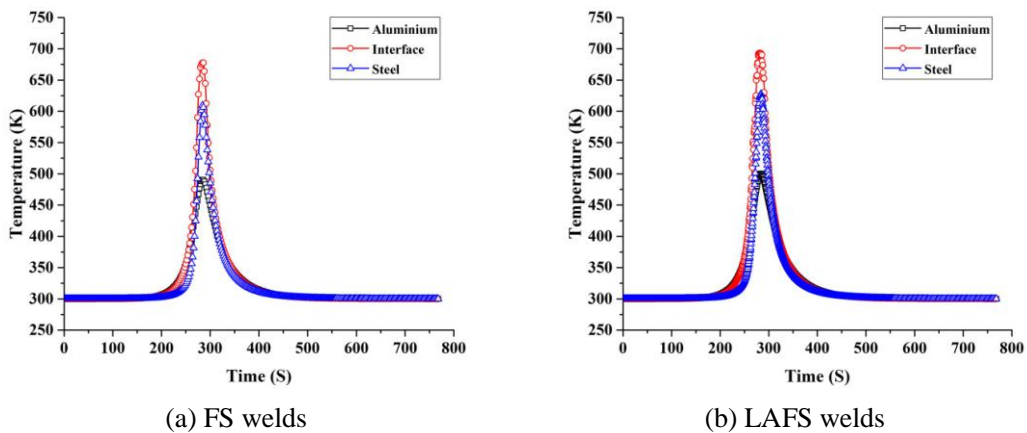
Fig. 4-6　　Temperature history obtained from thermal analysis at three different positions; (a) FS welds and (b) LAFS welds

Fig. 4-6 shows the temperature history of FS welds and LAFS welds obtained from thermal analysis at three different positions. The thermal cycles calculated at all positions indicate that the peak temperature of LAFS welds was higher than that of FS welds. The peak temperature at

84

interface of LAFS welds was about 715 K while the peak temperature of interface in FS welds was about 675 K. This elevated temperature is attributed to laser preheating during welding and will have inevitable effect on formation and growth of intermetallic compounds at joint interface between aluminium and steel. In addition, the difference in the temperature compared between conventional friction stir welding and laser assisted friction stir welding could lead to the regional variations of welding residual stress distribution.

4.3.3 Thermal elastic-plastic stress analysis

(a) Residual stress field analysis

The temperature history calculated from temperature field model was employed as thermal load in elastic-plastic stress analysis to estimate the welding residual stress field and plastic strain field. Fig. 4-7 shows the comparison of welding residual stress distribution field of FS welds and LAFS welds obtained from thermal elastic-plastic stress analysis. It can be seen from Fig. 4-7(a) that the peak value of transverse residual stress in LAFS welds was slightly higher than that of FS welds and the distribution field of residual stress in steel side away from joint interface was significantly different. In case of FS welds, the transverse residual stress distribution existed at outside of weld bead (weld bead means shoulder zone) in steel side, while the transverse residual stress distribution of LAFS welds existed in the weld bead at steel side. The peak values of transverse residual stress in FS welds and LAFS welds was 312 MPa and 318 MPa, respectively. These peak values of not only FS welds but also LAFS welds were approximately 32% and 31% smaller than the yield strength of steel base metal, which is 459 MPa. The distribution field of longitudinal residual stress component is shown in Fig. 4-7(c). The distribution of longitudinal residual stress was similar to result of the distribution field of transverse residual stress. The results showed that the magnitude of the longitudinal stress component in LAFS welds was relatively higher than that of FS welds. However, the peak value of residual stress in FS welds was slightly higher than in LAFS welds. The peak values of longitudinal residual stress in FS welds and LAFS welds was 321 MPa and 314 MPa, respectively. The peak values of longitudinal residual stress in FS welds and LAFS welds were not more than the yield strength of steel base metal. It can be clearly found that the longitudinal residual stress distribution was concentrated at the weld bead of dissimilar joints obtained by conventional friction stir welding and laser assisted friction stir welding processes and then these residual stress distributions gradually decreased further away from weld bead. Fig. 4-7(d) illustrates the comparison of corresponding von Mises equivalent stress distribution of FS welds and LAFS welds obtained by thermal elastic-plastic stress analysis in order to determine the final residual stress state after cooling phase. It can be found similarly to

longitudinal residual stress distribution that a higher residual stress concentration occurred at steel side in the weld bead. The von Mises equivalent residual stress in steel side was relatively higher than in aluminium alloy side. The peak value of equivalent residual stress predicted in FS welds and LAFS welds was 286 MPa and 319 MPa, which occurred at steel side in the weld bead. Theses peak values did not also exceed the yield strength of steel base metal. It can be seen from the comparative results of Fig. 4-7, the distribution of corresponding von Mises equivalent stress of FS welds and LAFS welds as well as normal stress components was significantly asymmetric due to non-uniform temperature characteristic in the aluminium/steel joints, especially resulting from difference in thermal physical properties (e.g. about doubled in thermal expansion coefficient between aluminium and steel).
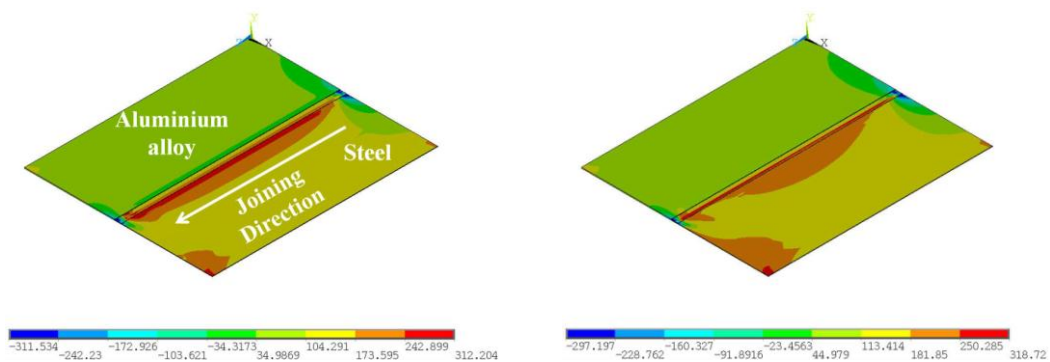
(a) Distribution field of transverse residual stress component (SX)
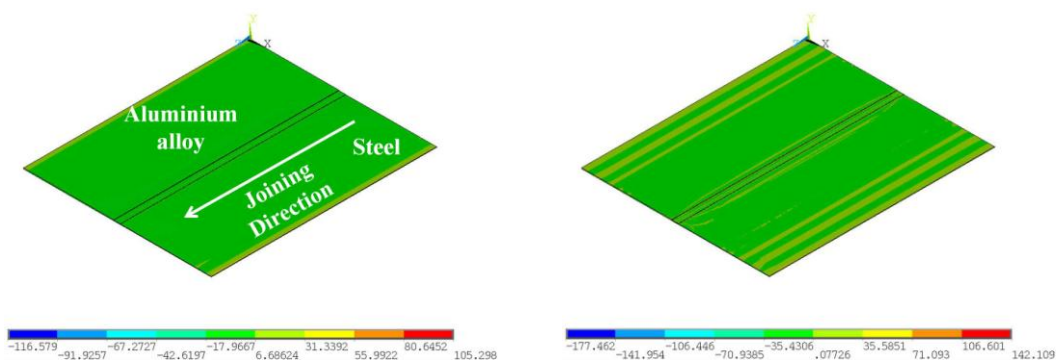
(b) Distribution field of normal residual stress along the thickness component (SY)

87
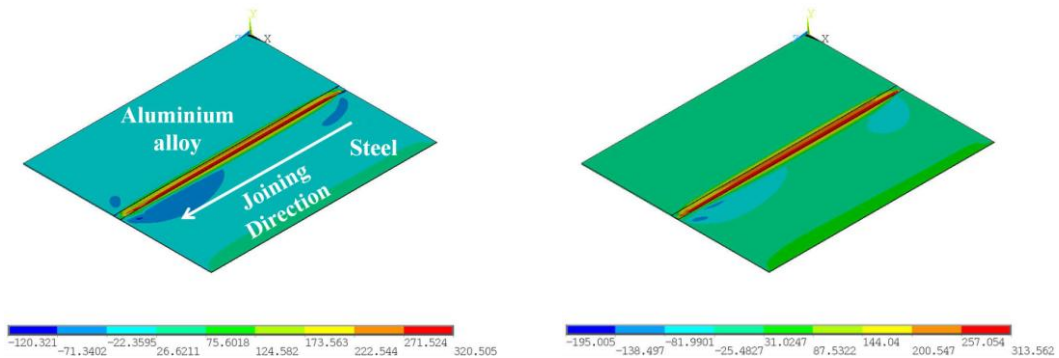
(c) Distribution field of longitudinal residual stress component (SZ)

(d) Distribution field of von Mises equivalent residual stress component (SEQV)

Fig. 4-7   Comparison of distribution field in residual stress components after cooling phase; (a) SX, (b) SY, (c) SZ and (d) SEQV

Fig. 4-8 shows the comparative distribution curves of longitudinal residual stress components obtained by thermal elastic-plastic stress analysis at intermediate transverse section (z=300 mm) after cooling phase. The left side and right side in Fig. 4-8 indicate FS welds and LAFS welds, respectively. It can be seen from Fig. 4-8(a) that similar to FS welds, the transverse residual stress distribution in LAFS welds exhibited asymmetrical curve and the tensile transverse residual stress mainly appeared. The peak values of transverse residual stress in FS welds and LAFS welds occurred at steel side and were about 223 MPa and 254 MPa, respectively. Meanwhile, in case of aluminium side, the peak values of transverse residual stress in FS welds was slightly higher than

88

that of LAFS welds and were about 150 MPa and 137 MPa, respectively. It can be clearly found that these peak values were smaller than the yield strength of its base metal. Fig. 4-8(b) shows that the distribution of normal residual stress along the thickness. This comparative result indicates that the variation of stress distribution was relatively less than the distributions of transverse and longitudinal residual stress. The comparison of longitudinal residual stress distribution predicted is shown in Fig. 4-8(c). It can be seen from Fig. 4-8 that among the residual stress components, the longitudinal residual stress indicates the highest value compared with other residual stress components.
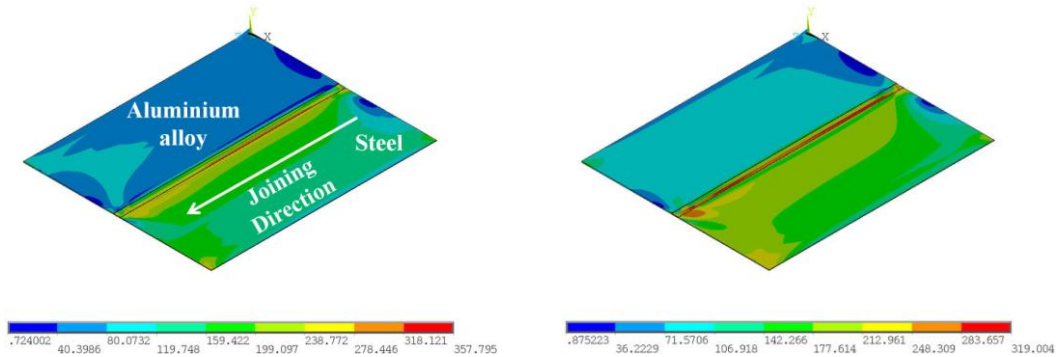

(a) Distribution of transverse residual stress component (SX)
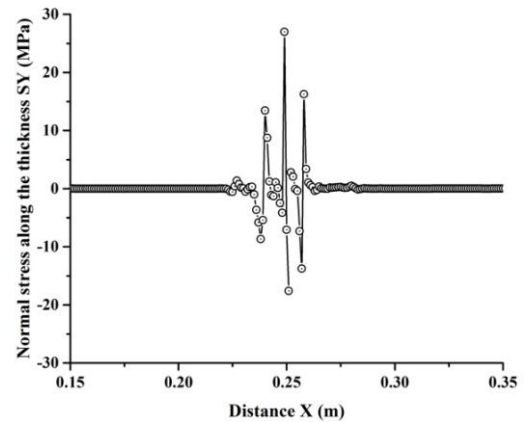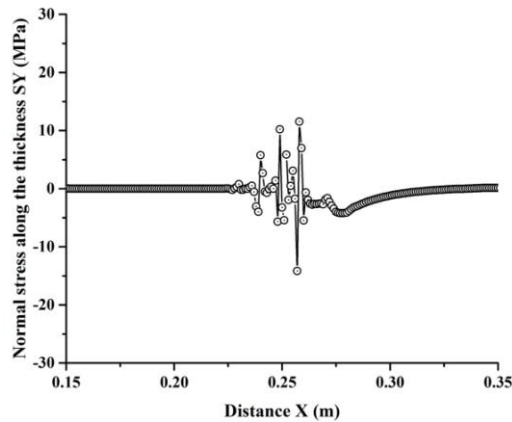
(b) Distribution of normal residual stress along the thickness component (SY)

89

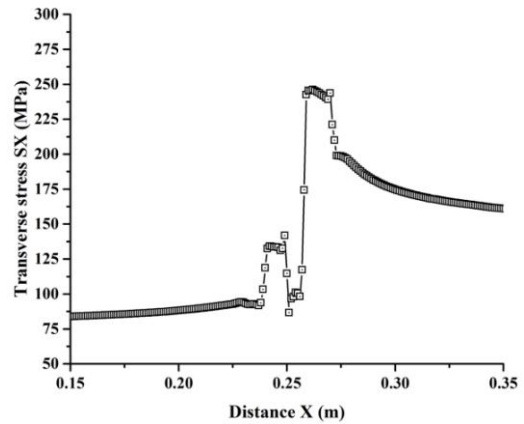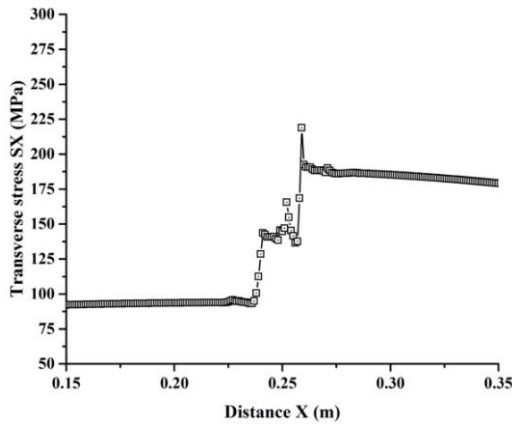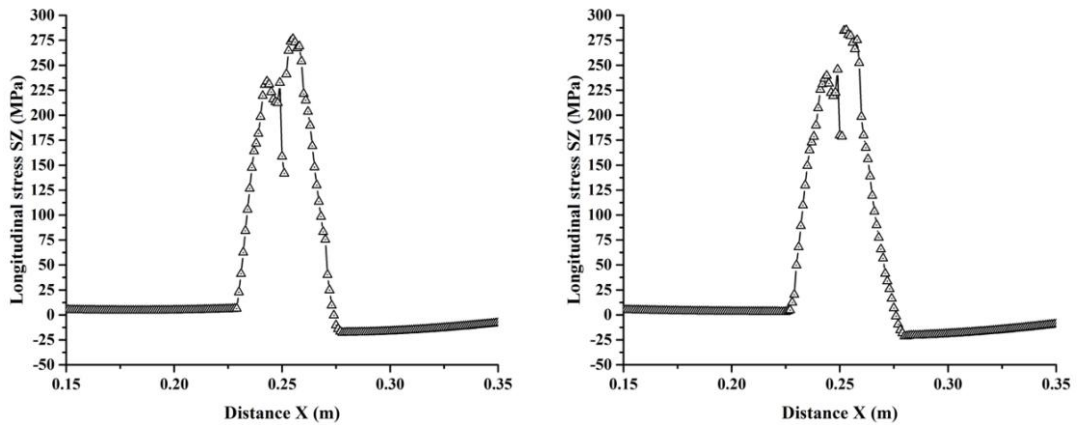(c) Distribution of longitudinal residual stress component (SZ)
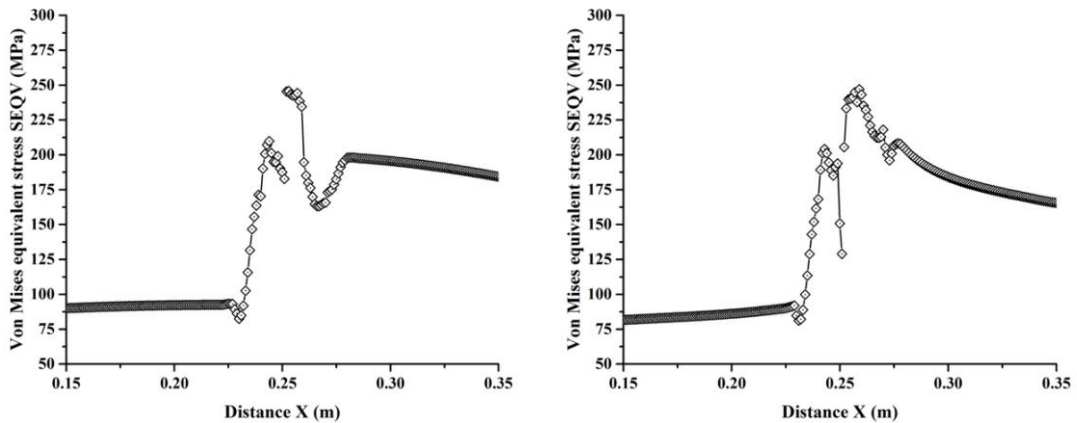
(d) Distribution of von Mises equivalent residual stress component (SEQV)

Fig. 4-8   Distribution curve of longitudinal residual stress components at intermediate section (z=300 mm) after cooling phase; (a) SX, (b) SY, (c) SZ and (d) SEQV

The peak value of longitudinal residual stress predicted in FS welds and LAFS welds was about 235 MPa and 245 MPa in aluminium side, respectively. These peak values were exceedingly larger than the yield strength of base metal, which is 188 MPa indicating. However, the peak values of longitudinal residual stress predicted in steel side did not exceed the yield strength of base metal. In comparison of residual stress components in FS welds and LAFS welds, the magnitude of peak

90

welding residual stress is in following order: longitudinal residual stress (SZ) > transverse residual stress component (SX) > normal residual stress along the thickness (SY). The distribution of von Mises equivalent residual stress predicted in FS welds and LAFS welds are shown in Fig. 4-8(d). In the residual stress distribution of aluminium side, the von Mises equivalent residual stress significantly decreased to base metal at edge of shoulder zone, where the highest value of tensile stress occurred. In the residual stress distribution of steel side, the equivalent residual stress showed similar trend like stress distribution in aluminium side. The peak values of corresponding equivalent residual stress in FS welds and LAFS welds were 212 MPa and 209 MPa in aluminium side, which is larger in FS welds, respectively. Meanwhile, the peak values of corresponding equivalent residual stress in FS welds and LAFS welds were 248 MPa and 254 MPa in steel side, which is larger in LAFS welds, respectively. Therefore, the comparative result predicted from thermal elastic-plastic stress analysis indicates that a higher stress concentration occurred at weld zone and surrounding shoulder edge. It can be clearly found the peak values of equivalent stress in aluminium side were in excess of the yield strength of base metal, which is 11~13% larger indicating that the welding induced plastic deformation is retained surrounding shoulder edge.

91

(b) Plastic strain field analysis

Fig. 4-9 shows the comparative distribution curves of longitudinal plastic strain components obtained by thermal elastic-plastic stress analysis at intermediate transverse section (z=300 mm) after cooling phase. The left side and right side in Fig. 4-9 indicate FS welds and LAFS welds, respectively. The transient temperature produced in FS welds and LAFS welds causes the variations of the physical parameters during welding. It can be seen from Fig. 4-9 that the longitudinal plastic strain distribution corresponded to trend of the temperature distribution.


(a) Distribution of transverse plastic strain component (XX)
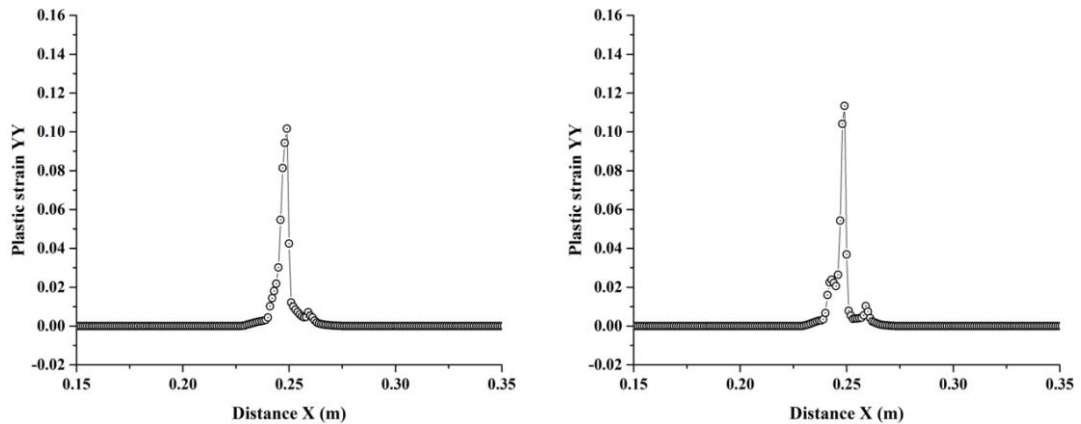
(b) Distribution of normal plastic strain along the thickness component (XX)

92
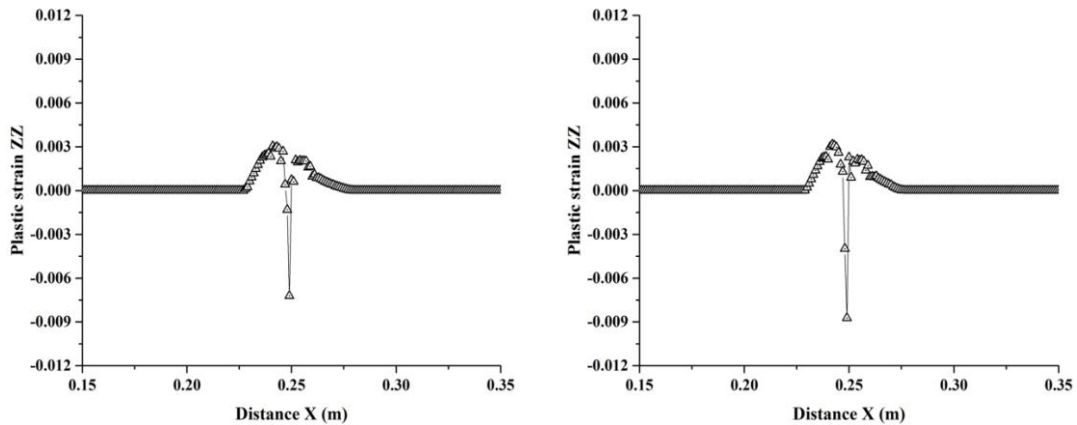
(c) Distribution of longitudinal plastic strain component (ZZ)
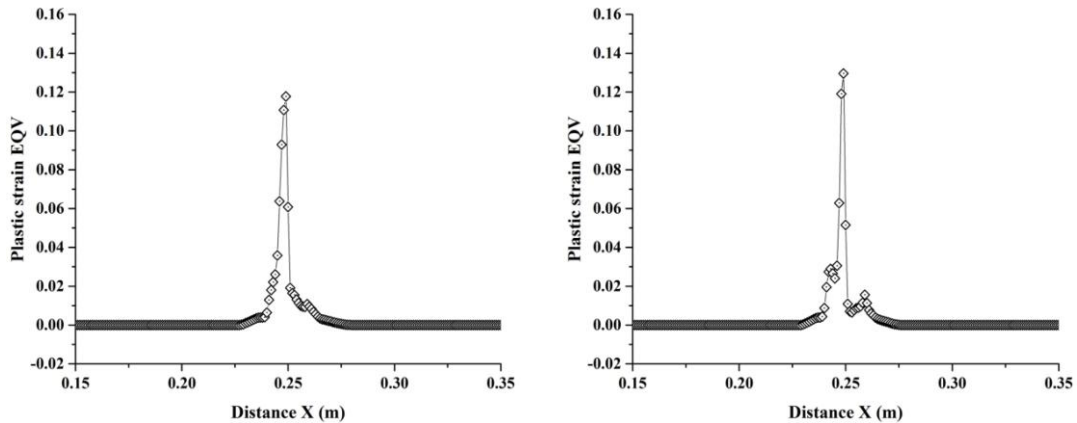
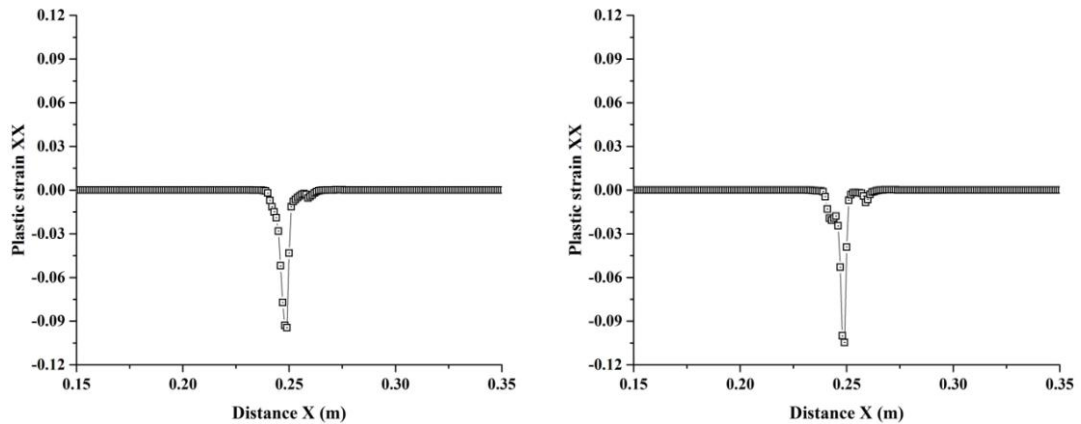(d) Distribution of equivalent plastic stain component (EQV)

Fig. 4-9   Distribution curve of longitudinal plastic strain components at intermediate section (z=300 mm) after cooling phase: (a) XX, (b) YY, (c) ZZ and (d) EQV

The high compressive transverse plastic strain relatively occurred in LAFS welds compared with FS welds, as shown in Fig. 4-9(a). Meanwhile, in Fig. 4-9(b) normal plastic strain along the thickness showed higher tensile value, especially in LAFS welds. The peak plastic strain was predicted at joint interface and then decrease with distance from the joint interface. In the laser preheating zone of LAFS welds at steel side, the plastic strain increases slightly due to the increase

93

of temperature. The equivalent plastic strain in LAFS welds was higher than in FS welds due to increase in heat input. The peak equivalent plastic strain in FS welds and LAFS welds were 0.12 and 0.135, respectively. As the plastic region extends further, the value of residual stress component becomes large.

94

4.4 Conclusions

In present study, the welding temperature field and the residual stress field in dissimilar joint of aluminium alloy and advanced high-strength steel has been performed by numerical simulation. The results can be summarized as follow:

> ➢ The temperature gradient in steel plate was larger than that in aluminium alloy because the thermal conductivitiy of aluminium alloy was much higher than that of steel. Therefore, the high temperature region in aluminium alloy was wider than in steel. The result obtained from simulation indicates good agreement with result of experiment and this model is proper to simulate this temperature field.

> ➢ In comparison with temperature field distribution of FS welds, the maximum peak temperature of LAFS welds occurred at laser preheating zone in steel side. The peak temperature at interface of LAFS welds was about 715 K while the peak temperature of interface in FS welds was about 675 K. This elevated temperature is attributed to laser preheating during welding and will have inevitable effect on formation and growth of intermetallic compounds at joint interface between aluminium and steel.

> ➢ In comparison of residual stress components in FS welds and LAFS welds, the magnitude of peak welding residual stress is in following order: longitudinal residual stress (SZ) > transverse residual stress component (SX) > normal residual stress along the thickness (SY).

> ➢ The comparative result predicted from thermal elastic-plastic stress analysis indicates that a higher stress concentration occurred at weld zone and surrounding shoulder edge. It can be clearly found the peak values of von Mises equivalent longitudinal stress in aluminium side were in excess of the yield strength of base metal, which is 11~13% larger indicating that the welding induced plastic deformation is retained surrounding shoulder edge.

Reference

[1]   Donne, D. C., Lima, E., Wegener, J., Pyzalla, A., Buslaps, E., Investigation on residual stresses in friction stir welds. 3nd International Symposium on Friction Stir Welding

[2]   Nandan, R., Debroy, D., Bhadeshia, H. K. D. H., 2008. Recent advances in friction-stir welding − process, weldment structure and properties. Prog. Mater. Sci. 53, 980-1023

[3]   Rajesh, S. R., Bang, H. S., Chang, W. S., Kim, H. J., Bang, H. S., Oh, C. I., Chu, J. S., 2007. Numerical determination of residual stress in friction stir weld using 3D-analytical model of stir zone. Acta Mater. 55, 883-895

[4]   Nandan, R., Roy, G. G., Lienert, T. J., Debroy, T., 2007. Three-dimensional heat and material flow during friction stir welding of mild steel. Prog. Mater. Sci. 53, 980-1023

[5]   Bang, H. S., Bang, H. S., Jeon, G. H., Oh, I. H., Ro, C. S., 2012. Gas tungsten arc welding assisted hybrid friction stir welding of dissimilar materials Al6061-T6 aluminium alloy and STS304 stainless steel. Mater. Des. 37, pp. 48-55

[6]   Bang, H. S., Bang, H. S., Song, H. J., Joo, S. M., 2013. Join properties of dissimilar Al6061-T6 aluminum alloy/Ti-6%Al-4%V titanium alloy by gas tungsten arc welding assisted hybrid friction stir welding. Mater. Des. 51, pp. 544-551

[7]   Bang, H. S., Bang, H. S., Kim, H. S., Kim, J. H., Oh, I. H., Ro, C. S., 2010. A study on the weldability and mechanical characteristics of dissimilar materials butt joints by laser assisted friction stir welding. J. of welding and joining. 28, pp. 70-75

[8]   Bang, H. S., Ro, C. S., Bang, H. S., Bijoy, M. S., 2012. Analysis of residual stress on dissimilar butt joint by TIG assisted hybrid friction stir welding. J. of welding and joining. 28, pp. 70-75

[9]   Kim, K. H., Bang, H. S., Ro, C. S., Bang, H. S., 2017. Influence of preheating source on mechanical properties and welding residual stress characteristics in ultra thin ferritic stainless steel hybrid friction stir welded joints. Int. J. Precis Eng Manuf-Green Technol. 4, pp. 393-400

[10]   Sundqvist, J., Kim, K. H., Bang, H. S., Bang, H. S., Kaplan A. F. H., 2018. Numerical simulation of laser preheating of friction stir welding of dissimilar metals. Sci. Technol. Weld. Join. 23, 351-356

96

[11]   Hong, S. M., Bang, H. S., Kim, K. H., Bang, H. S., 2018. Prediction of IMC thickness in laser assisted hybrid friction stir welded joint of dissimilar materials (Al5052-DP590) by numerical analysis. Abstract of the 2018 Spring Annual Meeting of Korean Welding and Joining Society, pp. 62

[12]   Das, H., Jana, S. S., Pal, T. K., De, A., 2014. Numerical and experimental investigation on friction stir lap welding of aluminium to steel. Sci. Technol. Weld. Join. 19, 69-75

Chapter IV.

Summary

5.1 Summary

In present study, dissimilar joining of aluminium alloy (AA5052-H32) to advanced high-strength steel (DP590) has been successfully achieved by laser assisted friction stir welding (LAFSW). The joint performance and quality have been investigated through critical analysis on correlation between the mechanical properties and microstructures of dissimilar joint in relation to the process parameters. The influence of laser preheating source on mechanical properties and microstructures including formation of intermetallic compounds (IMC), fracture path and welding defect has been compared with that of result obtained by friction stir welding. Moreover, the numerical analysis for welding residual stress characteristics in laser assisted friction stir welding has been investigated based on thermal elastic-plastic analysis. Some important findings are achieved by and experimental investigation and numerical simulation shown below:

(**Chapter 1**) The general background including main issue in the dissimilar metal joining, research objectives and construction of thesis are described in more detail.

(**Chapter 2**) Laser assisted friction stir welding that combine the portable diode laser adopting charge-coupled device camera and friction stir welding system for joining of dissimilar materials is economically developed.

- Laser assisted friction stir welding in joining of dissimilar materials is optimized by varying the primary process parameters (e.g. travel speed, rotation speed, laser power).

- The effect of laser preheating can contribute to both greater amount of conduction heat and plastic deformation heat and promote the penetration of aluminium stirred into steel side. Therefore, the material flow is significantly enhanced by laser preheating.

(**Chapter 3**) The influence of laser preheating source on mechanical and metallurgical characteristics is minutely evaluated in dissimilar joints.

- The ultimate tensile strength of FS welds and LAFS welds are 178 MPa (79%) and 193 MPa (88%), respectively. Joint properties of laser assisted friction stir welding produced

in optimum condition is significantly 9 percent higher than that of conventional friction stir welding. Laser assisted friction stir welding owns wider process window than friction stir welding with improvement in welding speed.

- The intermetallic compounds formed in laser assisted friction stir welding is approximately 5 times thicker than that of conventional friction stir welding due to relatively elevated temperature at joint interface.

- Despite growth of intermetallic compounds by laser preheating, TMAZ failure mode in LAFS welds is the most acceptable indicating that the highest tensile strength with suitable elongation is obtained. It can be therefore inferred that this intermetallic compounds scattered in aluminium matrix can take into account as reinforcement in dissimilar welds and then is contributed to enhancement in tensile strength.

(Chapter 4) Numerical and experimental investigation of thermally induced residual stress in laser assisted friction stir welding is performed to predict the welding residual stress distribution in dissimilar joint.

- Three-dimensional thermal model is developed to predict the temperature distribution field in dissimilar joints. The result calculated from analysis indicates a good agreement with result of experiment. This FEModel is proper to simulate the temperature field in other dissimilar joints.

- Three-dimensional thermal elastic-plastic model is developed. It can be clearly found that the peak value of equivalent longitudinal stress in aluminium alloy were in excess of the yield strength of base metal, which is 11~13% larger than conventional friction stir welding. This indicates that the welding induced plastic deformation is retained surrounding shoulder edge at aluminium alloy side.

100

5.2 Scope of future work

A reliable dissimilar metals joining is still interesting since it enables suitable combination of different materials with different thickness, such as aluminium alloy (e.g. AA 6XXX series) and steel (e.g. DP780 and DP980 etc.). Some possible directions for future research are suggested as following:

- **(Comparison of process efficiency)** Investigate the comparison of process efficiency between TAFSW and LAFSW on joining of Aluminium alloy and steel

- **(Galvanic corrosion behavior)** Investigate the galvanic corrosion behavior of dissimilar Al/Fe welds by adopting protective layer, which uses adhesive bonding.

- **(Prediction on intermetallic compounds)** Investigate the prediction on intermetallic compounds coupled to thermal model developed in present study

5.3 Appendix-Research Achievements

Awards and Honors (3)
1	**(Institute)** The Korean Welding and Joining Society **(Tile)** Best Presentation Award – No.64
2	**(Institute)** The Korean Welding and Joining Society **(Tile)** Best Poster Award – No.114
3	**(Institute)** The Royal Institute of Naval Architects (RINA) and Lloyd's Resister (LR) **(Tile)** RINA-LR Asia Student Award for 2013

Domestic Proceeding Papers (19)
1	"Numerical Analysis for Thermal Characteristics Comparison of Al5052-H32 TWB Friction Stir Welded Joints by Varying Workpiece Tilting Angle", Seung-Ji Yoo, <u>Kyoung-Hak Kim</u>, Chan-Seung Ro, Han-Sur Bang, Hee-Seon Bang, 2018 Autumn Conference of the Korean Welding and Joining Society, P 238
2	"Weldability of Al6061-T6 to STS304L Joint in AC Pulse MIG Brazing by Wire Position", Jae-Yong Bae, Han-Sur Bang, <u>Kyoung-Hak Kim</u>, Hee-Seon Bang, 2018 Autumn Conference of the Korean Welding and Joining Society, P 239
3	"Prediction of IMC Thickness in Laser Assisted Hybrid Friction Stir Welded Joint of Dissimilar Materials (Al5052-DP590) by Numerical analysis", Sung-Min Hong, Han-Sur Bang, <u>Kyoung-Hak Kim</u>, Hee-Seon Bang, Abstracts of the 2018 Spring Annual Meeting of Korean Welding and Joining Society, P 62
4	"Influence of Preheating on Weldability in Hybrid Friction Stir Welded joints of Dissimilar Materials (Al-steel)", <u>Kyoung-Hak Kim</u>, Han-Sur Bang, Hee-Seon Bang, Abstracts of the 2017 Autumn Annual Meeting of Korean Welding and Joining Society, Vol. 66, P 238
5	"Evaluation of Weldability Dissimilar Materials Al/CFRP using Friction Stir Welding upon Pin Existence", Se-Young Lee, Ju-Heon Park, <u>Kyoung-Hak Kim</u>, Han-Sur Bang and Hee-Seon Bang, Abstracts of the 2017 Autumn Annual Meeting of Korean Welding and Joining Society, Vol. 66, P 230
6	"The Weldability Evaluation of Al6061-T6 with parameters on Friction Stir Corner Welding", Yeong-Bin Son, <u>Kyoung-Hak Kim</u>, Han-Sur Bang, Hee-Seon Bang, Abstracts of the 2017 Autumn Annual Meeting of Korean Welding and Joining Society, Vol. 66, P

	250
7	"Welding Characteristics of Dissimilar Thickness TWB Friction Stir Welding upon Welding Parameters", E.G. Choi, <u>K.H. Kim</u>, J.H. Kim, H.S. Bang and H.S. Bang, Proceedings of KSPE 2017 Autumn Conference, P 235
8	"Welding Technology of Dissimilar Materials for Lightweight of Vehicle", Hee-Seon Bang, Han-Sur Bang and <u>Kyoung-Hak Kim</u>, 2017 Materials Research Society of Koran Annual Spring Conference, P 97
9	"Weldability of Hybrid Friction Stir Welded Joints for Tailor Welded Blanks of Dissimilar Materials (Al/Steel) in CTR FLR COMPL", <u>Kyoung-Hak Kim</u>, Hee-Seon Bang, Han-Sur Bang, In-Cheul Choi, Sung-Min Hong and Cheol-Hee Kim, KSAE 2017 Annual Spring Conference
10	"The Effect of Periodic Boiling and Wire Oscillation on Process Stability in Hot Wire Laser Welding (HWLW)", <u>Kyoung-Hak Kim</u>, Han-Sur Bang, Yeong-Bin Son, Alexander F.H. Kaplan, Jonas Näsström and Jan Frostevarg, Abstracts of the 2016 Autumn Annual Meeting of Korean Welding and Joining Society, Vol. 65, P 131
11	"A Study on the Mechanical Characteristics of FCA Weldment in Dissimilar Metal (High Mn steel-STS304L)", <u>Kyoung-Hak Kim</u>, Seung-Yeop Baek, Han-Sur Bang, Sung-Min Joo, Hee-Seon Bang, Soon-Gi Lee, In-Shik Suh, Il-Wook Han and Jong-Sub Lee, Abstracts of the 2015 Autumn Annual Meeting of Korean Welding and Joining Society, Vol. 63, P 103
12	"Evaluation on the Melting Behavior of Wire and Microstructure in Narrow-gap Laser Welded Joints using Hot-wire", <u>Kyoung-Hak Kim</u>, Han-Sur Bang, Alexander F.H. Kaplan, Jonas Näsström and Jan Hee-Seon Bang, Abstracts of the 2015 Spring Annual Meeting of Korean Welding and Joining Society, Vol. 62, P 176
13	"Characteristics of tensile strength and microstructure in FCA Welded cryogenic high manganese steel joint", Seung-Yeop Baek, <u>Kyoung-Hak Kim</u>, Bi-Ryong Kim, Sung-Min Joo, Hee-Seon Bang, Han-Sur Bang, Abstracts of the 2015 Spring Annual Meeting of Korean Welding and Joining Society, Vol. 62, P 153
14	"Evaluation of Corrosion Resistance of Hybrid Friction Stir Welded Joints in Dissimilar Materials(SS400/AA6061-T6)", <u>Kyoung-Hak Kim</u>, Chan-Seung Ro, Hee-Seon Bang and Han-Sur Bang, Abstracts of the 2014 Autumn Annual Meeting of Korean Welding Society, Vol. 61, P 60
15	"Weldability of Fillet Welded Joint for AA5052 by Friction Stir Welding", Chan-Seung

103

	Ro, <u>Kyoung-Hak Kim</u>, Guo-Cheng Zheng, Han-Sur Bang and Hee-Seon Bang, Abstracts of the 2013 Autumn Annual Meeting of Korean Welding Society, Vol. 59, P 186
16	"Fatigue and Residual Stress Characteristics of Thin Ferritic Stainless Steel by FSW and TIG-FSW Hybrid Technology", <u>Kyoung-Hak Kim</u>, Han-Sur Bang, Hee-Seon Bang, Abstracts of the 2013 Autumn Annual Meeting of Korean Welding Society, Vol. 59, P 117
17	"Weldability of Thin Ferritic Stainless Steel by FSW Using Tool without Pin", <u>Kyoung-Hak Kim</u>, Guo-Cheng Zheng, Han-Sur Bang, Hee-Seon Bang, Abstracts of the 2013 Spring Annual Meeting of Korean Welding Society, Vol. 58, P 193
18	"Friction Stir Welding of Thin Ferritic Stainless Steel", <u>Kyoung-Hak Kim</u>, Han-Sur Bang and Hee-Seon Bang, Abstracts of the 2012 Autumn Annual Meeting of Korean Welding Society, Vol. 57, P 182
19	"A Study on Weldability of TIG Assisted Friction Stir Welding of STS 430 Ultra-Thin Sheet", Jun-Hyung Kim, Hee-Seon Bang, Han-Sur Bang, Sung-Min Joo, Heung-Joo Kim and <u>Kyoung-Hak Kim</u>, Abstracts of the 2011 Autumn Annual Meeting of Korean Welding Society, Vol. 56, P 34
International Proceeding Papers (8)	
1	"Thermo-Mechanical Characteristics of Solder Joints with Pillar Bump's Aspect Ratio", Hee-Seon Bang, Han-Sur Bang, Hyeong-Cheol Kim, <u>Kyoung-Hak Kim</u>, Seong-Min Hong, International Union of Materials Research Societies- International Conference on Electronic Materials, 2018
2	"The Effect of Welding Parameters on Friction Stir Weldability in Dissimilar Joints of Aluminium Alloy 5052 and Advanced High Strength Steel (DP590 steel)", <u>Kyoung-Hak Kim</u>, Han-Sur Bang, Hee-Seon Bang, International Symposium on Precision Engineering and Sustainable Manufacturing, 2018
3	"Influence of Preheating Source on Weldability of Dissimilar Materials by Hybrid Friction Stir Welding", Hee-Seon Bang, Han-Sur Bang, <u>Kyoung-Hak Kim</u>, International Welding and Joining Conference, 2017
4	"Periodic boiling connected to hot wire oscillation during narrow gap laser welding", <u>Kyoung-Hak Kim</u>, Han-Sur Bang, Hee-Seon Bang, Jong-Hee Kim, Alexander F. H. Kaplan, Jonas Näsström, International Welding and Joining Conference, 2017
5	"Influence of Preheating source on Mechanical Properties and Welding Residual Stress Characteristics in ultra thin STS Hybrid Friction Stir Welded Joints", <u>Kyoung-Hak Kim</u>,

	Han-Sur Bang, Hee-Seon Bang, International Symposium on Green Manufacturing and Application, 2016
6	"Narrow gap laser welding by multilayer hot wire addition", Alexander Kaplan, <u>Kyoung-Hak Kim</u>, Hee-Seon Bang, Han-Sur Bang, Jonas Näsström, Jan Frostevarg, 34th International Congress on Applications of Laser & Electro-Optics, 2015
7	"Joint properties of thin ferritic stainless steel by GTAW-FSW hybrid welding", <u>Kyoung-Hak Kim</u>, Chan-Seung Ro, Jeong-Hoon Baek, Han-Sur Bang, Hee-Seon Bang, 67th IIW Annual Assembly & International Conference, 2014
8	"Joining of thin 430M2 stainless steel by friction stir welding without pin", Hee-Seon Bang, <u>Kyoung-Hak Kim</u>, Chan-Seung Ro, Han-Sur Bang, Processing and Fabrication of Advanced Materials XXII (PFAM XXII), 2013
Domestic Journal Papers (2)	
1	"Hot Wire Laser Welding of Multilayer for Narrow Gap - Analysis of Wire Melting /Transfer and Arc Formation Phenomenon by High Speed Imaging -", <u>Kyoung-Hak Kim</u>, Han-Sur Bang, Hee-Seon Bang, Alexander F. H. Kaplan, Jonas Näsström, Jan Frostevarg, Journal of Welding and Joining, Vol. 34, No.5, October, 2016, p 26-32
2	"Laser Stitch Welding Technology for the Fabrication of Automotive Parts", Sung-Min Joo, Hee-Seon Bang, Jun-Ui Han, <u>Kyoung-Hak Kim</u>, Byoung-Ho Ahn, Journal of the Korean Welding and Joining Society, Vol. 31, No.4, August, 2013, p 1-6
International Journal Papers SCI(E) (5)	
1	"The Analysis of Viscoplastic Behavior Using Finite Element Analysis at Solder Joints on Pillar Bump's Aspect Ratio", Hyeong-Cheol Kim, Han-Sur Bang, <u>Kyoung-Hak Kim</u>, Seong-Min Hong, Hee-Seon Bang, Nanoscience and Nanotechnology Letters, Vol. 10, No. 9, 2018, p 1197-1203
2	"Numerical simulation of laser assisted friction stir welding of dissimilar materials", Jesper Sundqvist, <u>Kyoung-Hak Kim</u>, Hee-Seon Bang, Han-Sur Bang, Alexander F. H. Kaplan, Science and Technology of Welding and Joining, Vol. 23, No. 4, 2018, p 351-356
3	"Influence of Preheating Source on Mechanical Properties and Welding Residual Stress Characteristics in Ultra Thin STS Hybrid Friction Stir Welded Joints", <u>Kyoung-Hak Kim</u>, Han-Sur Bang, Hee-Seon Bang, Chan-Seung Ro, International Journal of Precision Engineering and Manufacturing-Green Technology, Vol. 4, No. 4, 2017, p 393-400

4	"Joint properties of ultra thin 430M2 ferritic stainless steel sheets by friction stir welding using pinless tool", <u>K.H. Kim</u>, H.S. Bang, H.S. Bang, A.F.H. Kaplan, Journal of Materials Processing Technology, Vol. 243, 2017, p 381~386
5	"Narrow Gap Laser Welding by Multilayer Hot Wire Addition", Alexander F. H. Kaplan, <u>Kyoung-Hak Kim</u>, Hee-Seon Bang, Han-Sur Bang, Jonas Näsström, Jan Frostevarg, Journal of Laser Applications, Vol. 28, No. 2, 2016, p 022410-1~8